

2019 ANNUAL REPORT

HP-HT laboratory

EXPERIMENTAL VOLCANOLOGY AND GEOPHYSICS

laboratory

NEW TECHNOLOGIES

Department of Seismology and Tectonophysics
Istituto Nazionale di Geofisica e Vulcanologia

Via di Vigna Murata 605 | 00143 Roma - Italia | Tel +39-0651860437 | Fax +39-0651860507
www.ingv.it

Follow us on



Follow us on



HPHTlab - Science, Technology & Engineering



HPHTlab (@hphtlab) | Twitter

About the cover:

Stromboli, lava flows moving down along Sciara del Fuoco from the upper flank of the SW crater (4 August 2019).

Credits:

HPHT Lab

Contents



1	ABSTRACT	5
2	PERSONNEL	6
3	INSTRUMENTS and FACILITIES	8
4	LABORATORY ACTIVITIES	13
5	RESEARCH PROJECTS	19
6	PARTNER LABORATORIES	21
7	PARTNER INSTITUTIONS	22
8	RESEARCH ACTIVITY and RESULTS	23
9	SEMINARS and TEACHING	122
10	VISITING SCIENTISTS	125
11	MEETINGS, WORKSHOP and SYMPOSIA	126
12	PUBLICATIONS	134



HP-HT Laboratory of Experimental Volcanology and Geophysics

LNT Laboratory of New Technologies

2019 Annual Report

11 ABSTRACT

In this annual report, we have summarized the most important research activities of the High Pressure High Temperature Laboratory of Experimental Volcanology and Geophysics and of the Laboratory of New Technologies that were conducted in 2019. The Labs hosted 15 full-time visiting scientists, 10 associated researchers, 16 PhD/Master students.

During the past year, 20 national- to international-level projects/collaborations were active, involving more than 15 partner laboratories and institutions. As part of the EPOS TCS 'Multiscale Laboratories' 3rd pilot call for Trans-National Access (TNA) activities, the HPHT lab has hosted two international scientists whose proposals were accepted for physical access.

The HPHT Lab continued its numerous research studies in petrology, mineralogy and volcanology (31 studies) and in rock physics (14 studies).

LNTS offers a consultancy service for questions concerning electronics and mechanics, and also produces original works in the field of measuring instruments and electronics. In 2019, 2 prototypes were developed and a patent application was submitted.

Finally, the Lab personnel have organized and participated to 14 meetings, workshops and seminars in Italy and abroad, and have published 50 scientific articles in the most important international journals.



21 PERSONNEL

HPHT Laboratory

Piergiorgio Scarlato | Senior Researcher, Responsible of the HP-HT group

Stefano Aretusini | Contract Researcher

Gianfilippo De Astis | Researcher

Elisabetta Del Bello | Researcher

Christopher Harbord | Contract Researcher

Valeria Misiti | Technologist

Manuela Nazzari | Researcher

Giacomo Pozzi | Contract Researcher

Tullio Ricci | Researcher

Elena Spagnuolo | Researcher

Laura Spina | Researcher

Jacopo Taddeucci | Senior Researcher

Laboratory of New Technologies

Giovanni Romeo | Technical Director, Responsible of the Laboratory of New Technologies

Giuseppe Di Stefano | Senior Technologist

Alessandro Iarocci | Engineer Technologist

Massimo Mari | Technician

Francesco Pongetti | Engineer Technician

Giuseppe Spinelli | Engineer Technologist

Mario Tozzi | Technician



Giuseppe Urbini | Engineer Technologist

Marcello Silvestri | Technician

Massimiliano Vallocchia | Technician

Associated researchers

Cristiano Collettini | Sapienza Università di Roma, Italy | Associated Professor in Structural Geology

Frances M. Deegan | Uppsala University, Sweden | Researcher

Giancarlo Della Ventura | Università di Roma Tre | Full Professor in Mineralogy

Giulio Di Toro | Università degli Studi di Padova, Italy | Full Professor in Structural Geology

Silvio Mollo | Sapienza Università di Roma, Italy | Associated Professor in Petrology

Valentin R. Troll | Uppsala University, Sweden | Chair of Petrology

Vincenzo Stagno | Sapienza Università di Roma, Italy | Associated Professor in Petrology

Collaborators

Luca Samuele Capizzi | Contract Researcher

Matteo Masotta | Università di Pisa, Italy | Researcher

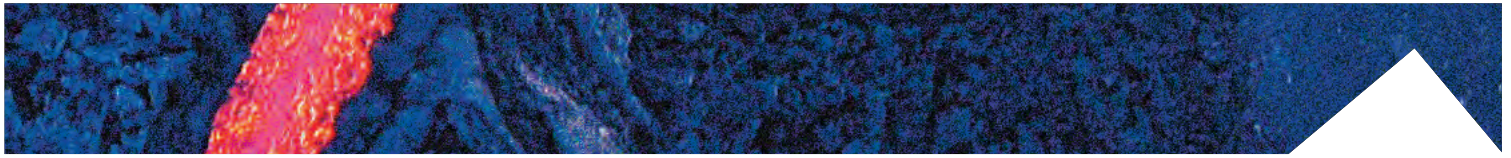
Marco M. Scuderi | Sapienza Università di Roma, Italy | Researcher



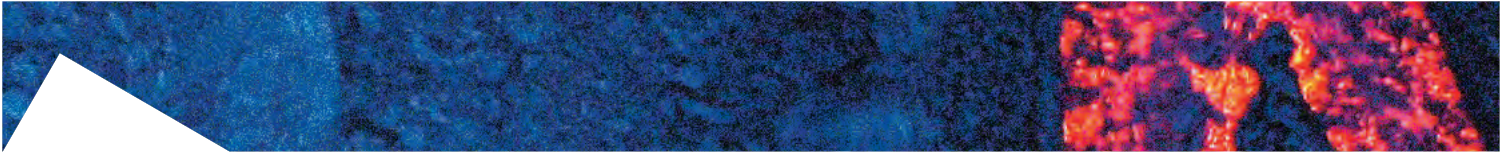
3I INSTRUMENTS and FACILITIES

HPHT Laboratory

- Multiple press 840 ton | [Voggenreiter](#)
- Piston cylinder - 3/4" and 1" pressure plates | [Voggenreiter](#)
- Multianvil - Walker type 6/8 | [Voggenreiter](#)
- Quick Press - Piston Cylinder 3/4" and 1" pressure plates | [Depth of the Earth](#)
- Bi-Tri-Axial Press (BRAVA) | [RMP - INGV](#)
- Low to High Velocity Apparatus (SHIVA) | [RMP - INGV](#)
- Electron microprobe equipped with 5 WDS and 1 EDS | [JEOL JXA-8200](#)
- Field Emission Scanning Electron Microscope equipped with EDS and BSE detectors | [JEOL JSM-6500F](#)
- Auto Carbon coater | [JEOL JEC-530](#)
- Fine coater | [JEOL JFC-2300HR](#)
- High and low temperature furnaces | [Lenton](#)
- Impedance analyser | [Solartron SI1260](#)
- Digital oscilloscope | [Tektronix DPO4032](#)
- Wave generator | [Agilent 33250A](#)
- H-Frame presses 10 ton | [Enerpac](#)
- Uniaxial testing machine with double load cell (15 and 250 kN) and LVDT controller | [Tecnatest](#)
- Precision balance | [Sartorius](#)
- Optical and stereo microscopes | [Leica DMRXP](#) and [Euromex](#)
- Ultra-high velocity, intensified, gated digital camera | [Cordin 204-2](#)
- High speed digital camcorder | [Optronis](#) and [NAC 512 SC](#)
- Stereomicroscopes | [Leica MZ 9.5](#)



- Semiautomatic polisher | [Buehler Minimet 1000](#)
- Power Supply | [Agilent 6575A](#)
- Helium Picnometer | [AccuPyc II 1340](#)
- Permeameter with double intensifier | [Rock Physics](#)
- Rheometer MCR 301 Physica | [Anton Paar](#)
- Vertical Furnace RHTV 120-300/18 | [Nabertherm](#)
- High Temperature Furnace LHT 04/18 | [Nabertherm](#)
- Cecchi data acquisition system | [Applied Seismology](#)
- Rock drilling, cutting, and grinding equipment for samples preparation
- Thermal High speed camera | [FLIR SC 645](#)
- Welder PUK U3 | [Lampert](#)
- Laser line generator | [Edmund optics](#)
- Precision test sieves | [Endecotts](#)
- Laser MGL-III, 532nm 200mW, PSU-III-LED/Unit | [Changchun New Industries](#)
- Multi-Wavelength Analyser LUMiReader® PSA with Particle sizing according to ISO 13317 | [LUMiReader@PSA](#)
- 2 Polarized Free-field Microphones 40AN 1/2", Low Frequency (0.5Hz - 20kHz) | [G.R.A.S.](#)
- Vacuometro PVG-500 | [Pirani](#)
- Petrographic microscope ECLIPSE E-50i POL | [Nikon](#)
- Drying oven UF 75 | [Mettler](#)
- 4K digital camcorders | [Sony](#)
- High speed digital camcorder | [NAC Memrecam-HX6](#)
- Shock-tube apparatus (Jet-Buster) | [INGV](#)
- High speed digital camcorders | [NAC 512 SC](#), [Optronis CR600x2](#), [NAC HX6](#), [NAC HX3](#)
- Laser range finder | [Vectronix VECTOR 21](#)

- 
- Time Lapse Camera with 24-70 lens | [Brinno TLC200 Pro](#)
 - Precision Syringe Pumps | [ISCO](#)
 - Ash dispersal/settling apparatus (Ash-Buster) | [INGV](#)

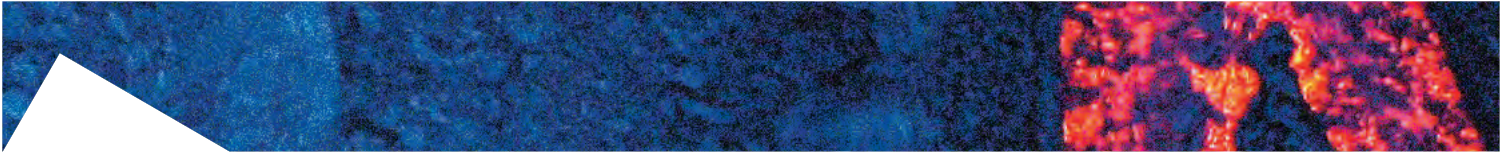
Acquired in 2019

- Drone Mavic 2 Pro | [DJI](#)
- Dual UV cameras 340 UVGE | [Thorlabs](#)
- Laboratory sieve shaker Octagon 200 | [Endecotts](#)
- Triaxial ICP® accelerometer | [PCB Piezotronics](#)
- Three ceramic shear ICP® accelerometers | [PCB Piezotronics](#)
- Two 4-channel ICP® sensor signal conditioners | [PCB Piezotronics](#)



Laboratory of New Technologies

- Analog Oscilloscope | [HP](#)
- Analog Oscilloscope | [Iwatsu SS5710](#)
- Analog Oscilloscope | [Tektronix TDS220](#)
- Analog Oscilloscope | [Tektronix](#)
- Oscilloscope | [HP54201](#)
- Oscilloscope | [HP54602b](#)
- Power supply | [Elind HL series](#)
- Power supply | [Elind 6TD20](#)
- Power supply | [DC DF1731SB](#)
- Signal generator | [HP8656A](#)
- Function generator | [HP3325A](#)
- Multimeter | [HP3478A](#)
- Milling machine for printed circuit boards | [T-Tech](#)
- Logic state analyzer | [HP16500A](#)
- Superheterodyne spectrum analyzer | [Tektronix](#)
- Soldering-reworking station | [JBC advanced AM6500](#)
- Oscilloscope | [FLUKE 199C](#)
- Oscilloscope | [Tektronix DPO4000](#)
- Oscilloscope | [Tektronix MSO4034](#)
- Calibrator | [FLUKE 5700 \(series II\)](#)
- Function generator | [HP33120](#)
- Function generator | [AGILENT 33250 A](#)
- PXI Industrial computer with I/O boards | [National Instruments](#)

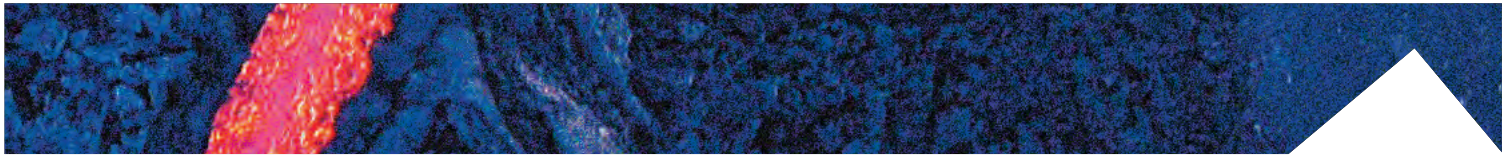
- 
- Waveform generator | [Agilent 33210 A](#)
 - Oscilloscope W wave surfer | [LeCroy 44MXs-A](#)
 - Drone Phantom 3 pro with termination system

Acquired in 2019

- Power supply (4 items) | [-3005D](#)

Machine shop

- Lathe | [Grazioli Fortuna](#)
- Small lathe | [Ceriani](#)
- Small milling machine | [Schaublin](#)
- Cutting machine | [Ercoletta](#)
- Bending machine | [Ercoletta](#)
- Drill press | [Serrmac](#)
- Small drill press | [Webo](#)
- Bandsaw | [Femi](#)
- Grinder | [Femi](#)
- Extractor hood | [Filcar](#)
- Inverter welding machine | [Tecnica](#)
- TIG welding machine | [Cebora](#)
- Miter saw
- Numerically controlled milling machine



4| LABORATORY ACTIVITIES

Experimental laboratory

Super press I Multi Anvil

10 experiments has been conducted in the frame of tourmaline project.

Quick press I Piston cylinder

The 1 inch pressure plate

43 experiments in the frame of 2 projects have been conducted during 2019:

1) Kinetic of major and minor elements; 2) shale solubility

The 3/4 inch pressure plate

5 experiments in the frame of 1 project have been conducted during 2019:

viscosity measurements

The 1/2 inch pressure plate

20 experiments in the frame of 2 projects have been conducted during 2019:

1) K geobarometer, 2) alkaline magmas

Furnaces

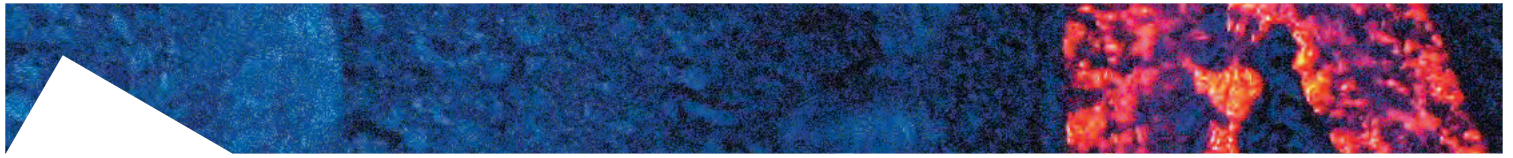
48 experiments have been performed in the frame of the following project:

- Kinetic aspects of major and trace element partitioning between olivines and melt during solidification of terrestrial basaltic materials

BRAVA

During the 2019 we performed about 60 experiments testing most of the capabilities of the apparatus. The experimental work has been focused on consolidating the research lines developed in the past years. In the following we summarize the main research themes:

1) Frictional properties of phyllosilicate-rich faults.



2) Fault stability of carbonate-clay mixture, within the ENI Fault stability project.

3) Comparison of laboratory permeability: Darcy's law vs. pressure oscillation technique.

4) Characterization of slip velocity functions recorded for different lithologies during stick-slip laboratory experiments.

Finally, we have used BRAVA for teaching rock-physics at Master students of the Petrophysics course at La Sapienza Università di Roma and for outreach with high-school students.

Slow to HIgh Velocity Apparatus (SHIVA)

The tenth year of activity of SHIVA has been mainly dedicated to:

1. The investigation of fluid – rock interaction in affecting frictional properties of bare rocks and gouges. The latter in particular by developing a new system for fluid pressurization of gouges.
2. The study of natural and experimental smectite group clay minerals to understand the mechanical behavior and the deformation processes pertaining to subduction zone fault cores at shallow depth (<1 km) following IODP projects e.g. Sumatra-Adaman region and Hikurangi subduction zones.
3. The study of the energy budget and the thermomechanical weakening of fault rocks by means of: optical fibers to measure the temperature increase directly inside the fault zone and by using dynamically consistent slip velocity functions.

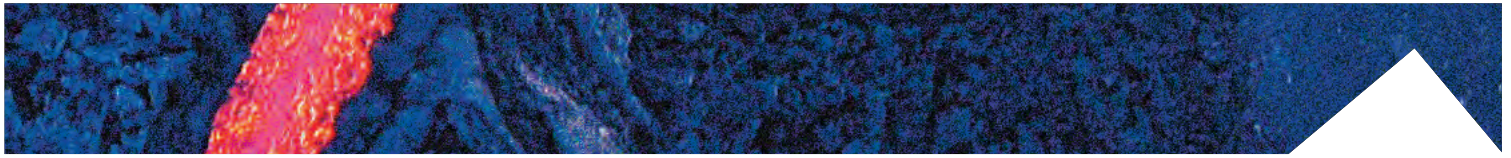
We collaborate with the Geophysical Borehole Research center at Koyna (India) to study triggered seismicity by lake impoundment in one of the best instrumented natural laboratory installed worldwide.

We studied the effect of fluid chemistry (injecting CO₂- H₂O mixtures) and fluid viscosity (using mixtures of glycerol and water) in fault reactivation for both natural and induced seismicity in cohesive westerly granite, calcite and basalts.

We studied the effect of fluid diffusion through pre-existing fractures and we are developing models to understand the mechanical and chemical effect of fluid diffusion on faults strength to test the hypothesis of dynamic weakening by thermal pressurization and/or electrodynamic lubrication.

We studied and start to model the effect of lithological heterogeneities in storing and releasing elastic energy in subduction zones under room humidity and water dampened conditions by using a novel technique of loading gradually the samples to trigger spontaneous instabilities.

We developed a new system to surpass a challenging technical problem of gouge confinement with pressurized fluids. We are now able to control the slip velocity functions to test dynamically consistent condition of frictional behavior



at earthquake slip velocities.

We installed optical fibers to measure the temperature increase during dynamic weakening and frictional heating of fault rocks.

We finalized the installation of a novel device to monitor changes in fault physical properties (V_p , V_s , attenuation, Young modulus) during the seismic cycle.

To this end we run 153 experiments during 2019.

Analog laboratory

The ash Burster laboratory device for the study of volcanic particles ejection and sedimentation was implemented with a sedimentation chamber, and a series of pilot experiments were carried out on compressed air/particle jets mixtures.

A custom-designed prototype of a mini wind tunnel was realised for carrying out volcanic ash resuspension experiments.

Resuspension experiments were carried out both in the field, on naturally deposited ash from Sakurajima (Japan) and Cordon Caulle (Chile), and in the lab, using natural ash to test the behaviour of dust-repellent surfaces.

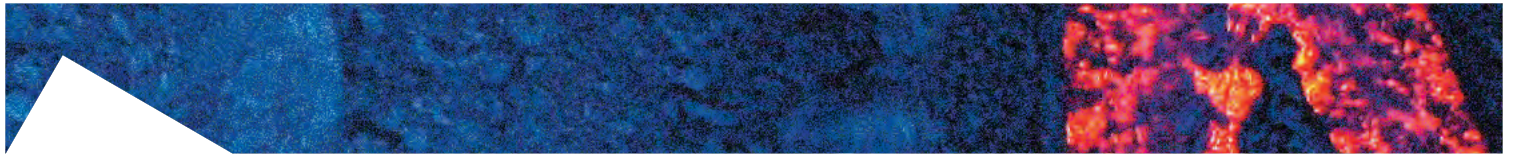
Rheometer

5 rheometer tests were performed on natural asphalts for the characterization of their viscous behaviour as a function of heating.

FaMoUS (Fast Multiparametric Setup)

Visible Highspeed cameras (NACandOptronis): i) about 50 high speed video acquisitions were collected during the field campaigns in Japan (January) and Patagonian Argentina (October), and during calibration tests at Aarhus Environmental facility (Denmark, June) for the characterization of volcanic ash resuspension (300x1000 pixel and 2000/3000 fps); ii) about 25 Strombolian explosions events were filmed at 500 fps during the period 9-11 May at Stromboli.

Infrared Camera: about 1.5 to 5 hours of continuous recording of the volcanic activity at the crater terrace of Stromboli were acquired at a range of frequency (50 to 200 Hz) and image resolution (640x120-480) in the period 9-11 May, 20 June, 27-28 July, 7 September and 26 November.



UV Camera: about 3 to 5 hours of continuous recording of the volcanic activity at the crater terrace of Stromboli were acquired at a 50 Hz and image resolution (640x480) in the period 9-11 May, 20 June.

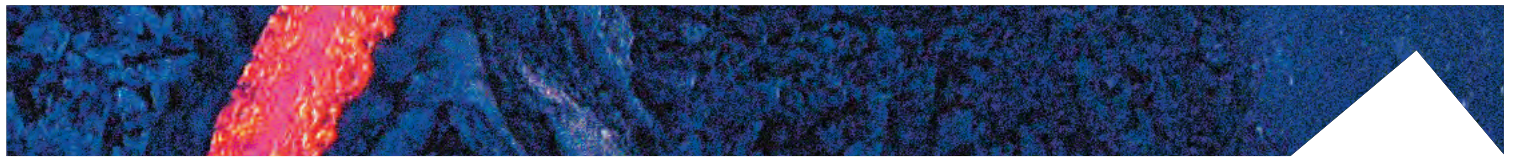
Drone: 5 drone overflights were performed in May, June, August, September, November to reconstruct morphological variations of the crater terrace at Stromboli.

Microanalytical laboratory

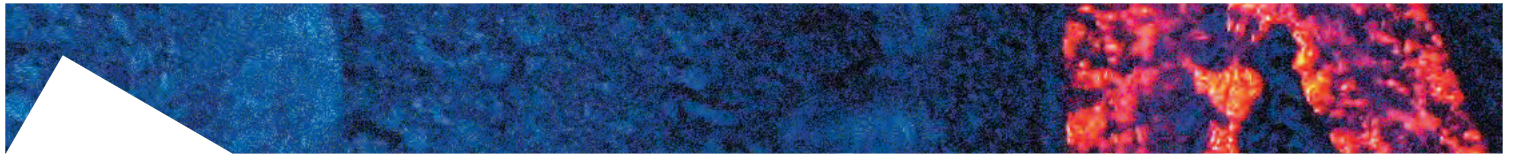
FE-SEM and EMP performed 330 days of analysis in the frame of 33 research proposals.

Proposal

1. Messinian tephra in central and northern Apennines: distribution, texture and mineralogy of a large eruption
G. Iezzi - P. Scarlato | Università di Chieti - INGV Roma1
2. Kinetic aspects of major and trace element partitioning between olivine and melt during solidification of terrestrial and extraterrestrial basaltic materials
S. Lang - V. Misiti - P. Scarlato | Sapienza Università di Roma - INGV Roma1
3. Timescales of crystallization in basaltic magmas: effects of strain rate and undercooling
F. Di Fiore - P. Scarlato | Università RomaTre - INGV Roma1
4. Reconstruction of the intensive variables and magmatic architecture of Vulcano island
F. Palummo - M. Nazzari - G. De Astis | Sapienza Università di Roma - INGV Roma1
5. Experimental investigation of mechanisms generating phonolites in the Dunedin Volcano, New Zealand
A. Pontesilli - M. Nazzari | University of Otago (New Zealand) - INGV Roma1
6. Lab-study on the frictional properties of basalts interacting with H₂O- and CO₂- rich fluids and implications for CO₂ storage
P. Giacomel - E. Spagnuolo | Sapienza Università di Roma - INGV Roma1
7. Dynamic crystallisation in magmas
M. Nazzari | INGV Roma1
8. Crystal-chemical variations induced by variable cooling rate in sub-alkaline silicate liquids
G. Iezzi - V. Misiti | Università di Chieti - INGV Roma1
9. The Pigroot duality, an experimental investigation of the mantle xenolith-bearing Pigroot phonolite
Y. Yagolnitzer - M. Nazzari | University of Otago (New Zealand) - INGV Roma1



10. Chemical and degassing dynamics of magma-sulfate (CaSO_4) and magma-shale interaction
F. Deegan - V. Misiti | University of Uppsala - INGV Roma1
11. Experimental study of borosilicates minerals at HP-T conditions with oxy-thermobarometric applications
V. Stagno - P. Scarlato | Sapienza Università di Roma - INGV Roma1
12. Olivine-clinopyroxene-plagioclase-melt cation exchange reactions as a tool for a quantitative understanding magma dynamics
F. Di Stefano - P. Scarlato | Sapienza Università di Roma - INGV Roma1
13. In situ viscosity and structural measurements of volatile-bearing melts at upper mantle pressure-temperature conditions
V. Stagno | Sapienza Università di Roma
14. Analysis of Pre- and post-Experimental Clays and Rocks (APECAR) storage
S. Aretusini - E. Spagnuolo | INGV Roma 1
15. Petrological study of a tephritic to phono-tephritic caldera forming eruption: the case of Onano Eruption (Latera volcano, Central Italy)
P. Landi | INGV PI
16. Timescales of magmatic processes
I. Arienzo - M. Nazzari | INGV OV - INGV Roma1
17. Reading the mineral record of REE enrichment in carbonatite and alkaline-silicate magmas
C. Beard - M. Nazzari | British Geological Survey - INGV Roma1
18. Volcanic crystals as recorders of magma dynamics and eruption triggers
T. Ubide - P. Scarlato | University of Queensland - INGV Roma1
19. Transformation of Cu-slag and glass wastes in new glass-ceramics
G. Iezzi | Università di Chieti
20. Geochemical characterization of geological obsidian sources
M. Carapezza | INGV Roma1
21. Stratigraphy in an Etnean lava flow: post-emplacement differentiation
G. Iezzi - M. Nazzari | Università di Chieti - INGV Roma1
22. Brains2South
M.A. Di Vito - M. Nazzari | INGV OV - INGV Roma1
23. Multidisciplinary gas monitoring and petrological approach for identifying magmatic source of active volcanoes in the Southern Volcanic Zone
P. Robidoux | Universidad Mayor, Santiago (Chile)



24. Orthosilicic and persilicic fluid in gemstone natural lithospheric diamonds
F. Nestola - V. Misiti | Università di Padova - INGV Roma1

25. Rock Mass Creeping, a multidisciplinary approach to characterize the long-term behaviour of faults and landslides
F. Trippetta - E. Spagnuolo | Sapienza Università di Roma - INGV Roma1

26. Crystal-chemistry and texture of a 2015 Mt. Etna bomb storage
G. Iezzi - M. Nazzari | Università di Chieti - INGV Roma1

27. Inclusions of the Monte Amiata volcanic rocks
G. Della Ventura | Università RomaTre

28. The 3 July 2019 paroxysm at Stromboli volcano (Italy): is Stromboli playing by new rules?
P. Scarlato | INGV Roma 1

29. Fractured microlites
J. Taddeucci | INGV Roma 1

30. Moine Amphibolites
G. Pozzi | INGV Roma 1

31. COupling of Rheology and Textures in Experimental Seismic faults (CORTES)
G. Pozzi | INGV Roma 1

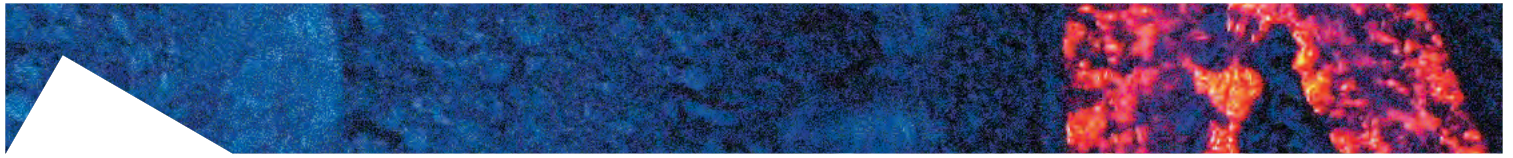
32. Volcanic hazard assessment at Mt. Etna: a time-integrated, polybaric and polythermal perspective
P. Moschini - P. Scarlato | Sapienza Università di Roma - INGV Roma1

33. Reproduce the seismic cycle of a complex fault in the laboratory and predict its progress with Machine Learning
N. Bigaroni - G. Di Stefano | Sapienza Università di Roma - INGV Roma1

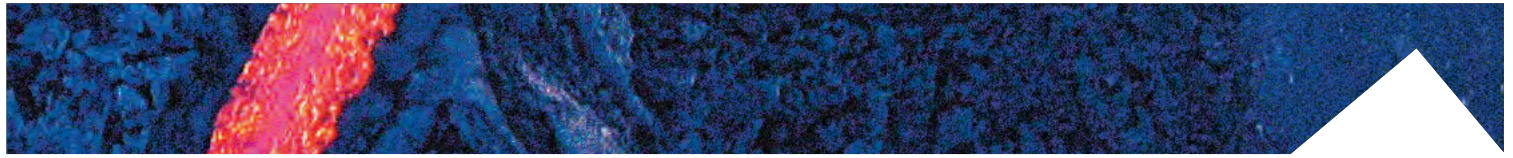


51 RESEARCH PROJECTS

1. **MIUR Progetti Premiali 2015** | Ash-RESILIENCE A research infrastructure for volcanic ash hazard assessment to aviation and communities living near Italian active volcanoes | P.I. **A. Costa, D. Andronico**
2. **MIUR Progetto TOP-DOWN FISR 2016** | Task 3: Magmatismo e vulcanismo dell'Italia Centrale, Attività C) Studio del sistema vulcanico dei Colli Albani (Scarlato P.) | P.I. **F. Galadini**
3. **MIUR Progetto PRIN** | Scales of solidification in magmas: applications to volcanic eruptions, silicate melts, glasses, glass-ceramics | P.I. **M. Carroll**
4. **MIUR Progetto FISR Ricerca Libera 2016** | Gas hazard in Central Italy: Experimental investigation on the Radon emissions from volcanic rocks | P.I. **P. Scarlato**
5. **MIUR PON Ricerca e Innovazione 2014-2020** | Infrastruttura di Ricerca Italiana per le Geoscienze (GRINT) | P.I. **G. Puglisi**
6. **European research project** | EUROVOLC “European Network of Observatories and Research Infrastructures for Volcanology” | P.I. **K. Vogfjord**
7. **European research project** | EPOS “European Plate Observing System” Implementation Phase, WP 16 Multi-scale Laboratories | P.I. **M. Cocco**
8. **European Research Project - ERC Consolidator Grant Project** | NOFEAR: New Outlook on seismic faults: From EARth quaken ucleation to arrest | P.I. **G. Di Toro**
9. **European Research Infrastructures Transnational Access EUROPLANET 2020** | Agreement n.:654208 (15-EPN-003). Approved proposal grant n. 10341: “High-Speed Imaging Of Gas-Particle And Particle-Particle Interactions In Lab-Sized Volcanic Jets/plumes” | P.I. **J. Taddeucci, E. Del Bello**
10. **European research project HEMERA** | HERMES (Hemera Returning Messenger a Thread of HEMERA) | P.I. **G. Romeo**
11. **NERC Urgency Grant NE/T009292/1** | The 3 July 2019 paroxysm at Stromboli volcano (Italy): is Stromboli playing by new rules? | P.I. **C. Petrone, INGV R.U. leader P. Scarlato**
12. **Sapienza Progetti di Ateneo** | Kinetic controls on the partitioning of chemical species between olivine, clinopyroxene and melt during solidification of terrestrial and extraterrestrial basaltic rocks: Implications for the understanding of the crystallization conditions of magmas | P.I. **S. Mollo**
13. **Sapienza Progetti di Ateneo** | Fault distribution, complexity and slip behavior of active faults in the Apennines: insights from field studies and rock deformation experiment | P.I. **C. Collettini**
14. **Sapienza Progetti di Ateneo** | Quantitative understanding of magma reservoirs feeding large-scale volcanic eruptions at Campi Flegrei | P.I. **S. Mollo**



15. **Sapienza Progetti di Ateneo I** Viscosity and melt structure of anhydrous and carbonated leucite-basanite melts at high pressure and temperature: implications for the K-rich magmatism underneath central Italy | P.I. V. Stagno
16. **Sapienza Progetti di Ateneo I** Experimental study of borosilicates minerals at HP-T conditions with oxy-thermobarometric applications | P.I. V. Stagno
17. **ENI I** contratto aperto n. 25000307 | FAST – Fault Stability | P.I. E. Tinti
18. **École polytechnique fédérale de Lausanne I** Frictional properties of Opalinus clay | P.I. M. Violay
19. **DPC Grant – EXTEND –** Estendere la conoscenza del terremoto dalla profondità in superficie | P.I. E. Spagnuolo
20. **Petrobras3 - Petroleo Brasileiro S.A. -** Igneous rocks as source and sink of abiogenic hydrocarbons and CO₂ | P.I. G. Etiope



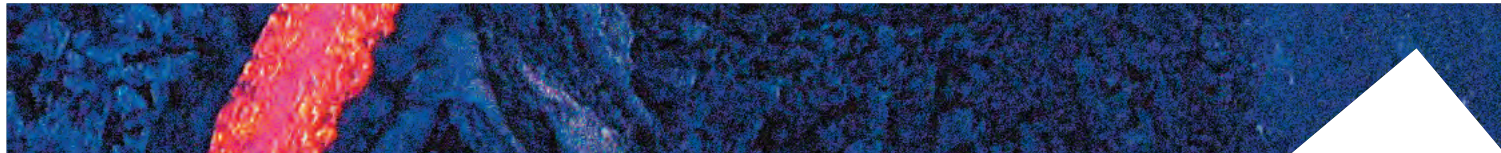
6 | PARTNER LABORATORIES

1. **Planetary Environmental Facilities** | Aarhus University | Denmark
2. **Experimental & Physical Volcanology** | Ludwig Maximilians Universität | Germany
3. **Dipartimento di Scienze** | Università di Roma Tre | Italy
4. **Geoscience Department** | Utrecht University | Netherlands
5. **Institute of Geochemistry and Petrology** | ETH Zurich | Switzerland
6. **Dipartimento di Scienze Biologiche, Geologiche e Ambientali** | Università di Catania | Italy
7. **Dipartimento di Fisica e Scienze della Terra** | Università di Ferrara | Italy
8. **Petro-Volcanology Research Group (PVRG) Department of Physics and Geology** | Università di Perugia | Italy
9. **School of Earth and Environmental Sciences** | University of Queensland | Australia
10. **Department of Geology** | University of Otago | New Zealand
11. **LEMR** | EPFL | Lausanne, Switzerland
12. **Geoscience Department** | Utrecht University | Netherlands
13. **Rock Mechanics Laboratory** | Durham University | UK
14. **Jackson School of Geosciences** | Texas University at Austin | USA
15. **Dipartimento di Geoscienze** | Università di Padova | Italy



71 PARTNER INSTITUTIONS

1. Ludwig Maximillians Universitat Munchen | **Munich** | Germany
2. Department of Geology and Geophysics, SOEST | **University of Hawaii** | USA
3. Department of Physics and Astronomy | **Aarhus University** | Denmark
4. HVO Hawaiian Volcano Observatory | **USGS** | USA
5. School of Earth and Environmental Sciences | **University of Queensland** | Australia
6. Department of Geology | **University of Otago** | New Zealand
7. Royal Hollow University of London | **London** | UK
8. Department of Earth Sciences | **University of Durham** | UK



8 | RESEARCH ACTIVITY and RESULTS

8.1 PETROLOGY, MINERALOGY, VOLCANOLOGY

Intra-eruptive trachyte-phonolite transition: Natural evidence and experimental constraints on the role of crystal mushes

Brenna M., Pontesilli A., Mollo S., Masotta M., Cronin S.J., Smith I.E.M., Moufti M.R.H., Scarlato P.

Two main compositional endmembers characterize the evolved spectrum of alkaline rocks: phonolite and trachyte, the former characterized by higher alkali and lower silica contents. In intraplate volcanic settings, trachytes and phonolites are frequently associated within the same volcanic system, although phonolites are less abundant and traditionally interpreted as the magmatic evolution of silica undersaturated primary basanitic magmas. In contrast, the generation of trachytes is often attributed to the magmatic evolution of Si-rich alkaline basalts. The generation of phonolite from trachytes is uncommon, as it implies the crossing of the thermal barrier and critical plane of silica undersaturation. Nevertheless, a co-genetic suite displaying compositional transition from benmoreite-trachyte to phonolite has been observed within the Al Shaatha pyroclastic sequence in the Harrat Rahat Volcanic Field (Kingdom of Saudi Arabia). We performed crystallization experiments on benmoreite and trachyte starting compositions to simulate the physicochemical conditions that generated the observed liquid line of descent, by systematically varying pressure, temperature and volatiles concentrations. The experimental conditions were 200-500 MPa, 850-1150 °C, 0-10 wt.% H₂O, 0.0-0.5 wt.% CO₂, and NNO+2 oxygen buffer. The experimental mineral assemblage consists of clinopyroxene, feldspar, and titanomagnetite, as well as glass in variable proportions. The degree of crystallinity of hydrous runs is lower than that of anhydrous ones at analogous pressure and temperature conditions. Experiments evidences that, at 500 MPa and 1000-1150 °C, the Al Shaatha benmoreitic magma differentiated toward trachytic compositions, whereas formation of trachytic magmas continues at shallower crustal levels and lower temperatures (200 MPa and 950-850 °C). Clinopyroxene crystallizes with compositions diopside-augite and augite-hedenbergite, respectively, at 500 and 200 MPa. The saturation of feldspar is primarily controlled by temperature and volatile content, with the more potassic composition equilibrating at low temperature (850-

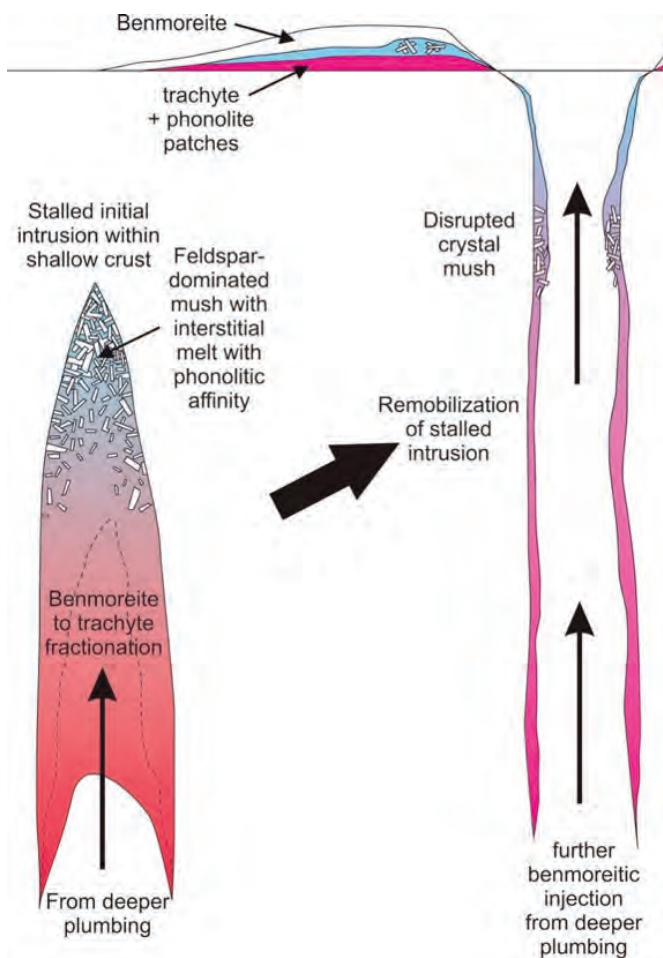
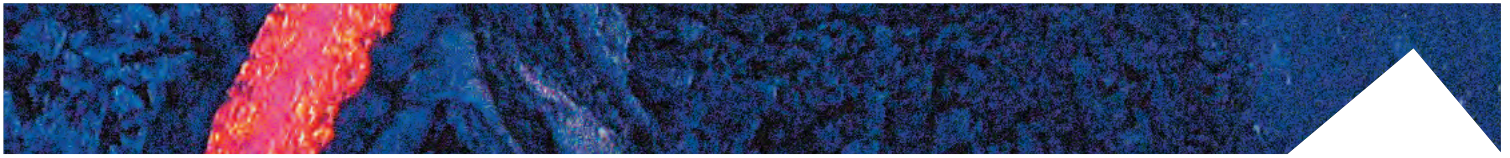


Fig. 1 | Schematic illustration (not to scale) of the proposed scenario for the formation of phonolite erupted at Al Shaatha. An initial stalled intrusion crystallizes extensively to form an anorthoclase-dominated crystal mush with interstitial phonolitic melt. A subsequent injection from the deeper plumbing remobilizes and interacts with the crystal mush, resorbs some anorthoclase and entrains the interstitial melt. Schematic illustration (not to scale) of the proposed scenario for the formation of phonolite erupted at Al Shaatha. An initial stalled intrusion crystallizes extensively to form an anorthoclase-dominated crystal mush with interstitial phonolitic melt. A subsequent injection from the deeper plumbing remobilizes and interacts with the crystal mush, resorbs some anorthoclase and entrains the interstitial melt.

900 °C) and anhydrous (for benmoreite) or hydrous (for trachyte) conditions. At low pressure (200 MPa), temperatures below 850 °C, and anhydrous conditions, the degree of crystallization is extremely high (>90%), and the residual glass obtained from trachyte experiments is characterized by peralkaline and sodic affinity. Although none of the investigated experimental conditions reproduced the alkali increase coupled with a decrease or unchanged SiO₂, this finding is consistent with natural eruptive products containing interstitial phonolitic glass within an anorthoclase framework. The shift from trachyte to phonolite is therefore interpreted as the result of open system interaction between trachytic magma and intercumulus phonolitic melt, as well as of dissolution of anorthoclase from a crystal mush (Figure 1).



The behaviour of schorl tourmaline at high pressure and temperature

Capizzi L.S., Stagno V., Bosi F., Ballirano P., Scarlato P., Andreozzi G.B.

Tourmaline supergroup minerals are the most common borosilicates in Earth with a large chemical variability occurring as an accessory phase in select rock types. Tourmaline, with a generalized chemical formula of $XY_3Z_6(BO_3)_3(T_6O_{18})V_3W$, (where: X = Ca, Na, K; Y = Li, Mg, Fe^{2+} , Mn^{2+} , Al, Cr^{3+} , V^{3+} , Fe^{3+} , (Ti^{4+}) ; Z = Mg, Al, Fe^{2+} , Fe^{3+} , Cr^{3+} , V^{3+} ; T = Si, Al, B; B = B; V = OH, O; W = OH, F, O). Tourmaline incorporates the largest amount of B up to 10 wt% in their structure along with hydroxyl group (~3 *a.p.f.u.*). Importantly, tourmalines can also contain variable amount of both Fe^{2+} and Fe^{3+} implying a key role in redox reactions involving coexisting minerals and fluids. Recent observations of Fe-bearing tourmaline

coexisting with diamonds in UHP metamorphic rocks have raised important questions on their stability at pressures (P) and temperature (T) conditions of the Earth's upper mantle with implications for the origin of oxidised H- and B-rich metasomatic fluids.

In this study, we carried out a total of 13 runs at variable pressures and temperature using both the gas-mixing furnace (1-atm runs) and the Walker-type multi anvil press (runs at 3.5 and 6 GPa) both available at the HPHT Experimental Laboratory of the INGV (Rome). The starting material used in this study is a natural tourmaline made of 90% schörl end-member with ~19 wt.% of iron as Fe^{2+} . The grinding tourmaline was, then, mixed with a mixture of rhenium and rhenium (IV) oxide and pure graphite (C) and silver oxalate ($Ag_2C_2O_4$), respectively, to act as solid redox buffers. Textural and chemical anal-

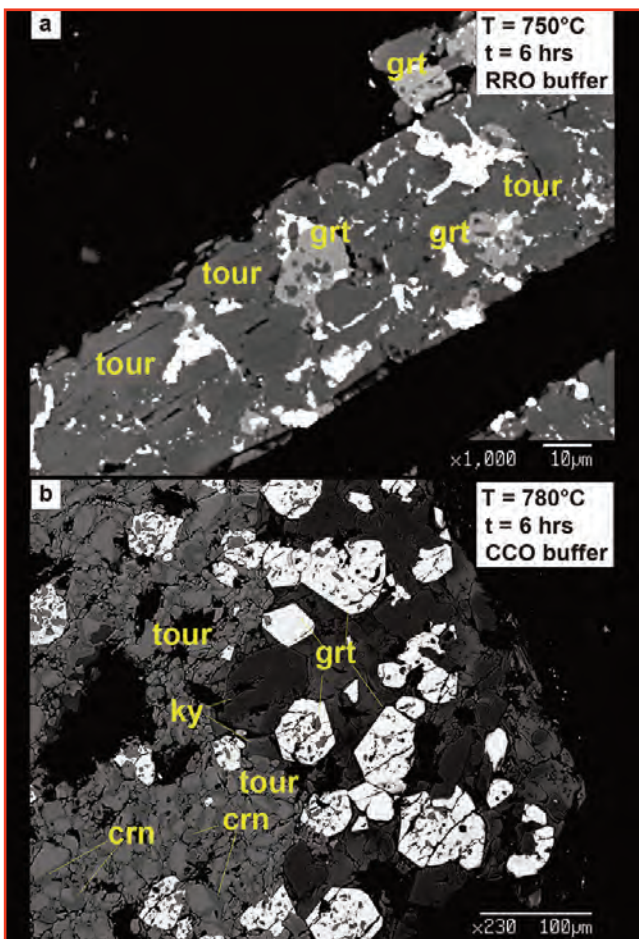
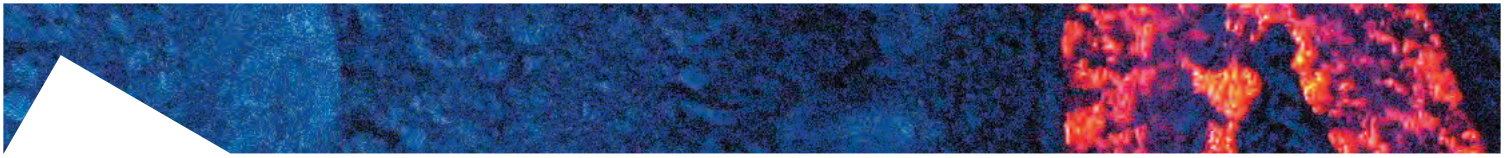


Fig. 1 | Back-scattered electron images of selected experimental run performed at 3.5 GPa with different temperature and buffers analysed.

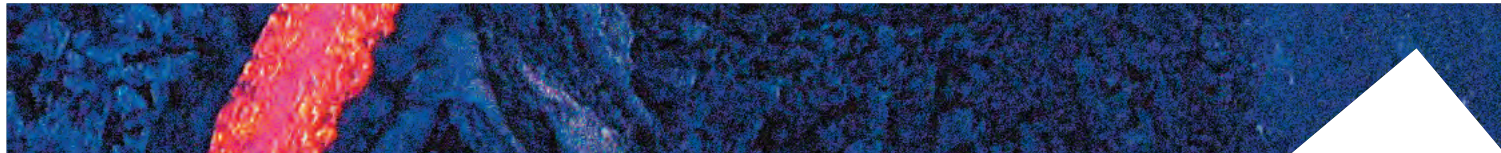
Abbreviations: tour=tourmaline; grt=garnet; crn=corundum; ky=kyanite.



yses on the recovered quenched products were analyzed using a Jeol JSM-6500F scanning electron microscope and a Jeol JXA-8200 electron microprobe also available at INGV (Rome). An example of recovered quenched products is shown in Figure 1a and b.

Our data supported by accurate analyses by X-ray diffraction show the crystallization of tourmalines such as fluor-schorl, fluor-dravite and dravite along with Al-rich phases such as kyanite, mullite, corundum and almandine garnet with the increase of temperature. Additional phases like iron-rich jadeitic pyroxenes might form as a result of oxidation of Fe^{2+} to Fe^{3+} of the starting material.

These experiments provide an evidence of the gradual dehydration and loss of B through decomposition of schorl at several steps. These breakdown process results, therefore, to the origin of hydrated B-rich fluids at local scale upon subduction at high pressure and temperature at higher P-T conditions than previously proposed.

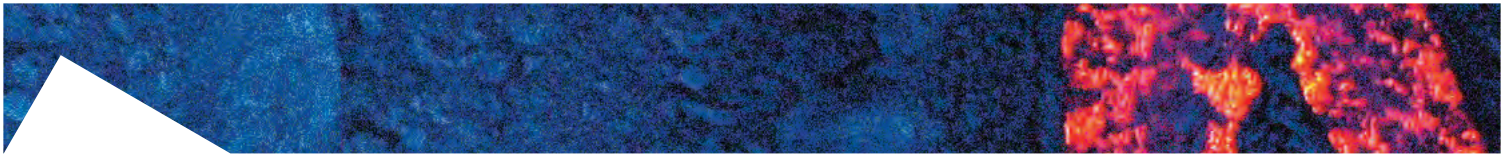


Chlorine as a discriminant element to establish the provenance of central mediterranean obsidians

Foresta Martin F., Rotolo S., Carapezza M., Nazzari M.

Since the pioneering studies of the first half of the 1900s concerning the geochemistry of Chlorine, it has been found that some volcanic glasses may have percentages of this element significantly higher than that found in the average of igneous rocks. For example, in some rhyolitic obsidians Cl exceeds 0.40% by weight (even up to 1% in peralkaline pantelleric obsidians), compared to an average of 0.02% in lithospheric igneous rocks. This feature indicates that Cl is a highly incompatible element that tends to concentrate in SiO_2 -rich melts, rather than being fixed in the crystalline lattices of minerals. Unlike other volatile constituents such as CO_2 and S, which escape through outgassing of rising magma, the high solubility of Cl in silicate melts, even at relatively low pressures, characterizes it as an element capable of providing useful information on the volcano-genetic processes, and on the eruptive dynamics. Starting from these considerations, we planned to verify to what extent Cl, alone or associated with other major and minor elements, can help in discriminating the four sources of obsidian exploited in prehistoric times in the Central Mediterranean, namely: Mount Arci, Palmarola, Lipari and Pantelleria. The recognition of the distinctive geochemical footprint of the obsidian sources is usually done combining major and minor element contents with those of trace elements, since the formers, by themselves, often give ambiguous results. Some studies tried to identify the sources of obsidian by carrying out on the archaeological findings only analysis of some major and minor elements (SiO_2 , Al_2O_3 , Na_2O , K_2O , CaO , MgO , MnO , Fe_2O_3 , TiO_2). The use of a series of binary diagrams with pairs of these oxides may in some cases leads to effective discrimination. But in other cases, the compositional variability of these elements in archaeological obsidians is so great to prevent a clear source attribution. By examining over 200 analyses, performed with an EMPA electronic microprobe, both on representative samples of the four Mediterranean obsidian sources, and on archaeological findings whose provenance had already been ascertained with previous studies, we noted the following:

- the Cl content changes from one primary obsidian source to the other, without overlapping, with the following



sequence (average values expressed in wt.%): M. Arci ~0.12%; Palmarola ~0.22%; Lipari ~0.34%; Pantelleria ~0.50%;

- Cl is negatively correlated with silica, but the SiO_2 vs. Cl binary diagram does not effectively discriminate the four obsidian sources (Figure 1 left);
- Cl is positively correlated with Na_2O (indirectly with alkalinity and peralkalinity of the melt), and the related binary diagram effectively discriminates the four primary obsidian sources (with a likely Pantelleria sub-source; Figure 1 right).

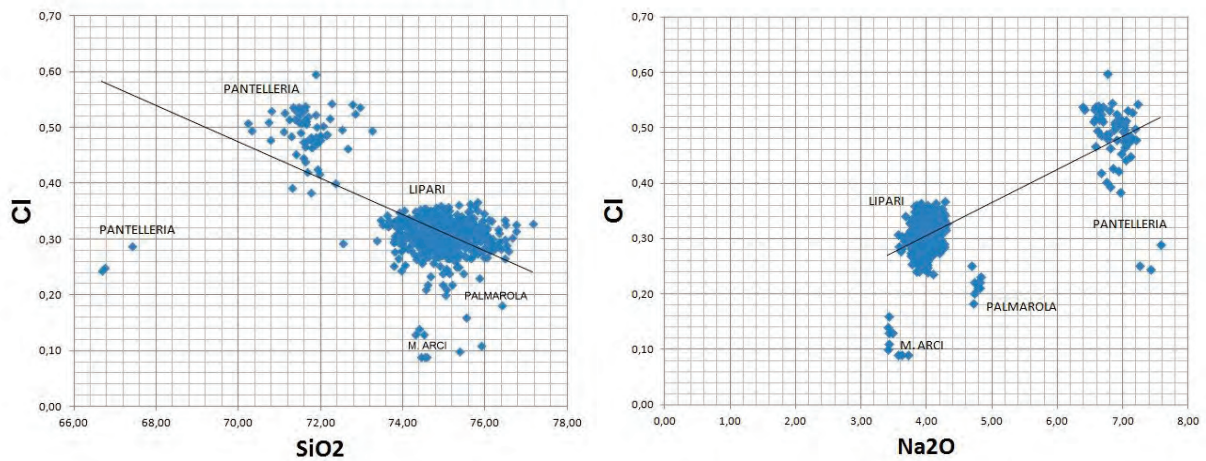
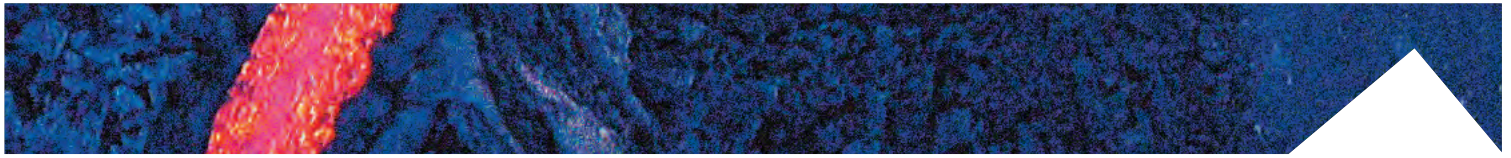


Fig. 1 | Chlorine vs. Silica and Na_2O (weight %) in the obsidians of four Mediterranean sources.



Voluminous crustal degassing and immiscible sulfide genesis caused by magma-shale interaction in Large Igneous Provinces

Deegan F.M., Bédard J.H., Troll V.R., Dewing K., Geiger H., Grasby S.E., Misiti V., Freda C.

Large Igneous Province (LIP) activity is hypothesized to impact global volatile cycles causing climate changes and environmental crises deleterious to the biosphere. Recent work suggests that the potential of LIPs to impact climate is magnified where they intrude organic-rich (i.e. shale-bearing) sedimentary basins. However, the chemical and degassing dynamics of magma-shale interaction are not well understood. Here we present the first experimental simulations of disequilibrium interaction between LIP magma and carbonaceous shale during upper crustal sill intrusions in the Canadian High Arctic LIP (HALIP), the latter of which were co-eval with oceanic anoxic event 1a (Figure 1). Experiments show that magma-shale interaction results in intense syn-magmatic degassing and simultaneous precipitation of sulfide droplets at the ablation interface. Magma-shale interaction on a basin-scale can thus

generate substantial amounts of climate-active H-C-S volatiles, while the presence of strongly reducing volatiles may also increase the likelihood of magma to segregate a sulfide melt. These findings have fundamental consequences for our understanding of both large-scale Earth outgassing and metal prospectivity in sediment-hosted LIPs.

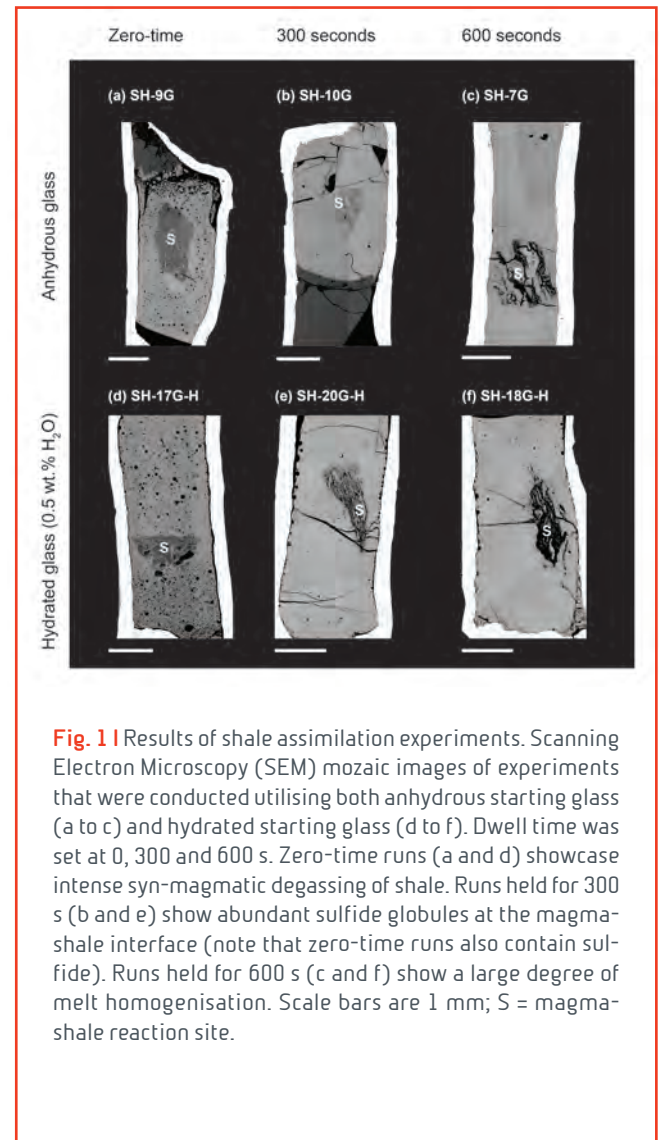
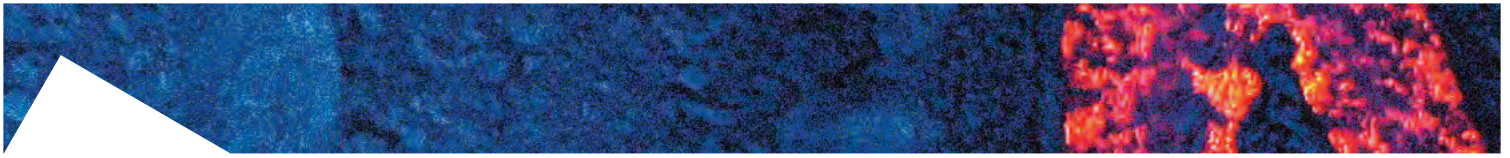


Fig. 1 Results of shale assimilation experiments. Scanning Electron Microscopy (SEM) mozaic images of experiments that were conducted utilising both anhydrous starting glass (a to c) and hydrated starting glass (d to f). Dwell time was set at 0, 300 and 600 s. Zero-time runs (a and d) showcase intense syn-magmatic degassing of shale. Runs held for 300 s (b and e) show abundant sulfide globules at the magma-shale interface (note that zero-time runs also contain sulfide). Runs held for 600 s (c and f) show a large degree of melt homogenisation. Scale bars are 1 mm; S = magma-shale reaction site.



In situ resuspension of volcanic ash: a portable wind tunnel facility

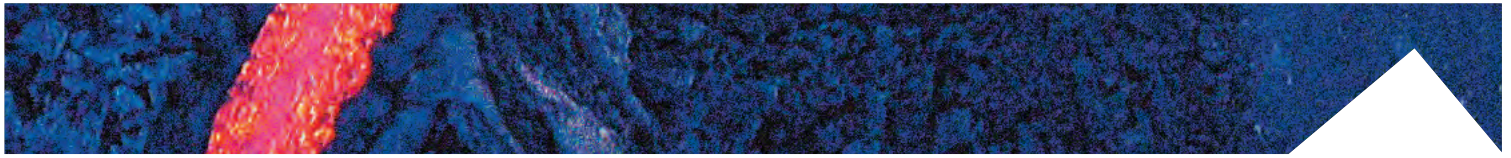
Del Bello E., Taddeucci J., Merrison J., Rasmussen K.R., Iversen J.J., Scarlato P., Ricci T., Andronico D.

The resuspension of volcanic ash deposits by wind is a well-known source of hazard following explosive eruptions. Besides the mail control exerted by the local wind field, ash resuspension is also influenced by: 1) atmospheric humidity; 2) features of the deposit (grain size distribution, sedimentary structures, etc.), and 3) features of the substrate (i.e. moisture, roughness). Ash resuspension is modeled using numerical simulations, which however require physical characterization and identification of the critical parameters controlling ash resuspension. Wind tunnel studies on volcanic particles are very limited and restricted to laboratory parameterizations, with in-situ effects not been pa-

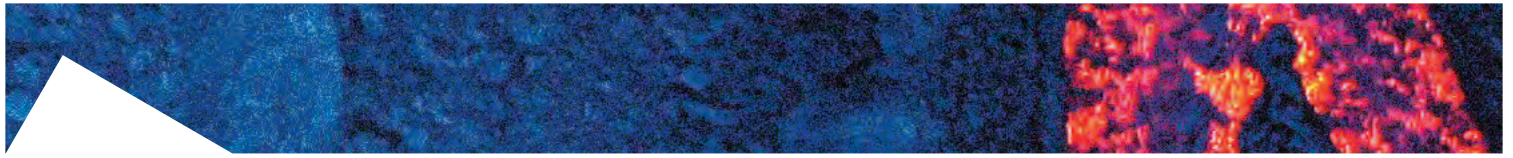


Fig. 1 | Deploying the portable wind tunnel in Argentina (October 2019), to study the resuspension of volcanic ash deposited from Cordon Caulle 2011 (Chile) eruption.

rameterized. Sakurajima volcano (Japan) is well known for its frequent ash-rich explosions, injecting thousands of kilob of ash per month into the atmosphere, most of which settles in the proximal areas of the volcano. This deposited ash is continuously resuspended by winds, causing trouble to people living in the surrounding villages, and, depending on the wind strength, carried over into the nearby city of Kagoshima. In 2019, we deployed a custom-designed portable wind tunnel in the areas around Sakurajima (Japan) and Bariloche (Patagonian Argentina) to study the in



situ resuspension of relic volcanic ash in a variety of the above conditions. The wind tunnel is calibrated with both LDA and pitot tubes measurements. The device allows generating a controlled wind profile within a 110x12x12 cm test section, which is placed directly on an untouched test bed of naturally deposited ash. Two types of experiments were performed: 1) ramp up speed experiments, where the wind speed is increased until reaching the threshold friction speed on four different substrates; 2) constant speed experiments, where three wind speed values were kept for 20 minutes using the same substrate. The threshold friction speed is measured with a hot wire anemometer, and the movement of resuspended ash is detected by means of multiple high speed and high definition digital camcorders. In-situ measured threshold friction speeds are compared to 1) in situ observed episodes of resuspension driven by local winds and (Figure 1) 2) laboratory determination of threshold friction speed in controlled environmental conditions, and using the same ash deposited homogeneously.



The 3 July and 28 August 2019 Paroxysms of Stromboli

Andronico D., Del Bello E., Ciancitto, F.A. Cristaldi, A. D’Orlando C., Landi P., Pennacchia F., Ricci T., Scarlato P., Taddeucci J.

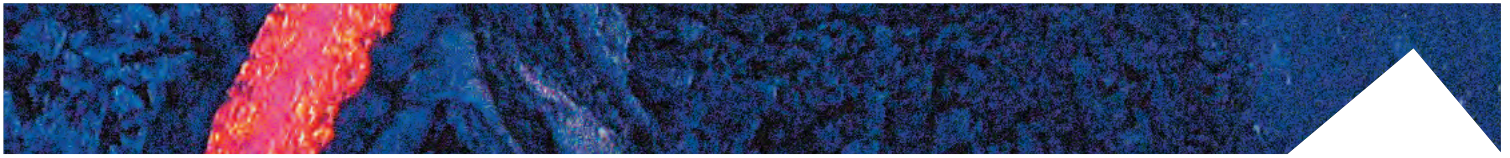
On 3 July and 28 August 2019, two large paroxysms - explosions up to several orders of magnitude larger in intensity and magnitude than ordinary explosions- occurred in Stromboli, Italy, during a phase of more intense Strombolian activity. Two minutes before the 3 July paroxysm, we observed lava being pushed out of two vents by the rising, gas-rich magma underneath. Then, an impressive blast initiated from the SE vents, accompanied by pressure waves clearly felt at the two coastal villages located up to 2.5 km from the vents. Meter-sized ballistic spatters reached



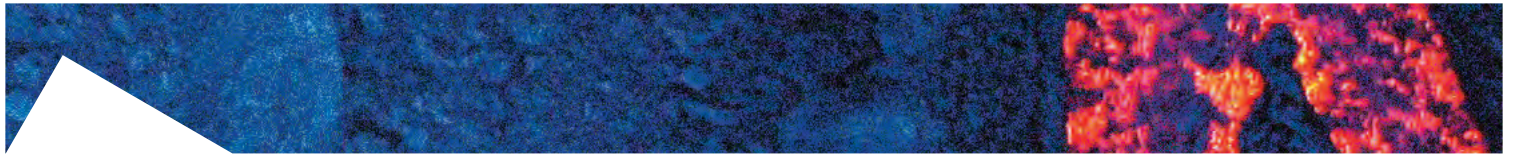
Fig. 1 | Stromboli, Pizzosopra la fossa as it appeared a few days (left side) and three months after the 28 August paroxysm. Note the bomb-size dimension of the products erupted during the paroxysm, eventually covered by ash-lapilli size products of the ordinary activity. Pictures Daniele Andronico.

several hundreds of meters down the slope of the volcano, and an eruptive column rose more than 4 km above the summit. Two pyroclastic currents descended from the NW flank into the sea, causing decimeter-sized tsunami waves that were still measurable up to hundreds of km away. Tephra and ballistic fallout triggered wildfires mainly along the SW slopes. After the paroxysm, the volcano produced energetic explosive activity at the summit and lava flows descending the upper slopes. The 28 August paroxysm occurred during this intensified period activity, and with characteristics very similar the 3 July one, but with no clear short-term variation in intensity/frequency of the explosive events.

Prompt field campaigns enabled us to map and sample the deposits after minimal reworking. The summit area was



largely covered by a continuous spatter deposit, while pumice lapilli from the plume were dispersed SW and covered one of the two villages. A dispersal map of the tephra deposits, grain-size, componentry, textural and morphological analyses of the pyroclasts, and petro-chemical analyses on juvenile clasts are being performed. Finally, an in-depth analysis of a large amount video-footages and images posted by social media users will be used to infer the complex dynamics and evolution of eruptive phenomena, and then compared with the 2003 and 2007 paroxysms (Figure 1).



Crystal-chemical variations of spinel, clinopyroxene and plagioclase solidified under variable cooling rates from a MORB melt

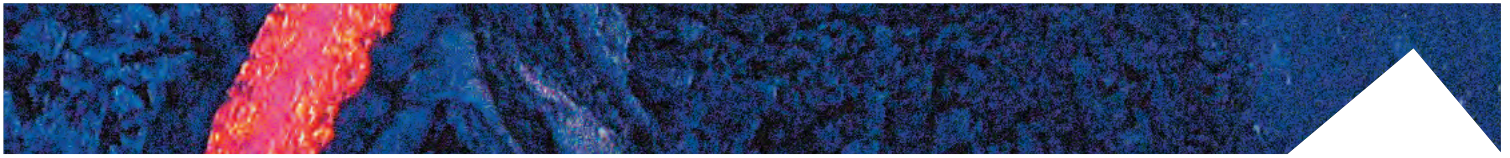
Giuliani L., Iezzi G., Vetere F., Nazzari M., Behrens H., Mollo S., Ventura G., Cavallo A., Scarlato P.

Solidification experiments on an Icelandic MORB were used to quantify the chemical gradients as a function of kinetic conditions. Experiments were performed at P_{atm} and fO_2 of air, in a thermal range of cooling (ΔT_c) between 1300 - 800 °C, using cooling rates ($\Delta T/\Delta t$) of 1, 7, 60, 180, 1800 and 9000 °C/h. The paragenesis of the run products is mainly composed by plagioclase (plg), clinopyroxene (cpx), spinel (sp) and glass. Plagioclases can nucleate up to 60°C/h and their disappearance coincides with the development of dendritic shapes for cpx and sp.

The influence of $\Delta T/\Delta t$ on the textural variations of sp, cpx and plg have been widely quantified in a previous work, in which maximum (G_{max}) and average (GCSD) crystal growth rates have been computed. Here we quantify the chemical gradients into sp, cpx, plg and glass, evaluating the variations of the major oxide elements (wt.%), cation abundances (a.p.f.u.) and molecules (mol.%) as a function of $\Delta T/\Delta t$. Micro-chemical features were measured either with EPMA-WDS and SEM-EDS. The increase of $\Delta T/\Delta t$ causes: 1) an increase of Al_2O_3 in sp and a decrease of TiO_2 and Fe_2O_3 ; 2) a slight decreasing of SiO_2 , MgO and CaO in cpx, while Al_2O_3 , Fe_2O_3 and Na_2O generally increase; 3) SiO_2 , Fe_2O_3 , CaO and Na_2O in plg remain almost constant, while Al_2O_3 slight decreases. The a.p.f.u. trends generally follow the same variations as the major oxide elements, highlighting that in cpx the Al^{3+} variations are mainly due to the M1Al increasing. Molecular variations show that the increasing of $\Delta T/\Delta t$ causes the decreasing of Mag and Di + CaFeTs respectively for sp and cpx, while An and Ab content for plg is not influenced by kinetic conditions.

Intracrystalline glass (i.e. glass at distance $\leq 50 \mu m$ from the crystal rims) is present only for $\Delta T/\Delta t$ of 180 and 1800 °C/h, showing chemical variations that reflect the rapid growth of the surrounding crystalline phases. Matrix glass (i.e. glass farther than 50 μm from the crystal rims) is observed only for $\Delta T/\Delta t \geq 1800$ °C/h, displaying very low variability in compositions, almost identical to that of the bulk system.

The measured chemical gradients suggest that the compositions of crystalline phases approach to those of *equilibrium* crystallization conditions for $\Delta T/\Delta t \leq 60$ °C/h.



Many of the variations of the major oxide elements, like those for Fe_2O_3 in sp, CaO in cpx and SiO_2 , Al_2O_3 , Fe_2O_3 and MgO in plg, are linearly related to the increasing of $\Delta T/\Delta t$. Identical considerations could be done for Fe^{2+} , Fe^{3+} and Ca in cpx, and Si, Al and Fe^{3+} in plg, as well as $\text{Fe}^{2+}/\text{Fe}_{\text{tot}}$

and Mg# in cpx. Similarly, some molecules of sp and cpx, like Mag, Fs and CaFeTs, also show high linear trends as a function of $\Delta T/\Delta t$.

Linear relationships have been also found between cpx-cations, as well as their most abundant molecules, as a function of kinetic conditions. Moreover, the high correlations between G_{max} and G_{CSD} versus sp, cpx (Figure 1) and plg chemical gradients, give for the first-time quantitative relationships between texture, crystal chemistry and kinetics.

All these functions are used as geospeedometers in order to retrieve the kinetic solidification conditions and quantitatively model the crystallization processes in MORBs.

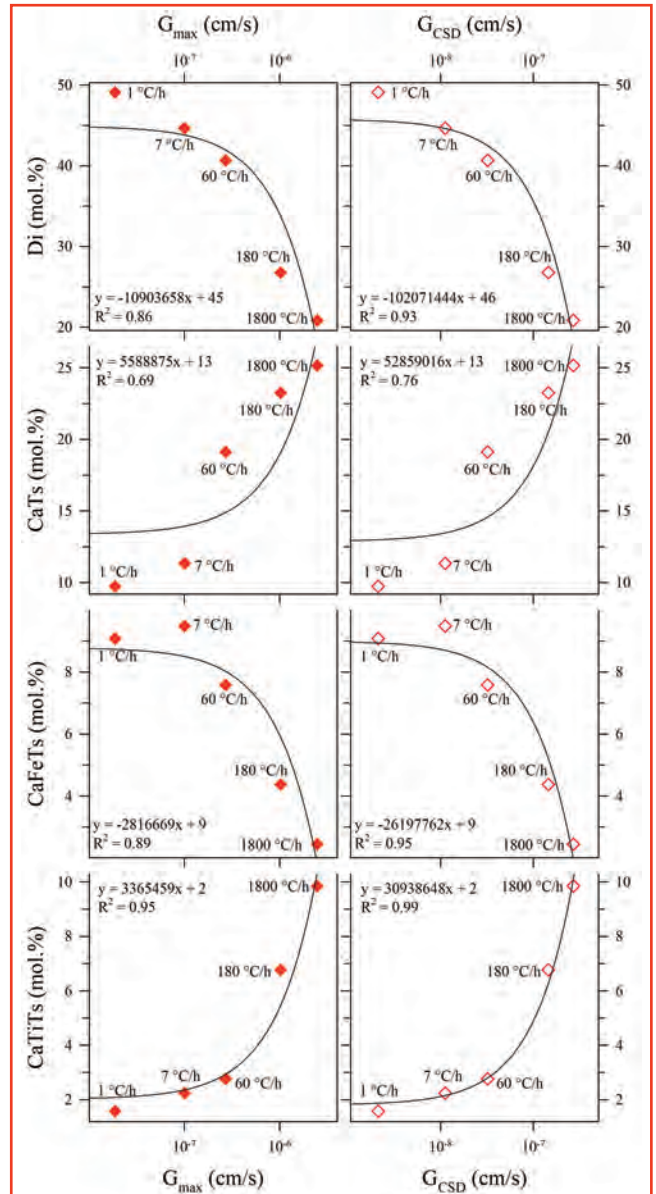
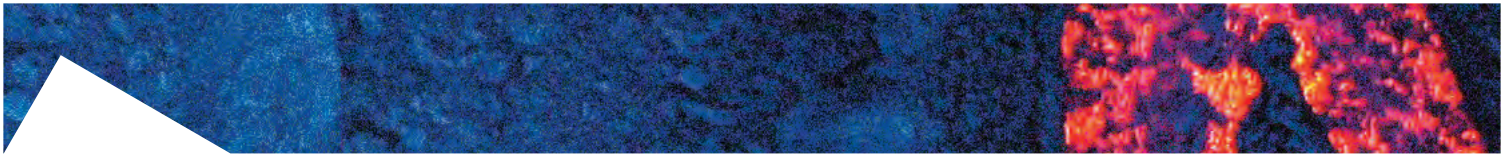


Fig. 1 | Relationships between maximum and average growth rates (G_{max} and G_{CSD}) and some cpx-molecules (mol.%). Found linear trends are highly related to the increasing of cooling rate ($\Delta T/\Delta t$).



The Onano Eruption (Lattera Volcano, Central Italy)

Landi P., D'Oriano C.

A detailed chemical and mineralogical study of the products erupted during the Onano Eruption was performed with the aim to draw a picture of the complex pre-eruptive plumbing system and the sin-eruptive dynamics.

The Onano Eruption (~0.17 Ma), also known in the literature as “*Vulcanite complessa di Onano*”, is the second to last caldera forming eruption of the Lattera volcano, in the northernmost sector of the Roman Comagmatic Province (Latium, Central Italy).

The chemical composition of pumice and scoriae ranges from phonotephrite to phonolite, but there is not a regular compositional variation with the stratigraphic height. Textural investigations and bulk rock, mineral and glass analyses

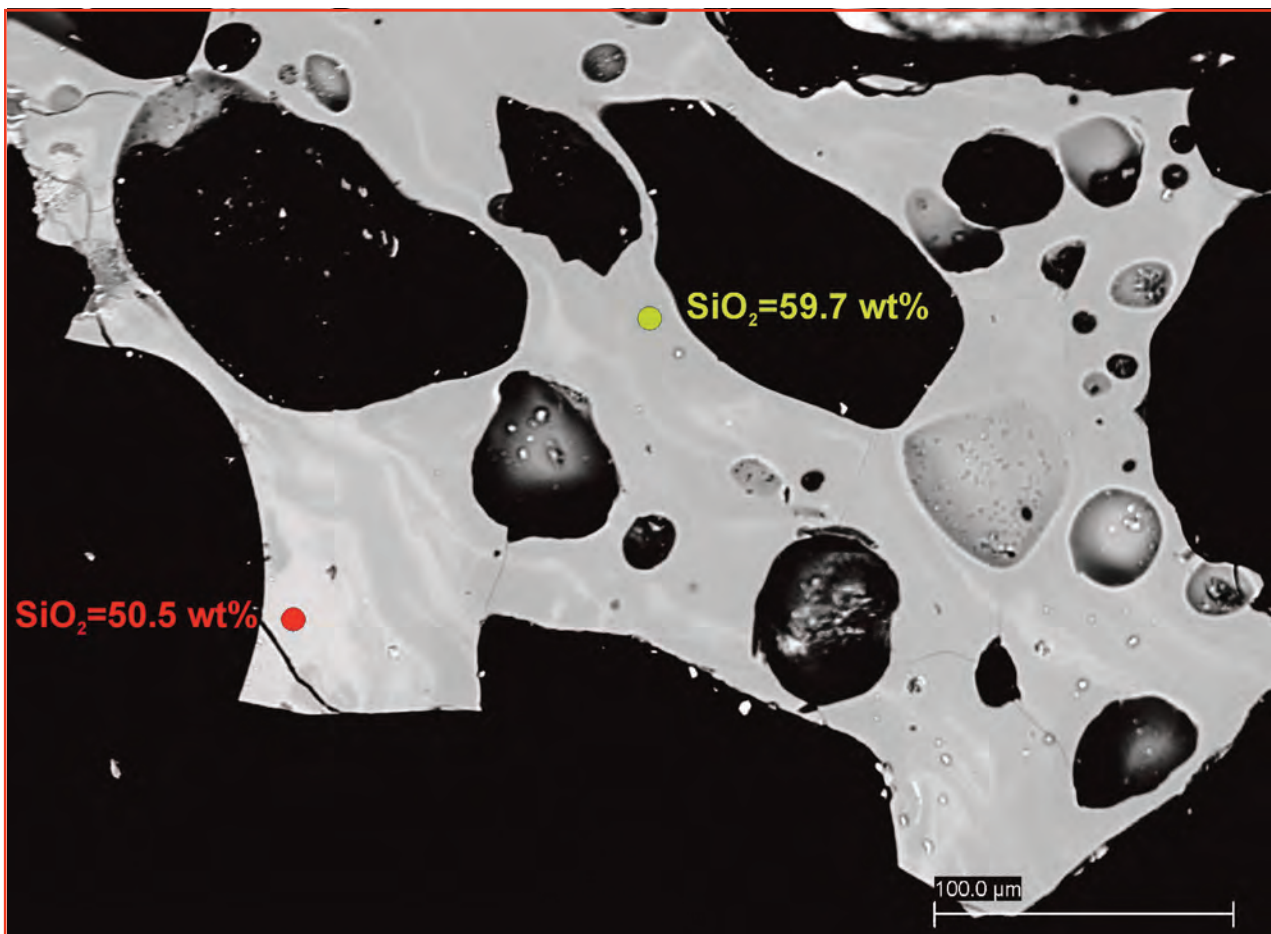
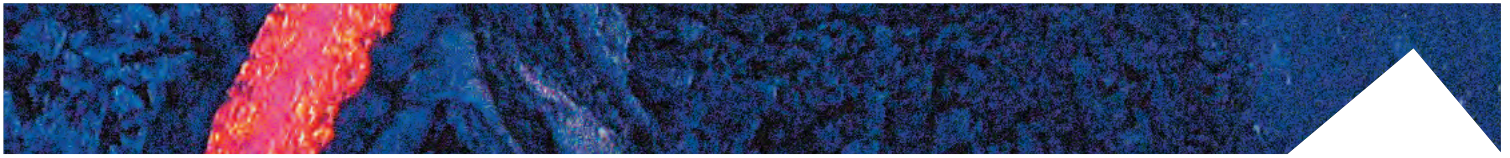
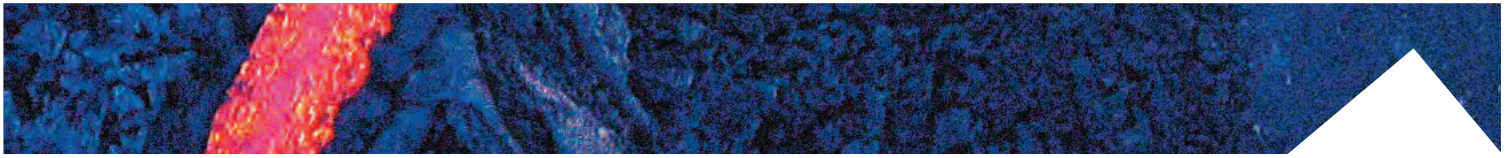


Fig. 1 | Inhomogeneous composition of the groundmass in the scoria emitted at the beginning of the caldera collapse during the Onano Eruption.



reveal that the entire eruptive sequence is typified by juvenile components with variable composition within a single depositional unit and commonly within a single clast. This indicates that the pre-eruptive zoning of the magma chambers was partially to totally disrupted during the eruption. Mingling between tephriphonolitic and phonolitic melts are present in different proportions during the first phases of the eruption, while during the caldera collapse all the magma chamber is involved leading to sin-eruptive mingling which became more and more extensive as the eruption proceeded.

The results obtained from the study of this old eruptive sequence give insights into the pre-eruptive magma conditions and sin-eruptive magma dynamics driving the eruptive behavior of the potassic active volcanoes in Italy (Figure 1).



Transformation of Cu-slag and glass wastes in new glass-ceramics

Giuliani L., Gualtieri M., Vetere F., Siligardi C., Iezzi G.

This study deals with a new glass-ceramic material obtained by two ends of life (EoL) materials, produced by industrial processes. The powdered starting material was obtained by mixing 75 wt.% of metallic wastes and 25 wt.% of soda-lime-silica glass. This mixture was heated up to 1550 °C, annealed and homogenized for 20 min and finally cooled at rates of 10, 100 and 500 °C/h down to the quenching temperature of 150 °C. An additional experiment was run to direct quench the melt from 1550 °C to ambient temperature, such to verify homogeneity and define the bulk composition of the melted system. The starting composition of the starting recycled materials is $\text{SiO}_2 = 27.1$, $\text{Al}_2\text{O}_3 = 28.7$, $\text{Fe}_2\text{O}_3 = 32.7$, $\text{ZnO} = 4.6$, $\text{MgO} = 1.2$, $\text{CaO} = 4.0$, $\text{Na}_2\text{O} = 2.9$ wt.%.

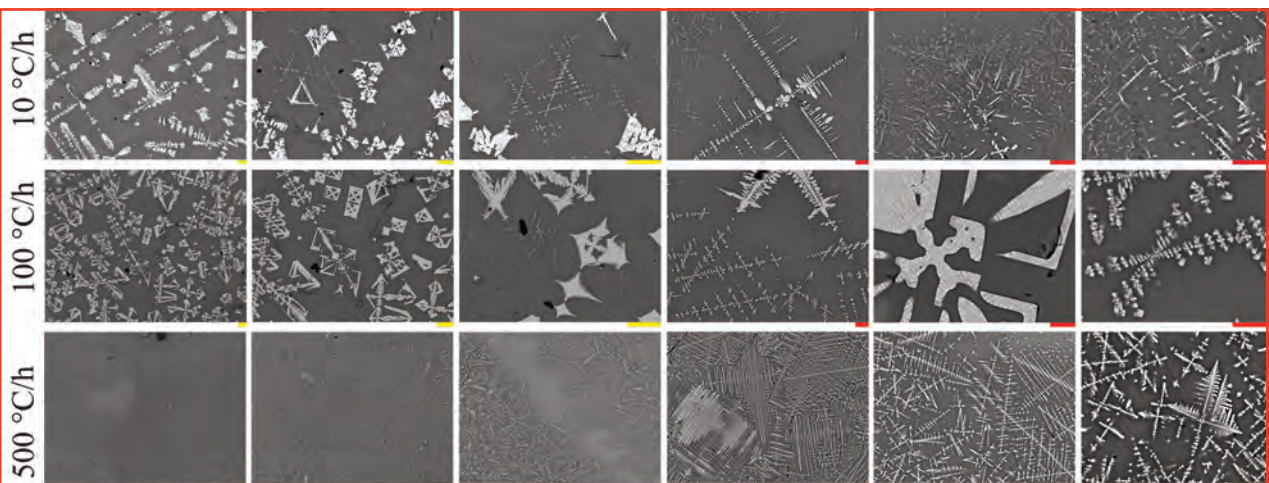
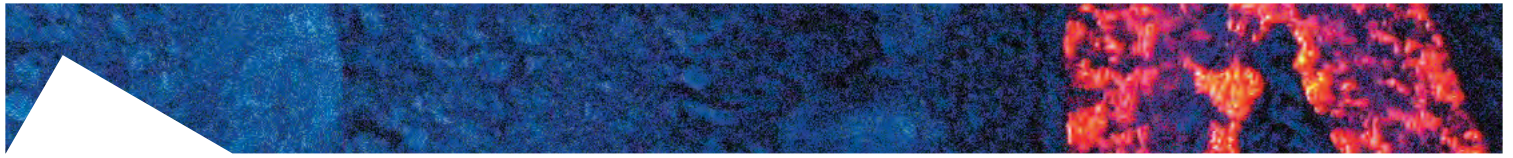


Fig. 1 | BS micro photos acquired by SEM and EPMA of the run products at different magnifications (from 40 to 250x for experiments at 10 and 100 °C/h, and from 200 to 1500x for the experiment at 500 °C/h); yellow and red bars correspond to 100μm and 10μm, respectively.

These four run products were analyzed by SEM-EDS to obtain several BS-images at magnifications from 100 to 5000 x. EPMA-WDS analysis was used to quantify phase compositions on an area as low as few μm^2 , plus chemical profiles on crystals and glass with areas of hundred μm^2 up to mm^2 . The solidified phases in all the run products are silicate glass and spinel-like crystals (Figure 1); these latter are mainly composed by Fe, Zn, Al, and Mg, plus other minor metals, like Cu and Cr. Crystals show dendritic shapes with sizes changing from mm to few tens of μm as the cooling

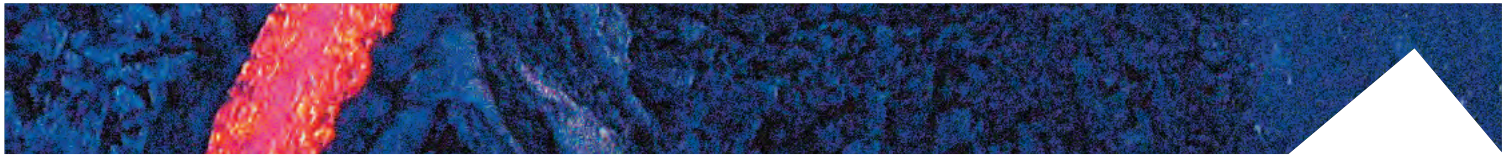


rate increases (Figure 1). Crystal amount (area%) was quantified by image analysis and increases as the cooling rate increase passing from 14 to 26 and 30 area% at 1, 100 and 500 °C/h, respectively. Glass area% follow the opposite trend.

Crystal-chemical features can be quantified on crystals solidified at 10 and 100 °C/h, because those in the run product cooled at 500 °C/h are very tiny. The increase of the cooling rate causes an increase of Al_2O_3 and CaO and a decreasing of the ZnO content into the spinel lattice, while MgO remains almost constant. Glass experiences a slight increase of FeO , ZnO , MgO and a slight decrement of K_2O . Instead, Al_2O_3 , CuO , CaO and Na_2O show more complex trends, first increasing from 1 to 10 °C/h and then decreasing at 500°C/h.

In addition to EPMA analysis, crystal-chemistry was investigated also by X-ray powder diffraction (XRPD), such to define the solidified mineralogical phases. All crystals in the run products result to be a solid solution along the magnetite to hercynite spinel join.

These preliminary outcomes will be integrated with the magnetic and thermometric analysis, such to quantify the capacity of this new glass-ceramic to absorb microwave. It is note of worth that the cooling rate is able to significantly change the textural and crystal-chemical characteristics of these recycled materials.



Textural variations along a vertical section of a distal portion of an Etnean lava flow

Giuliani L., Iezzi G., Lanzafame G., Ferlito C., Nazzari M., Casarin A., Piattelli V., Mollo S., Scarlato P.

This study focuses on the textural variations along a vertical section of an Etnean lava flow, cropping out at 3 km from the vent, in the Valle del Bove. The lava surface is pahoehoe and was erupted during the 1991-1993 period. Nine oriented samples were collected, cut and polished along the vertical lava flow section from the carapace (LV9) to the lowest portion (LV1), with sampling distance of 20 cm. From these samples, 9 oriented thin sections were extracted and analysed by high-resolution scanner (HRS) and transmission optical microscopy (TOM) to measure bubbles ≥ 0.5 mm and crystals ≥ 0.1 mm, respectively. Bubbles up to 0.07 mm and crystals up to 0.2 (plg and cpx + ol) and 0.03 mm (sp), were measured on BS-SEM puzzles (sequential images at 95 x). Image analysis was applied to quantify phases amount (area%), number of minerals and bubbles per area ($\#/A$), orientations ($^\circ$) and sizes (μm) of phases, as well as bubble-(BSD) and crystal-size distributions (CSD; Figure 1). From LV9 (top) to LV1 (bottom), bubbles decrease from ~ 30 to 10 area%, while their $\#/A$ (mm^{-2}) increases from ~ 1 to 9 mm^{-2} . From LV1 to LV7, cpx + ol slightly decrease from ~ 40 to 25 area%, then suddenly increase to about 45 area% for LV8 and LV9. An opposite trend is followed by plg, while the amount of sp does not change significantly. The $\#/A$ of cpx + ol and plg remains almost constant across the lava section and close to 1 and 2 mm^{-2} , respectively. Differently, $\#/A$ of sp shows a more complex trend which roughly decreases from LV1 to LV9. The 2D orientations of the major axes were defined respect to the vertical. The long side of bubbles show a low 2D variability, except in LV4 (tube-like) and LV9. Conversely, plg and cpx + ol are mainly 2D oriented along preferred direction(s), but with no specific trend from LV1 to LV9. The maximum bubble size decreases from 20 to 0.5 mm from LV9 (top) to LV1 (bottom). Except for LV5, the aspect ratio of bubbles always approaches the 1:1 circular 2D shape. The 2D crystal sizes of cpx + ol, plg and sp reach maximum values of 10, 2, and 0.5 mm, respectively, poorly changing along the vertical section. All bubbles in LV1-to-LV3 and LV6-to-LV7 are ≤ 0.3 mm, while in the other samples the bubbles reach a 2D length of 2 mm. Crystal size does not change significantly along the vertical lava section: most of cpx + ol and plg have lengths between 0.5 and 1 mm. More than the 90% of sp crystals are less than 0.05 mm in length. From LV9 to LV1, BSDs show a linearization, an increase of slope and decrease of size ranges

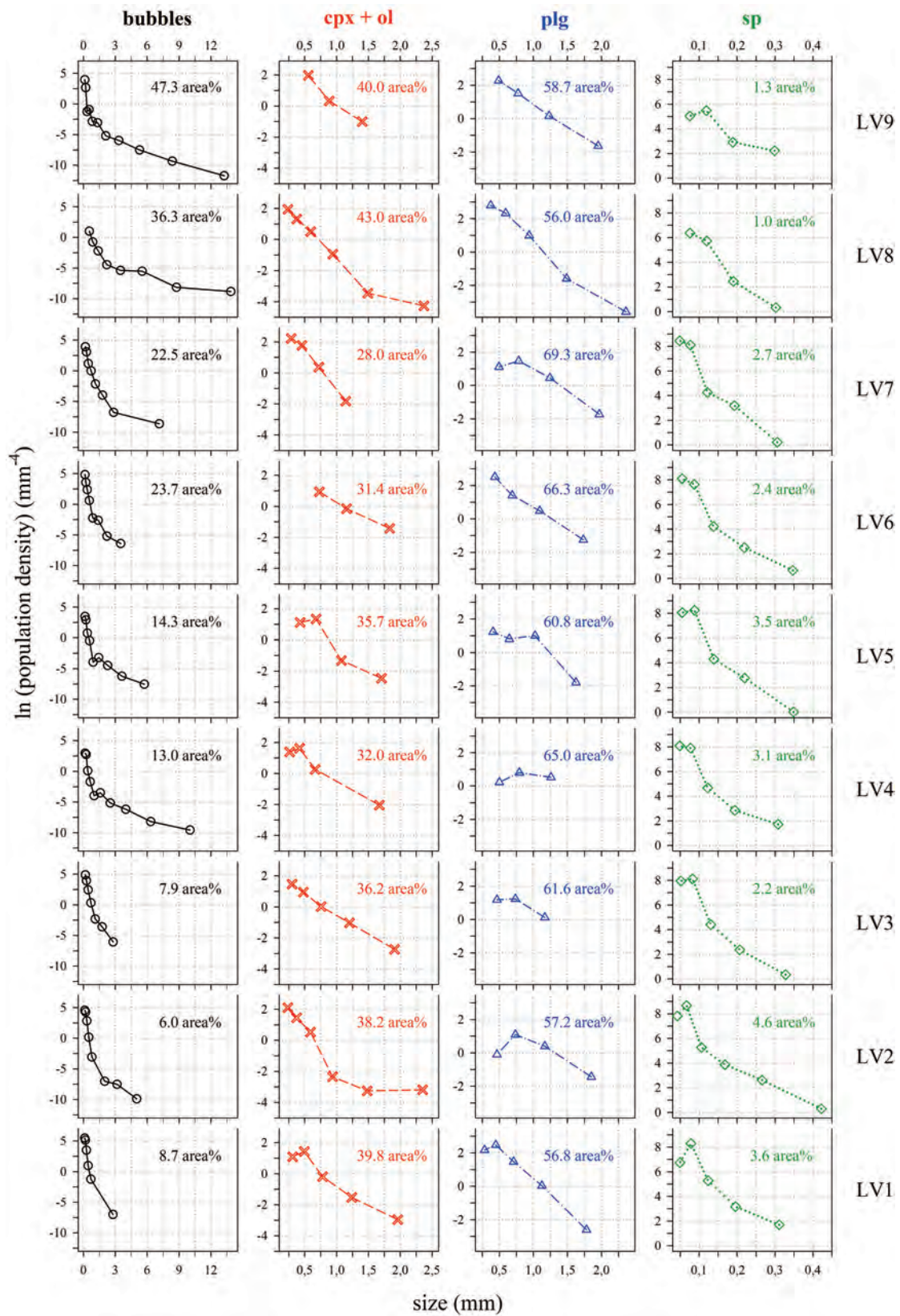
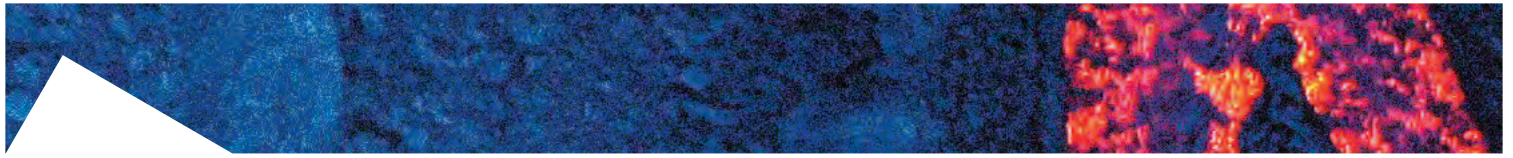
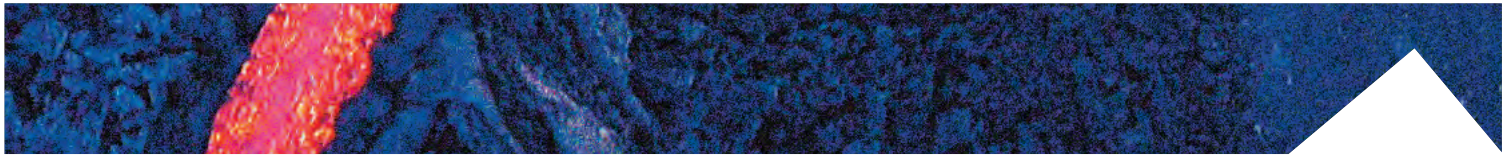
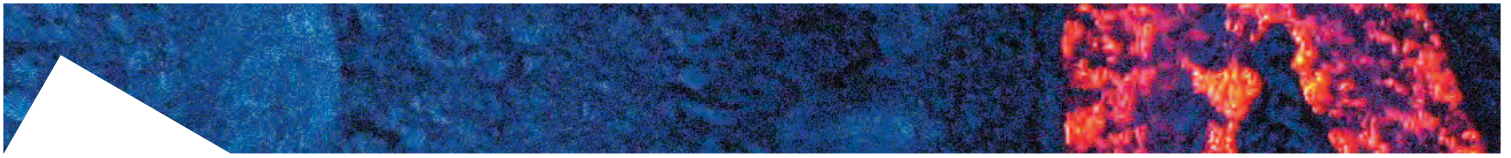


Fig. 1 | Bubble size distribution (BSD) and crystal size distribution (CSD) of plg, cpx + ol and sp, with their relative crystal contents from top (LV9) to bottom (LV1) of the lava flow.



(Figure 1); the only exception is LV4 containing tube-like bubbles. The CSDs of cpx + ol and plg do not show any clear trend from LV1 to LV9; counter-clockwise slope of the smallest sizes in LV1, LV4 and LV5 (cpx + ol) and LV1, LV2, LV4 and LV7 (plg) are indicative of crystal agglomeration phenomena. The same holds for sp, except in LV4, LV6, LV7 and LV8 (Figure 1). These outcomes indicate that degassing, ascent of bubbles and their coalescence still occur after eruption, even at several km away from the vent. Thus, the investigated lava remained very hot and with a low crystal content during the flow. Crystallization processes induced by lava cooling and degassing are important even at significant distances from the eruptive vent.



Magmatic enclaves from Mt. Amiata volcanic complex

Lucci F., Conte A., Nazzari M., Della Ventura G.

Magmatic enclaves in effusive products represent one of the most important mineralogical and petrological archives to unravel the pre-eruptive history in the magmatic plumbing system.

These samples can in fact represent the earlier segregated minerals thus reflecting the magmatic environment (i.e., pressure-temperature, magma/fluid composition) through their textures, the mineral growth, the mineral and the whole-rock chemistry.

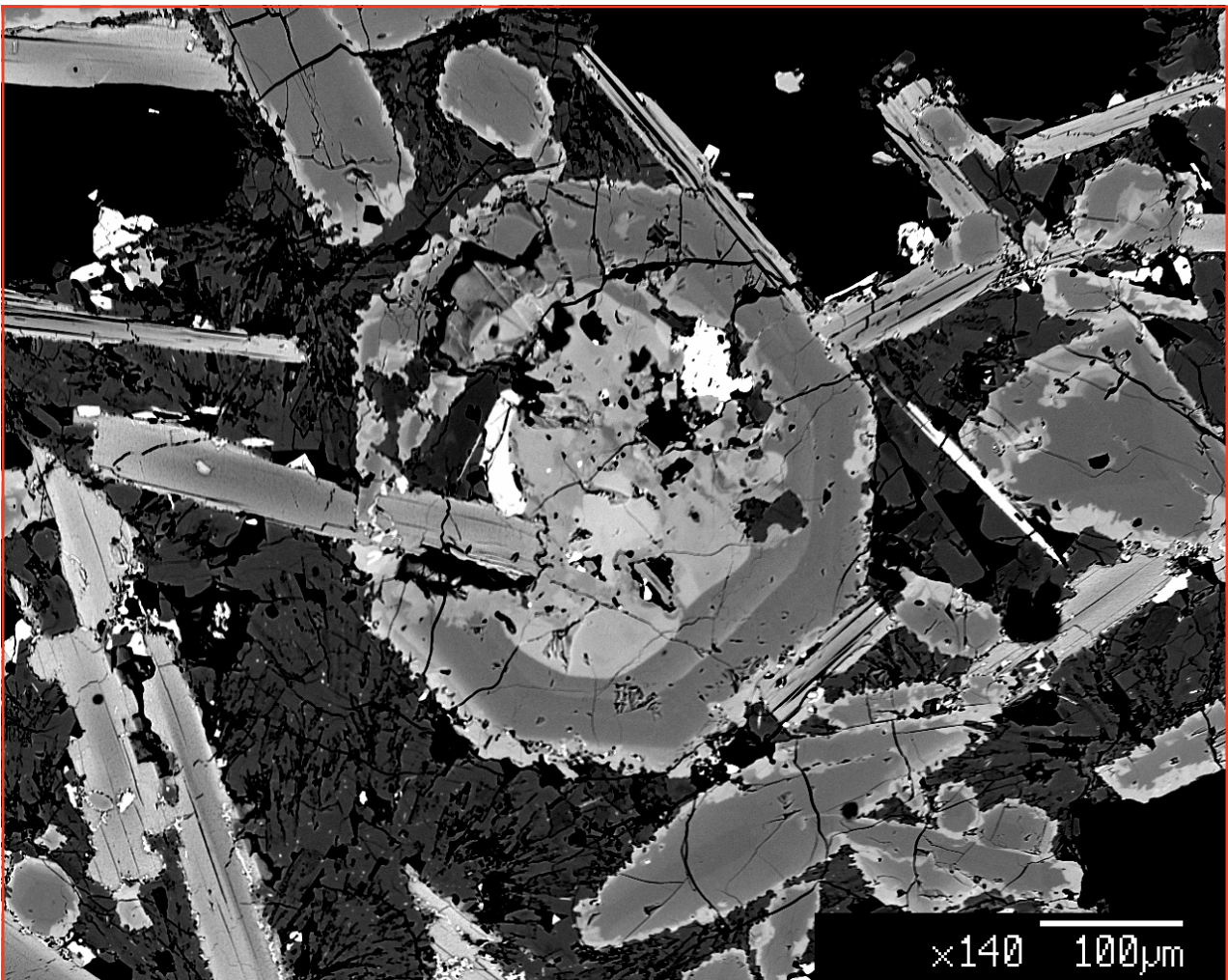
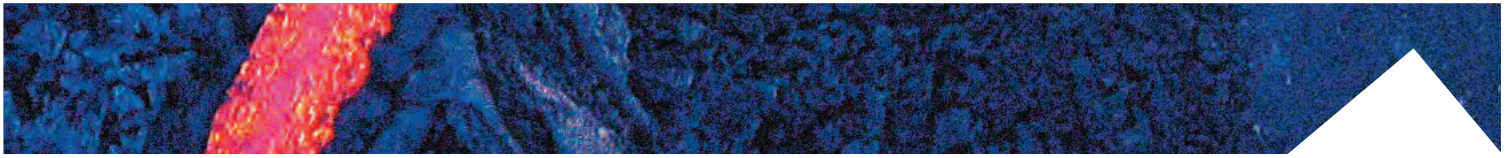


Fig. 1 | BSE image showing the typical texture and assemblage (Cpx+Pl+Bt+Sp) observed in Mt. Amiata magmatic enclaves, testifying a complex magmatic story. In particular it is possible to observe a clinopyroxene phenocryst characterized by a resorbed patchy core, high-amplitude oscillatory zoning inner rim and resorbed step-zoning outer rim.

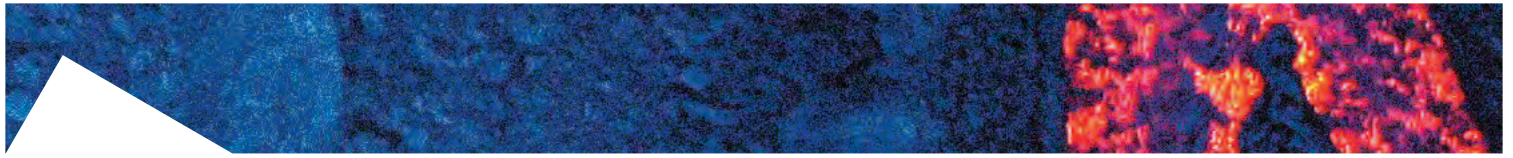


Accordingly, petrographic observations and chemistry of the primary assemblages of enclaves, integrated with opportunely selected mineral-melt thermobarometry models could allow defining the pressure-temperature conditions of the feeding system(s) of the erupted products of a volcanic complex.

In this ongoing project, we focus on the petrological, mineralogical and geothermobarometry modeling of magmatic enclaves included within the effusive rocks erupted during the Pleistocene (ca. 0.2-0.3 Ma) from Mt. Amiata volcanic complex (southern Tuscany), one of the youngest evidences of the so-called Tuscan Magmatic Province (TMP).

Our data and the novel results will be integrated with the (poor) existing information from the literature on the magmatism of the Mt. Amiata volcano. The final aim is at developing a conceptual model for the magmatic plumbing system active in this area during the Pleistocene age.

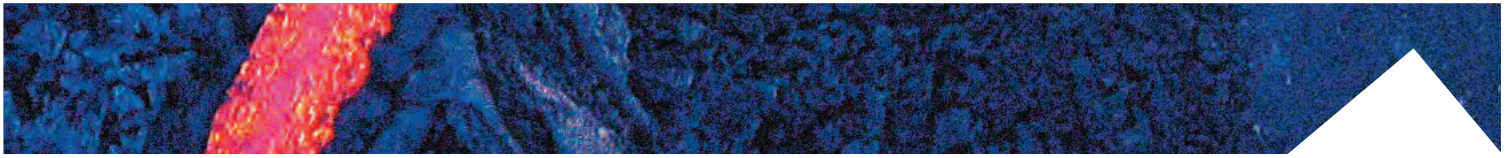
We believe that the workflow presented in this project could have also a general value and represent an efficient approach for a more general comprehension of pre-eruptive geometry of active volcanic systems.



The role of undercooling during clinopyroxene growth in trachybasaltic magmas: Insights on magma decompression and cooling at Mt. Etna volcano

Masotta M., Pontesilli A., Mollo S., Armienti P., Ubide T., Nazzari M., Scarlato P.

Isothermal and undercooling experiments were conducted on one of the most primitive trachybasalts from Mt. Etna volcano in order to examine the crystallization mechanisms controlling the textural and compositional variability of clinopyroxene. Experiments were performed at 400-800 MPa, 1050-1200 °C, 0-4 wt.% H₂O and at oxygen fugacity 2 log units above the Ni-NiO buffer. In isothermal experiments, the final resting temperature is approached from room temperature and clinopyroxene growth is dominated by an interface-controlled mechanism, leading to the formation of small (~10 μm) and euhedral crystals with homogeneous compositions. Conversely, in undercooling experiments, the final resting temperature is approached after annealing at temperature above the liquidus, imposing an effective degree undercooling (ΔT) to the system. In presence of undercooling, the crystallization of clinopyroxene is dominated by a diffusion-controlled mechanism that determines the formation of large (>100 μm) crystals, constituted by two compositionally distinct domains, enriched in Al₂O₃+TiO₂ and SiO₂+MgO, respectively. The maximum growth rate (G_{max}) decreases progressively from $\sim 10^{-7}$ to $\sim 10^{-8}$ cm/s as the degree of undercooling increases from ~20 to ~230 °C, due to the increase in nucleation rate. At low to moderate degrees of undercooling ($\Delta T=23-41$ °C) clinopyroxene is prevalently euhedral to subhedral, whereas at high degrees of undercooling, the crystal shape changes from prevalently subhedral ($\Delta T=73-123$ °C) to skeletal and dendritic ($\Delta T=132-233$ °C). Hourglass sector zoning similar to that documented for natural phenocrysts from eruptions at Mt. Etna volcano is observed only at low degrees of undercooling ($\Delta T=23-32$ °C). This type of zoning develops in the form of the cation exchange $[Si+Mg]_{(-111)} \leftrightarrow [Al + Ti]_{(100)}$ and demonstrates that hourglass sector zoning is an effective indicator of sluggish kinetic effects caused by relatively low degrees of undercooling. In contrast, at increasing degrees of undercooling ($\Delta T > 32$ °C), strong melt supersaturation determines the early formation of Al₂O₃+TiO₂-rich dendritic crystals and further SiO₂+MgO-rich overgrowths, as the bulk system attempts to return to a near-equilibrium state between the advancing crystal surface and the feeding melt.



The experimentally-determined relationship between ΔT and clinopyroxene chemistry is used to reconstruct the crystallization conditions of natural clinopyroxenes from 1974 and 2002-2003 eccentric eruptions at Mt. Etna volcano. Clinopyroxene rims record much higher degrees of undercooling (up to $\sim 110^\circ\text{C}$) than crystal mantles associated with magma recharge at depth (mostly $0\text{-}40^\circ\text{C}$). Hence, the rims track decompression-induced degassing and cooling during the ascent of magma towards the surface (Figure 1).

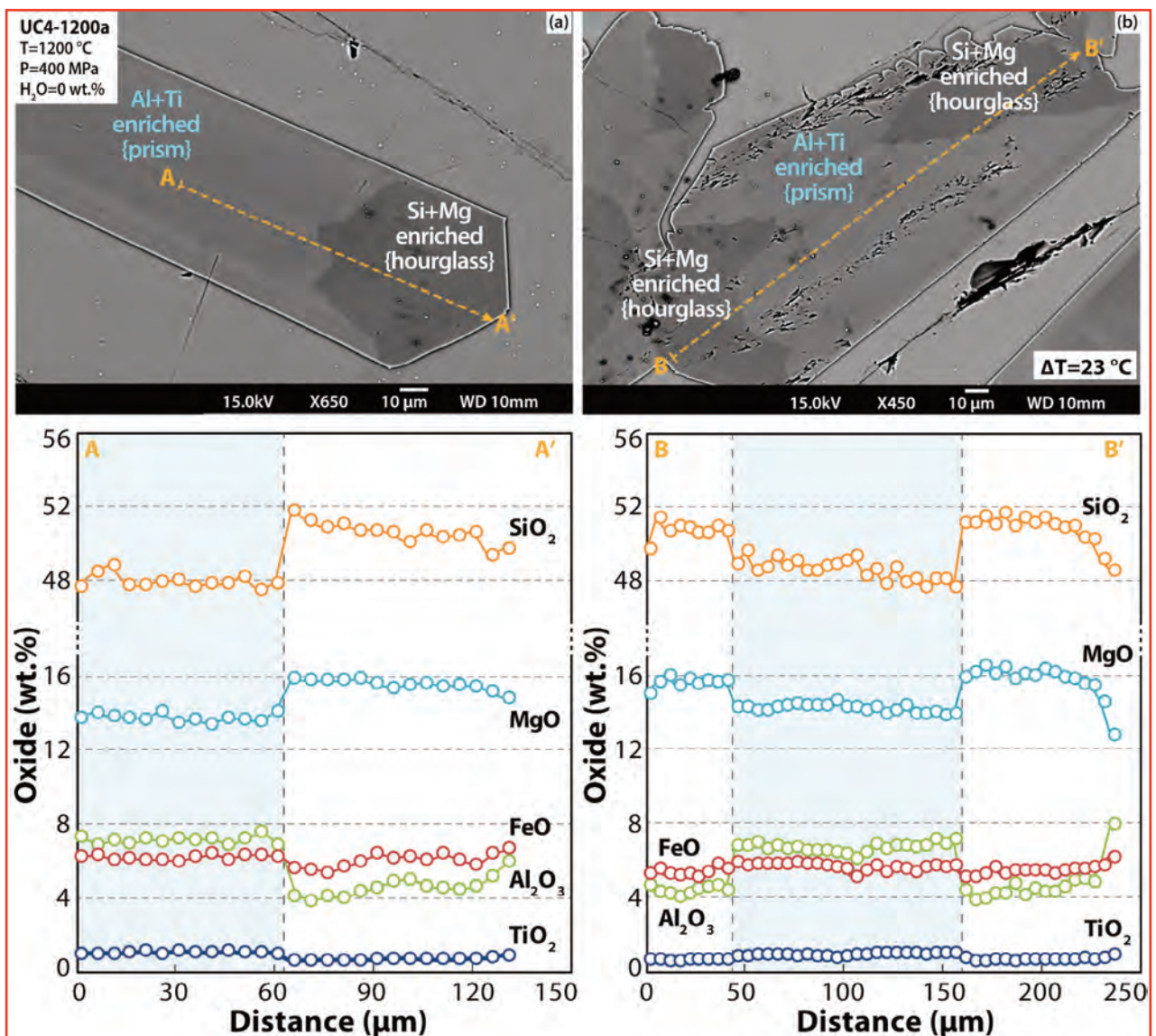


Fig. 1 | BSE images (top) and compositional profiles (bottom) of euhedral, hourglass sector-zoned clinopyroxene crystals from undercooling experiments conducted at $\Delta T = 23^\circ\text{C}$.

A New Plagioclase-Liquid Hygrometer Specific to Trachytic Systems

Masotta M., Mollo S.

We present a new empirical plagioclase-liquid hygrometer for estimating the amount of H_2O dissolved in trachytic magmas. The hygrometer is based on the exchange reaction of anorthite between plagioclase and liquid, and is calibrated using crystallization experiments where the concentration of H_2O in quenched glasses has been accurately determined based on Fourier Transform Infrared Spectroscopy (FTIR) analysis. The multiple linear regression of plagioclase-liquid cation fractions and components from experimental data obtained at 150-202 MPa, 850-1020 °C, 1.17-7.57 wt. % H_2O and $\Delta NNO + 2.5$ buffer, yields to a highly accurate model with uncertainty of only ± 0.29 wt. % H_2O . The model reliability has been demonstrated using an independent test data set consisting of crystallization experiments from the literature and thermodynamically derived compositions. The fairly good convergence between our model calibration and the test data set excludes systematic H_2O overestimates or underestimates caused by miscalibration and data overfitting. The plagioclase-liquid hygrometer from this study has been applied to trachyandesitic (latitic) and trachytic products erupted over the last 1000 years at the La Fossa cone of Vulcano Island (Aeolian Islands, South-

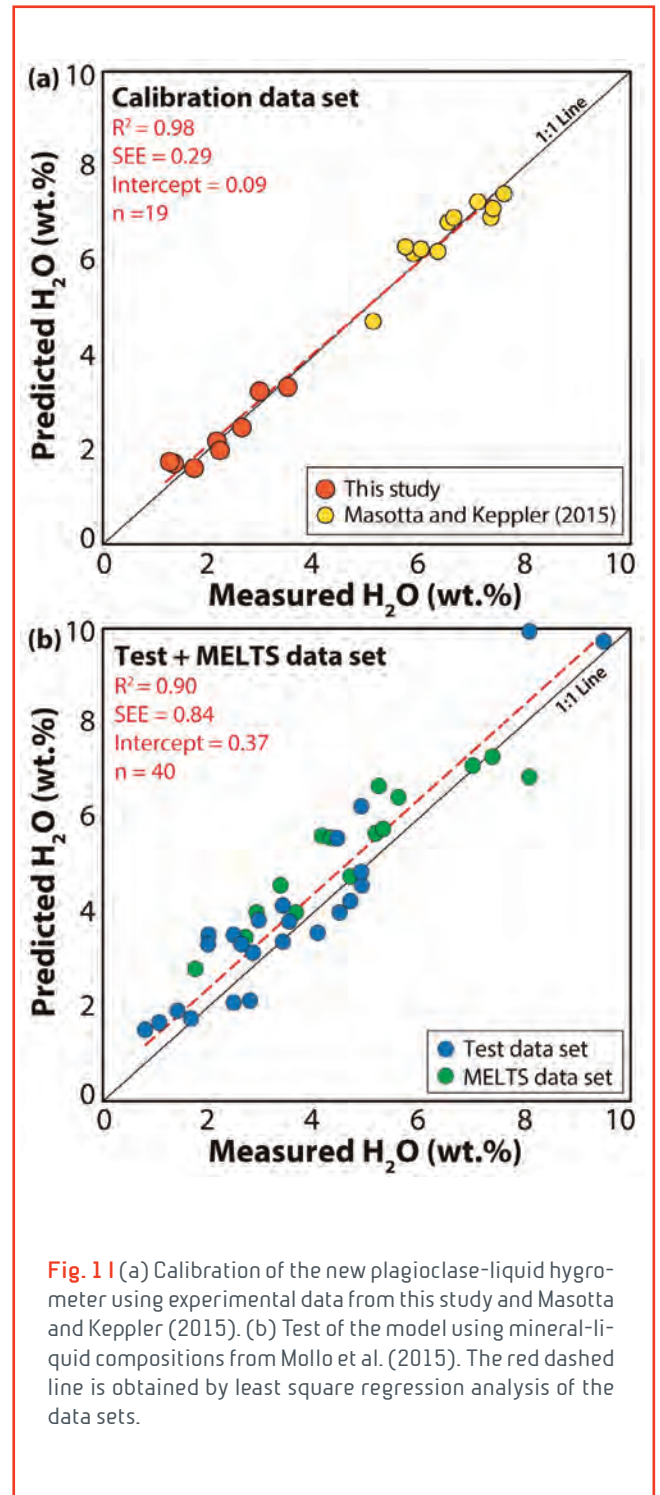
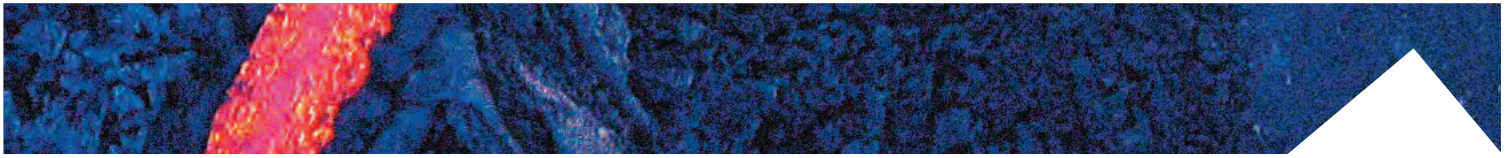
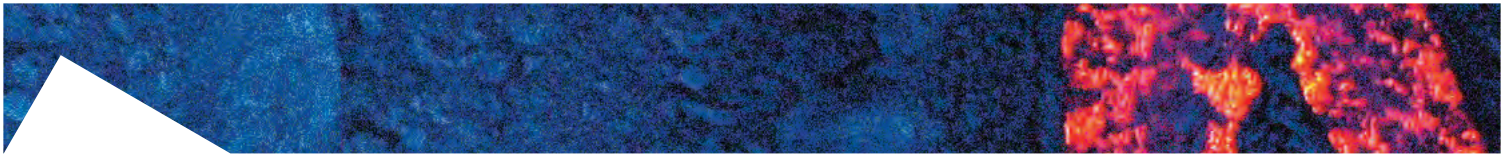


Fig. 1 (a) Calibration of the new plagioclase-liquid hygrometer using experimental data from this study and Masotta and Keppler (2015). (b) Test of the model using mineral-liquid compositions from Mollo et al. (2015). The red dashed line is obtained by least square regression analysis of the data sets.



ern Italy). Results from calculations indicate that the concentration of H₂O in the latitic and trachytic melts is comprised between ~2.5 and ~3.5 wt. %. These values are in good agreement with data from melt inclusions and, overall, testify to low-pressure, open-system differentiation of trachytic magmas under strong degassing conditions (Figure 1).



Reconstruction of the intensive variables and magmatic architecture of Vulcano island (Aeolian Arc, Italy)

Palummo F., Mollo S., De Astis G., Di Stefano F., Nazzari M., Scarlato P.

In this study, we present new mineralogical and petrological data on olivine, clinopyroxene, plagioclase and titanomagnetite phenocrysts from sixteen eruptive products (i.e., lava flows and pyroclastic deposits) collected at Vulcano island (Aeolian Arc, Italy) and representative of a relatively wide time period, from Epoch 5 (70-42 ka) to Epoch 8 (< 8

ka). These rocks show shoshonitic (SHO) to high-K calc-alkaline (HKCA) affinity, with compositions evolving from basalt ($Mg^{\#}_{60-57}$) to basaltic trachyandesite ($Mg^{\#}_{41-35}$) to trachyandesite ($Mg^{\#}_{32-54}$) to trachyte ($Mg^{\#}_{30-40}$) to rhyolite ($Mg^{\#}_{23-28}$). The intensive variables driving the crystallization of magma were reconstructed by employing mineral-melt equilibrium and thermodynamic models, as well as barometers, thermometers, hygrometers and oxygen barometers.

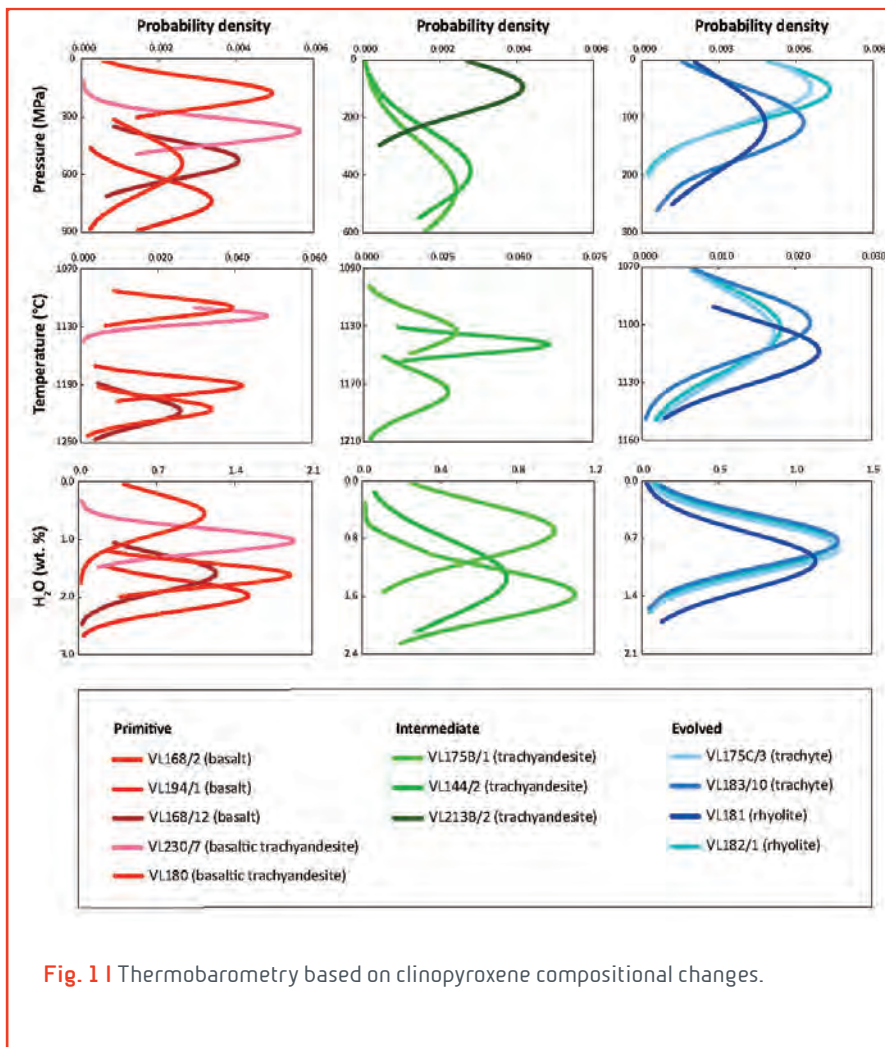
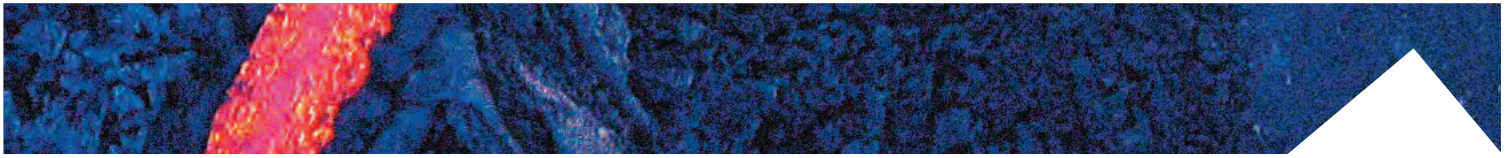
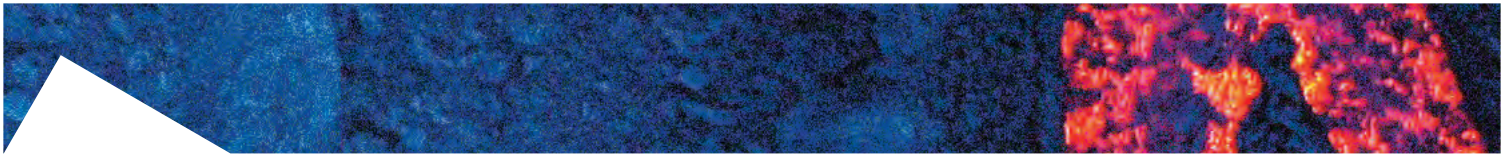


Fig. 1 | Thermobarometry based on clinopyroxene compositional changes.

The stability of olivine (Fo_{61-91}), as first phase on liquidus, is restricted to 100-300 MPa and 1080-1180°C. Afterwards, the melt is co-saturated with clinopyroxene ($Mg^{\#}_{92}$, diopside), which composition progressively evolves ($Mg^{\#}_{64}$, augite) as the temperature decreases to 1090 °C. The jadeite exchange between clinopyroxene and melt indicates



that the overall decompression path of magmas ranges from 900 to 0.1 MPa. The maximum crystallization pressure decreases from basalt/basaltic trachyandesite (900 MPa) to trachyandesite (650 MPa) to trachyte/rhyolite (250 MPa). The melt-water content (0.5-6.5 wt.%) is sensitive to either pressure or melt composition, thus controlling the plagioclase stability and chemistry (An_{30-80}). Titanomagnetite (Usp_{11-29}) equilibrates with progressively more evolved and oxidized melts, from $\Delta QFM+1.5$ to $\Delta QFM+3$. We conclude that the architecture of the plumbing system at Vulcano island is characterized by multiple reservoirs in which compositionally distinct magmas stall and undergo polybaric-polythermal differentiation, before eruption to the surface (Figure 1).



Mush cannibalism and disruption recorded by clinopyroxene phenocrysts at Stromboli volcano: new insights from recent 2003-2017 activity

Di Stefano F., Mollo S., Ubide T., Petrone C.M., Caulfield J., Scarlato P., Nazzari M., Andronico D., Del Bello E.

The Present-day activity of Stromboli (Aeolian Islands, Southern Italy) is periodically interrupted by lava flows and more violent explosions (so-called paroxysms). The Strombolian activity is persistently fed by a vertically-extended mush column with an open-conduit configuration. Equilibrium between the volume of injected and erupted magma in the volcano plumbing system leads to a steady-state regime, ensuring bulk compositional uniformity of eruptive products through time via periodic supply of deep, hot, mafic magma (low porphyritic or lp-magma) into a homogeneous shallow reservoir (highly porphyritic or hp-magma). The compositional zoning in clinopyroxene provides es-

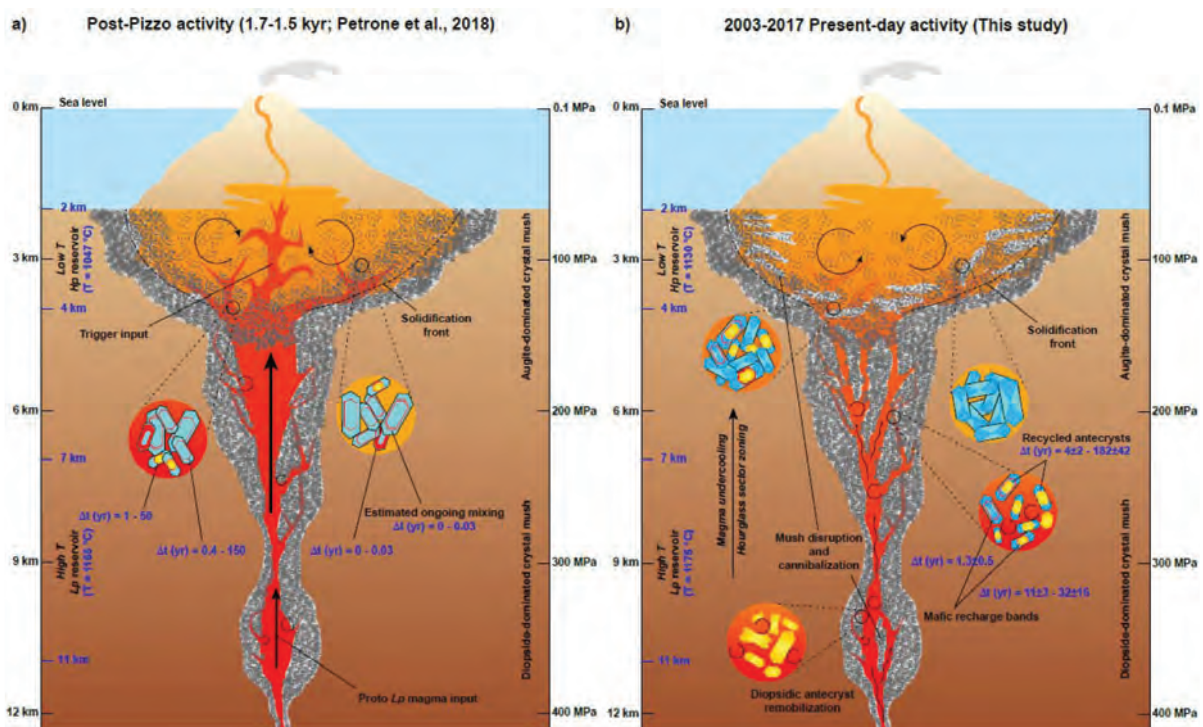
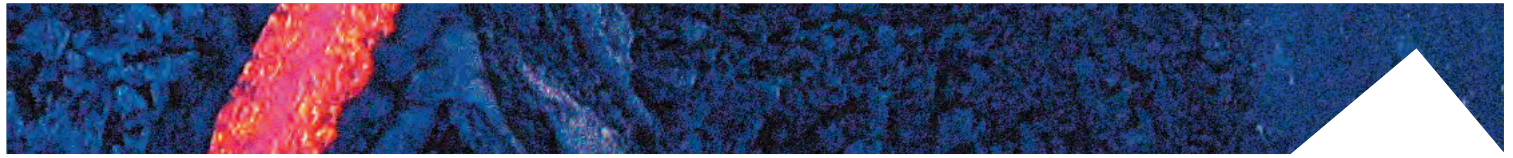
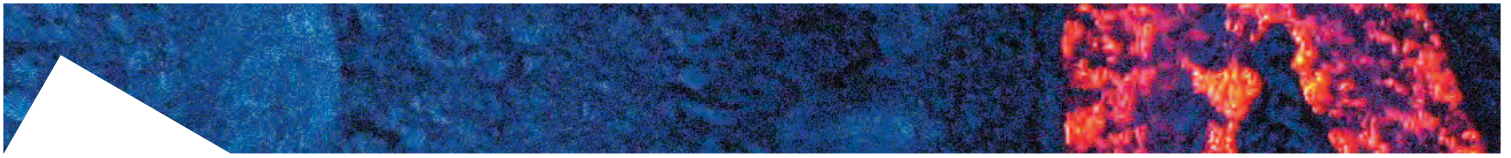


Fig. 1 | Working model for the extended plumbing system at Stromboli volcano during the a) Post-Pizzo period and the b) Present-day 2003-2017 activity. During the Post-Pizzo period, the abundant occurrence of diopside bands is directly related to quasi-instantaneous timescales caused by rapid and voluminous injections of fresh Lp-magmas triggering the eruption. This means that mafic Lp-magmas do not stall within the crystal mush over prolonged time periods, and no antecrysts are transported into the shallow Hp-reservoir. We propose that the 2003-2017 activity represents a new phase in the lifetime of Stromboli volcano, characterized by more efficient mechanisms of mush disruption and cannibalization, in which the old diopside antecrysts were continuously remobilized and transported by the Lp-magmas permeating the mush.



sential information on pre-eruptive magma dynamics, indicating multi-stage crystallization across the lp-hp-reservoirs, where diopsidic compositions are markers of more primitive, higher-T magmas injecting into shallow, lower-T domains of the plumbing system. Phenocrysts from the 2003-2017 activity show very mild sector zoning, interpreted in the context of crystal convection at reservoir margins. Diopsidic bands record lp-recharges injected into the shallow hp-reservoir. Resorbed diopsidic cores (antecrysts) testify to the continuous disruption and cannibalization of relic crystal mushes at different depths. Very short timescales (1 year) are estimated for the diopsidic bands from the 2003 paroxysm, documenting restricted temporal intervals between mafic injection, magma mixing and homogenization in the hp-reservoir and subsequent eruption. Longer timescales (11-32 years) are obtained for diopsidic recharge bands surrounding resorbed (diopsidic) antecrysts and for the diopsidic cores (4-182 years). We conclude that a distinct phase in the life of Stromboli volcano commenced at least after the violent 2003 paroxysm. Our observations suggest there are more efficient mechanisms of mush disruption and cannibalization, in which old diopsidic antecrysts are continuously remobilized and transported by the lp-magmas permeating the mush. The disappearance of diopsidic recharge bands within augitic overgrowths indicates that over time, magmatic injections feeding the persistent Present-day activity are more intensively mixed and homogenized prior to eruption, reflecting small recharge volumes and/or a more mafic system in which the mafic inputs are less evident (Figure 1).



Interpreting magma dynamics through a statistically refined thermometer: Implications for clinopyroxene Fe-Mg diffusion modeling and sector zoning at Stromboli

Mollo S., Blundy J., Scarlato P., De Cristofaro S.P., Tecchiato V., Di Stefano F., Vetere F., Holtz F., Bachmann O.

Relying on its broad mineral stability field, extending from mantle depths to shallow crustal levels, clinopyroxene is a typical phase of volcanic eruptions and is frequently used for modeling the intensive variables of active volcanic settings. Clinopyroxene-based thermometers are calibrated using a great number of clinopyroxene and/or melt components, resulting in a variety of clinopyroxene-melt, clinopyroxene-only and melt-only models with calibration errors in the range 18-58 °C. If the uncertainty of a thermometer is higher than the temperature changes associated with

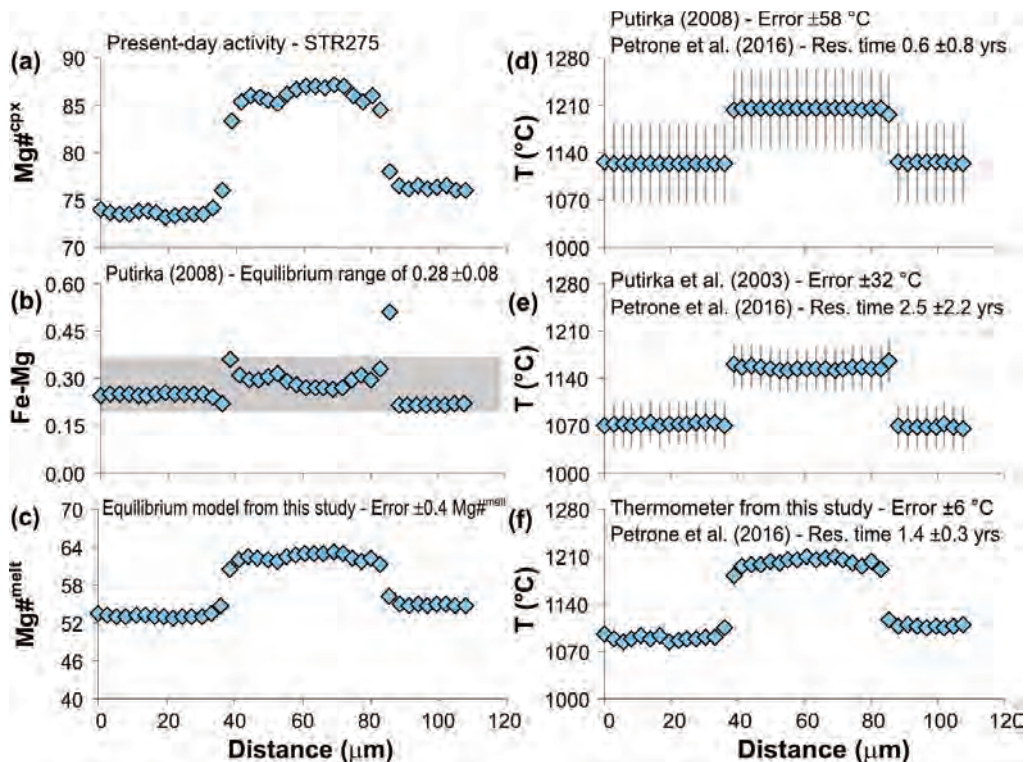
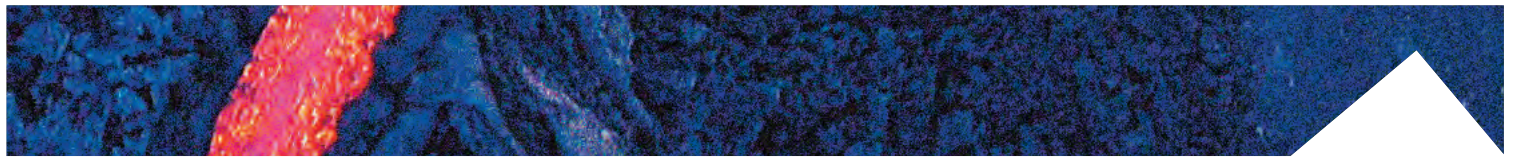
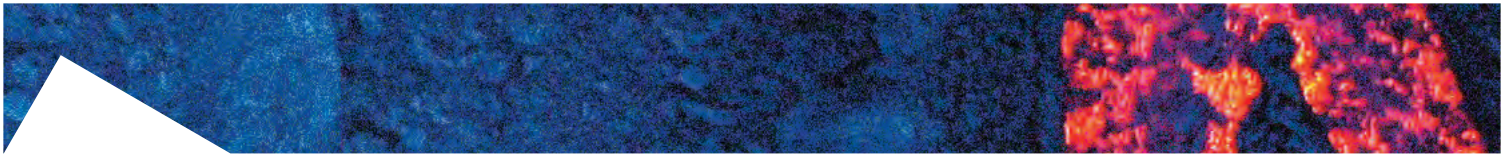


Fig. 1 | Mg#_{cpx} data from Active Craters and Early Paroxysm (EP) activity (sample STR275) (a). Fe-Mg exchange between clinopyroxene compositions and the mafic bulk rock of Ip magma and the more differentiated matrix glass analysis (b). Mg#_{melt} obtained by applying the equilibrium model from this study and using as input data the composition of clinopyroxene (c). Application of the clinopyroxene-only thermometer (d), the clinopyroxene-melt thermometer (e), and the thermometer from this study specific to Stromboli magmas (f). The Non-Isothermal Diffusion Incremental Step (NIDIS) model of Petrone et al. (2016) is employed to estimate crystal residence times using as input data the temperatures predicted by each different thermometer.



complex magma dynamics, any attempt to correctly assess the clinopyroxene zoning is not a trivial task. Here we present a more accurate clinopyroxene-only thermometer for shoshonite melts, successfully calibrated relying on a solid statistical analysis of both experimental and thermodynamically-derived compositions. The calibration data set refers to the compositions of magmas at Stromboli, one of the most studied volcanoes in Italy and of broad significance as the type locality for Strombolian activity. Through test compositions not included in the calibration data set, we verify that the predictive power of the clinopyroxene-only thermometer is potentially very high, with an uncertainty of only 6 °C for crystallization conditions of 10-900 MPa, 1.000-1.200°C, 1-5 wt.% H₂O, and -1.66-1.27 NNO. For compositions extremely different from those of Stromboli magmas (i.e., trachytic and phonolitic melts), the error of estimate may increase up to 30°C but is still a relatively low uncertainty with respect to other thermometers from literature. The strong linear correlation between T and Mg#_{melt} allows to test for equilibrium between natural clinopyroxene compositions and their host magmas, supporting the use of the clinopyroxene-only thermometer with alkaline eruptive products to minimize the error of temperature estimate. We illustrate the potential of this integrated approach by modeling temperature changes for clinopyroxene compositional zoning caused by recharge episodes of mafic magmas at Stromboli. With respect to previous thermometric equations, the percentage error on diffusion timescales decreases from 51% to 21%. Owing to its high accuracy, the thermometer is also suitable to estimate the crystallization temperature of hourglass sector-zoned clinopyroxenes where kinetic effects induce differential elemental partitioning into {100} and {-111} sectors.



Modeling the crystallization and emplacement conditions of a basaltic trachyandesitic sill at Mt. Etna Volcano

Nazzari M., Di Stefano F., Mollo S., Scarlato P., Tecchiato V., Ellis B., Bachmann O., Ferlito C.

This study documents the compositional variations of phenocrysts from a basaltic trachyandesitic sill emplaced in the Valle del Bove at Mt. Etna volcano (Sicily, Italy). The physicochemical conditions driving the crystallization and emplacement of the sill magma have been reconstructed by barometers, oxygen barometers, thermometers and hygrometers based on clinopyroxene, feldspar (plagioclase + K-feldspar) and titanomagnetite. Clinopyroxene is the liquidus phase, recording decompression and cooling paths decreasing from 200 to 0.1 MPa and from 1050 to 940°C, respectively. Plagioclase and K-feldspar co-saturate the melt in a lower temperature interval of 1000–870 °C. Cation exchanges in clinopyroxene (Mg-Fe) and feldspar

(Ca-Na) indicate that magma ascent is accompanied by progressive H₂O exsolution (up to ~2.2 wt. %) under more oxidizing conditions (up to NNO + 0.5). Geospeedometric constraints provided by Ti-Al-Mg cation redistributions in titanomagnetite indicate that the travel time (up to 23 h) and ascent velocity of magma (up to 0.78 m/s) are consistent with those inferred for other eruptions at Mt. Etna. These kinetic effects are ascribed to a degassing-induced undercooling path caused principally by H₂O loss at shallow crustal conditions. Rare earth el-

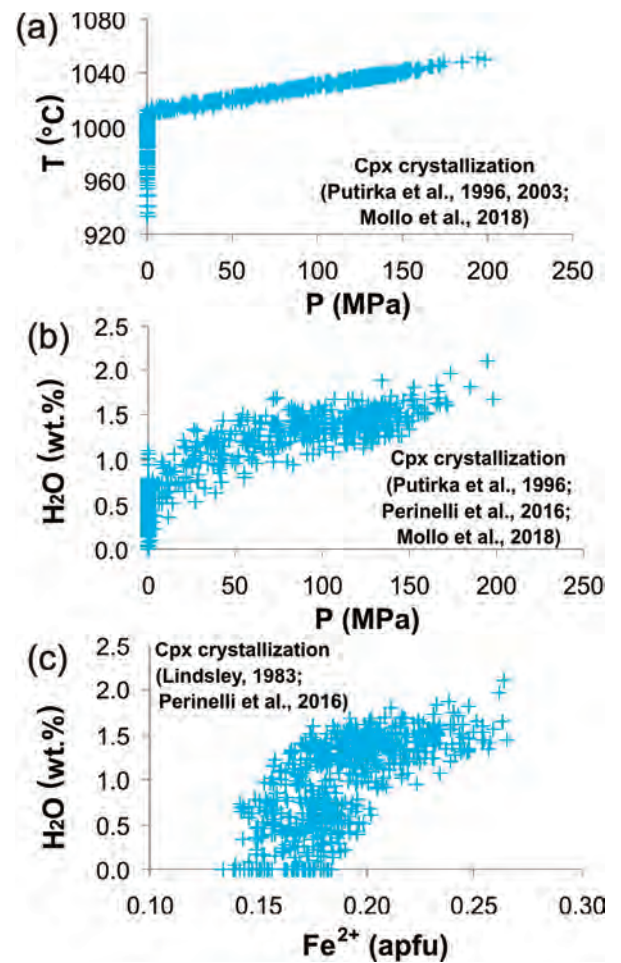
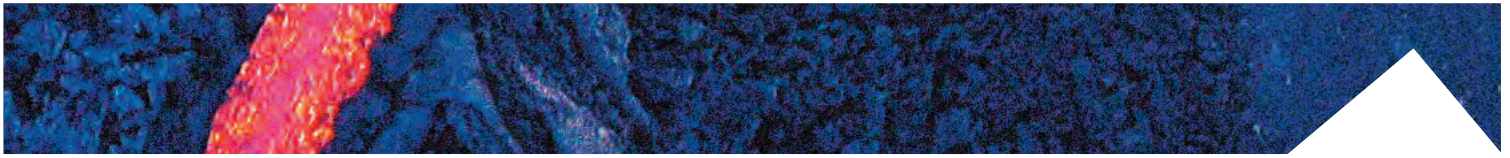
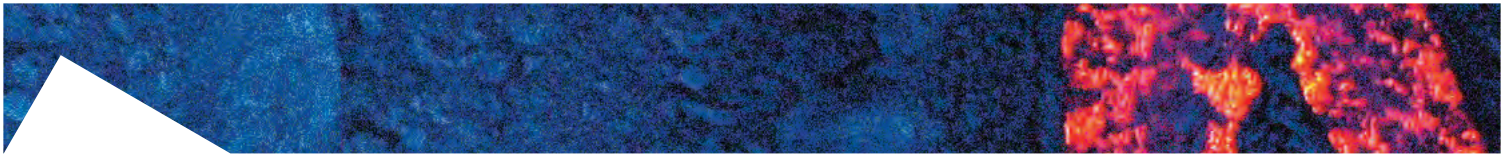


Fig. 1 | Temperatures (a), pressures (a and b) and melt-H₂O contents (b and c) in equilibrium with clinopyroxene phenocrysts.



ement (REE) modeling based on the lattice strain theory supports the hypothesis that the sill magma formed from primitive basaltic compositions after clinopyroxene (41%) and plagioclase (12%) fractionation. Early formation of clinopyroxene at depth is the main controlling factor for the REE signature, whereas subsequent degassing at low pressure conditions enlarges the stability field of plagioclase causing trace element enrichments during eruption towards the surface.



Kinetic aspects of major and trace element partitioning between olivine and melt during solidification of terrestrial basaltic materials

Lang S., Mollo S., France L., Nazzari M., Misiti V.

The incorporation of trace elements within the crystal lattice of igneous minerals is mostly controlled by the pressure, temperature and bulk composition of the system. This research focuses on the partitioning of major and trace elements between olivine and melt, by considering the substitution mechanisms affecting these substitution reactions. To suc-

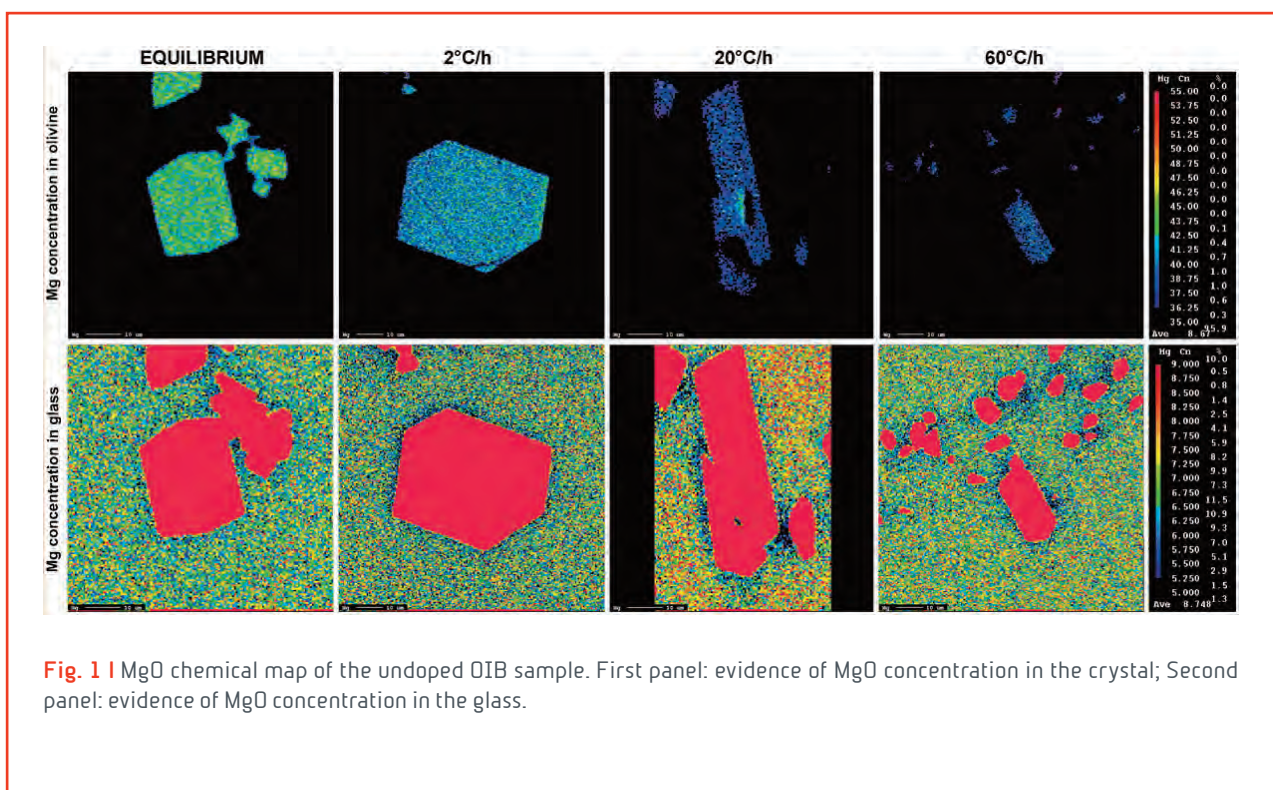
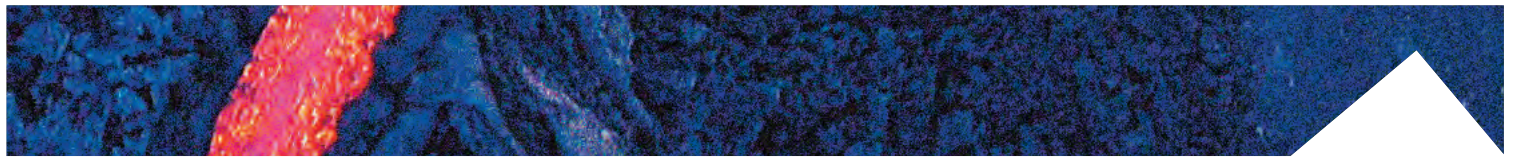
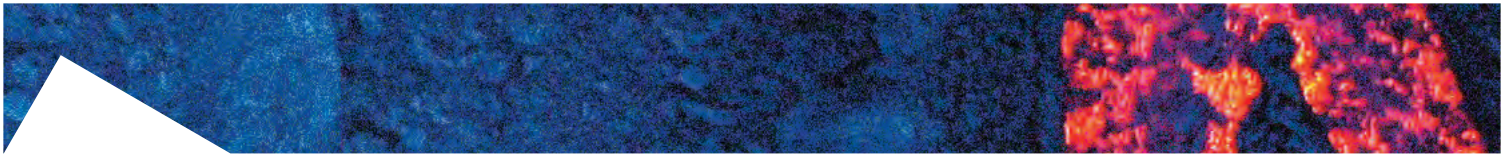


Fig. 1 | MgO chemical map of the undoped OIB sample. First panel: evidence of MgO concentration in the crystal; Second panel: evidence of MgO concentration in the glass.

cessfully address this issue, we are investigating in laboratory the partitioning of major and trace elements in two different basalts: a Hawaiian Oceanic Island Basalt (OIB) and an Indian Mid-Oceanic Ridge Basalt (MORB). This is done by varying the intensive and extensive variables of the system, such as the pressure, temperature, oxygen fugacity and composition (by including also volatile contents). We are also considering the effect of undercooling and cooling rates to provide evidence of core-to-rim crystal zoning and the presence of a diffusive boundary layer in the melt next to the crystal interface, as well as to calibrate geospeedometric models to constrain the crustal transport of OIB and MORB magmas. The disequilibrium experiments show a decreasing of the MgO amount in the crystal composition



with increasing cooling rate. The diffusion boundary layer next to the crystal rim become most important with a high cooling rate than at equilibrium, especially for the major element. The evolution of the magnesium composition is compatible with the chemical maps, thereby the amount of MgO in the crystal and the melt decreases with increasing cooling rate. The velocity of the crystal growth also increases, but magnesium remains strongly compatible with olivine. The diffusion boundary layer in the melt becomes depleted in magnesium, as the diffusion of Mg is lower than the crystal growth velocity. This explains the decrease of MgO in olivine and the decreasing partitioning of magnesium at the crystal-melt interface. Calcium and aluminum have a similar behavior, their amount in olivine increases under kinetic effects and, in contrast, it decreases in the melt. As the crystal growth velocity increases, incompatible cations are preferentially incorporated in the crystal lattice of olivine.



The effect of CaO on the partitioning behavior of REE, Y and Sc between olivine and melt: Implications for basalt-carbonate interaction processes

Di Stefano F., Mollo S., Blundy J., Scarlato P., Nazzari M., Bachmann O.

The partitioning of REE, Y and Sc (R^{3+}) between olivine and melt has been investigated experimentally during basalt-carbonate interaction. Three synthetic basalts ($^{melt}Mg\#_{72}$, $^{melt}Mg\#_{75}$ and $^{melt}Mg\#_{78}$) were doped with 0, 10 and 20 wt.% $CaCO_3$ and then equilibrated for 72 h at 1 atm, 1150, 1200 and 1250 °C, and the QFM oxygen buffer. The thermal decomposition of $CaCO_3$ produced CaO contents in the melt up to ~22 wt.%. Regular relationships are found between the ionic radius and the partition coefficient ($D_{R^{3+}}$), showing typical near-parabolic patterns. $D_{R^{3+}}$ is weakly dependent

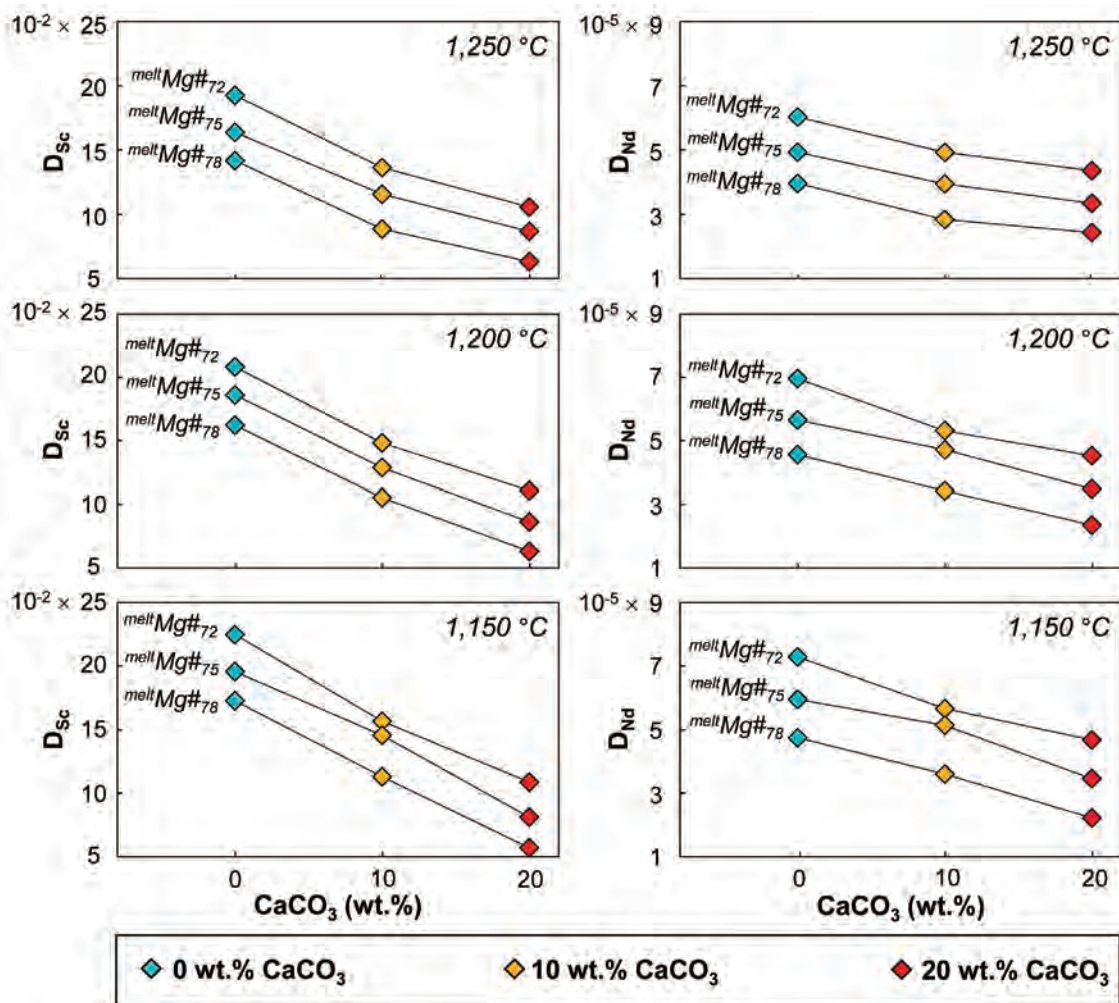
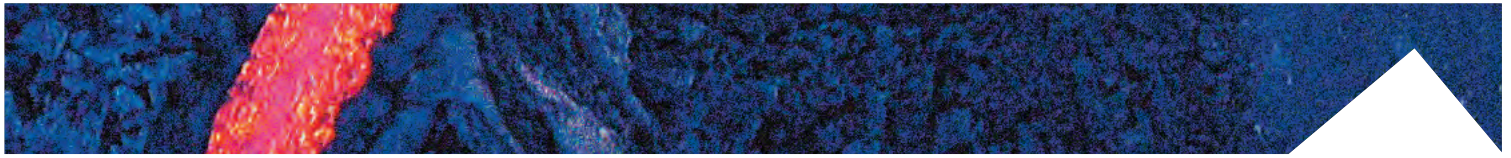


Fig. 1 | Variations of Sc and Nd partition coefficients as a function of T, meltMg# and $CaCO_3$.



on temperature, but decreases with increasing CaCO_3 in the starting material (e.g., D_{Sc} decreases from 0.20 to 0.13). From the point of view of the lattice strain theory, is described in terms of the radius of the crystal site (r_0), the Young Modulus (E) due to the elastic response of that site to lattice strain caused by cation insertion, and the strain-free partition coefficient (D_0). The value of r_0 decreases as Ca cations are accommodated into the more distorted M2 site of olivine via progressive Ca-Fe substitutions. This mechanism is accompanied by a higher proportion of Mg cations entering into the smaller M1 site, making the optimum ionic radius smaller and favoring the crystallization of more forsteritic olivines from decarbonated melts. The enrichment of Ca in the crystal lattice is also proportional to the number of Si and Ca cations available in the melt. This causes E to be anticorrelated either with Ca in olivine or the activity of Ca_0 in the melt. R^{3+} cations behave as network modifiers and, during basalt-carbonate interaction, the increasing abundance of non-bridging oxygens enhances the solubility of REE, Y and Sc in the melt. As a consequence, D_0 is negatively correlated with the degree of melt depolymerization. Additionally, the strain of the crystal lattice dominates the DR^{3+} parabolic patterns and D_0 is strongly controlled by forsterite and aluminium concentrations in olivine. The accommodation of REE, Y and Sc in the crystal lattice requires maintenance of local charge-balance by the generation of vacancies, in accord with a paired substitution of R^{3+} and a vacancy for Mg in octahedral sites.

Deep magma storage revealed by multi-method elemental mapping of clinopyroxene megacrysts at Stromboli Volcano

Ubide T., Caulfield J., Brandt C., Bussweiler Y., Mollo S., Di Stefano F., Nazzari M., Scarlato P.

The magmatic architecture and physicochemical processes inside volcanoes influence the style and timescale of eruptions. A long-standing challenge in volcanology is to establish the rates and depths of magma storage and the events that trigger eruption. Magma feeder systems are remarkably crystal-rich, and the growth stratigraphy of minerals

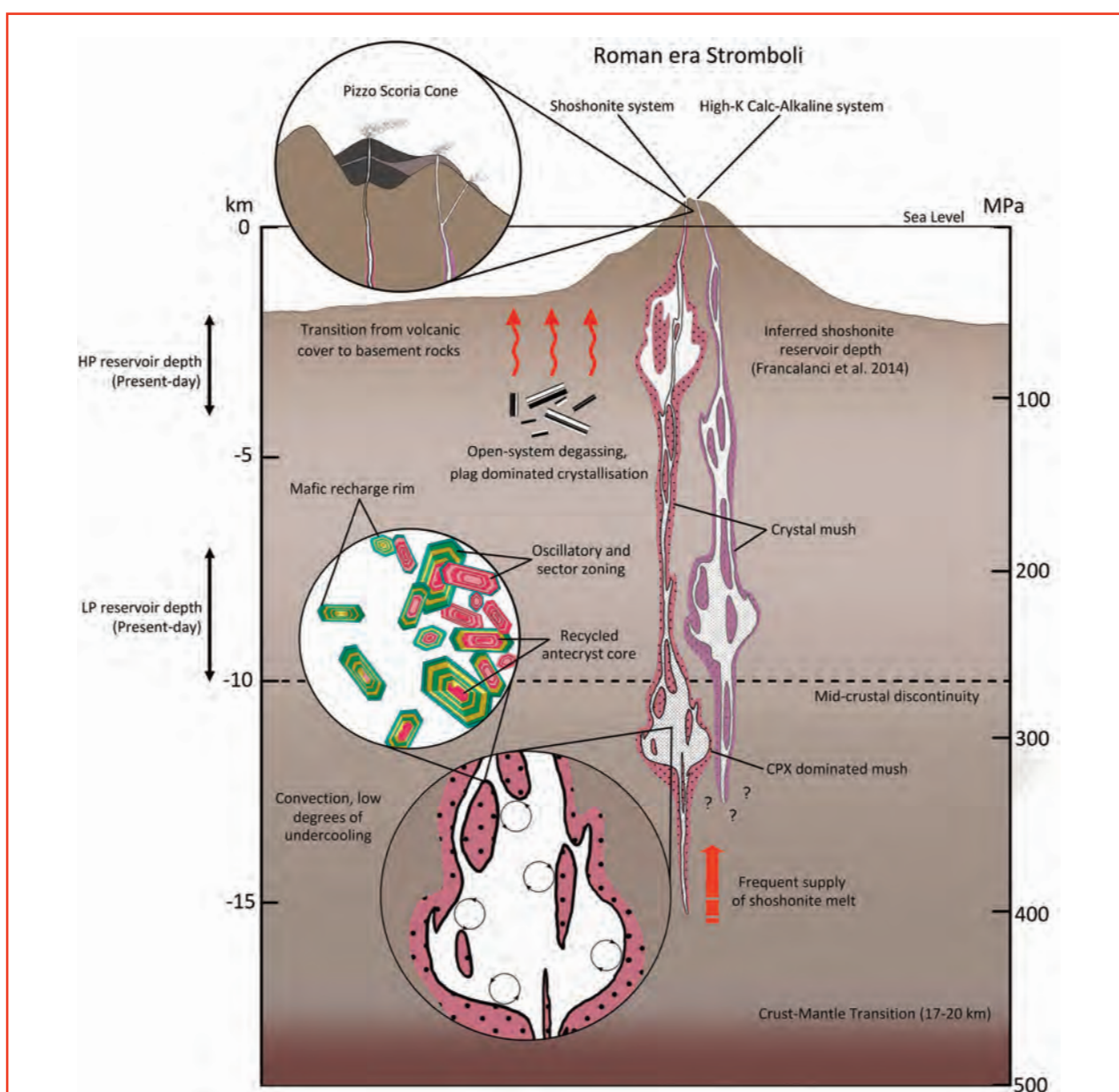
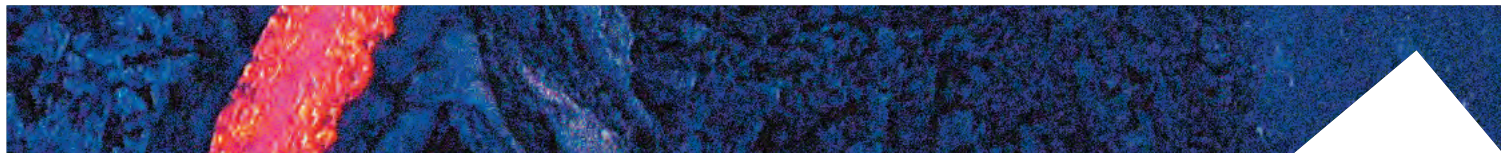
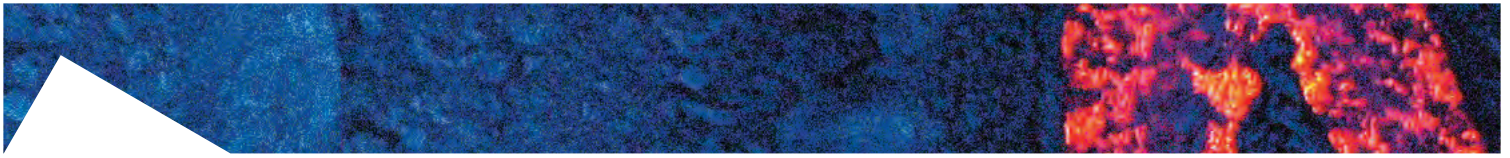


Fig. 1 | Working model for the extended plumbing system at Stromboli volcano during Pizzo (Roman) times.



sampled by erupted magmas can reveal a wealth of information on pre-eruptive processes. Here we combine detailed textural and chemical data acquired on large, euhedral augite megacrysts from Roman era activity (Pizzo scoria cone, 2.4–1.8 ka) at Stromboli (Italy) to investigate the plumbing system prior to the onset of current steady-state activity. Our dataset includes novel laser ablation time-of-flight mass spectrometry maps, which rapidly visualize multi-element zoning patterns across entire megacryst sections. The clinopyroxene data are complemented with geochemical constraints on mineral and melt inclusions, and adhering glassy tephra. Megacrysts are sector and oscillatory zoned in trace elements, yet their major element compositions are relatively uniform and in equilibrium with shoshonite-buffered melts. Mild sector zoning documents dynamic crystallisation under conditions of low undercooling during magma residence and growth. Clinopyroxene-melt thermobarometric and hygrometric calibrations, integrated with thermodynamically derived equilibrium equations, accurately track the crystallisation path of magmas. The refined models return restricted crystallization depths that are deeper than those reported previously for historical and current eruptions, but consistent with deep clinopyroxene-dominated crystallisation (≥ 10 km), resembling other water-rich alkaline mafic systems. Megacryst cores are overgrown by oscillatory zoned mantles recording continuous input of magma that failed to trigger eruption. Crystal rims are characterized by a mild increase in compatible transition metals Cr and Ni, and depletion in incompatible elements, indicative of pre-eruptive mafic replenishment and magma mixing. The volcanic system appears to have been dominated by protracted periods of replenishment, convection, and crystal residence, punctuated by rapid megacryst evacuation and eruption upon arrival of more mafic magma (days-weeks).



Sector-zoned clinopyroxene as a recorder of magma history, eruption triggers, and ascent rates

Ubide T., Mollo S., Zhao J.X., Nazzari M., Scarlato P.

Sector-zoned clinopyroxene is common in igneous rocks, but has been overlooked in the study of magmatic processes. Whilst concentric zoning is commonly used as a record of physicochemical changes in the melt feeding crystal growth, clinopyroxene is also highly sensitive to crystallisation kinetics. In sector-zoned crystals, the fidelity of compositional changes as recorders of magma history is dubious and the interplay between thermodynamic and kinetic controls remains poorly understood. Here we combine electron probe and laser ablation micro-chemical maps of titanite crystals from Mt. Etna (Sicily, Italy) to explore the origin of sector zoning at the major and trace element levels, and its implications for the interpretation of magmatic histories. Elemental maps afford the possibility to revisit sector zoning from a spatially controlled perspective. The most striking observation is a clear decoupling of elements into sectors vs. concentric zones within single crystals. Most notably, Al-Ti enrichments and Si-Mg depletions in the prism sectors $\{100\}$, $\{110\}$ and $\{010\}$ relative to the hourglass (or basal)

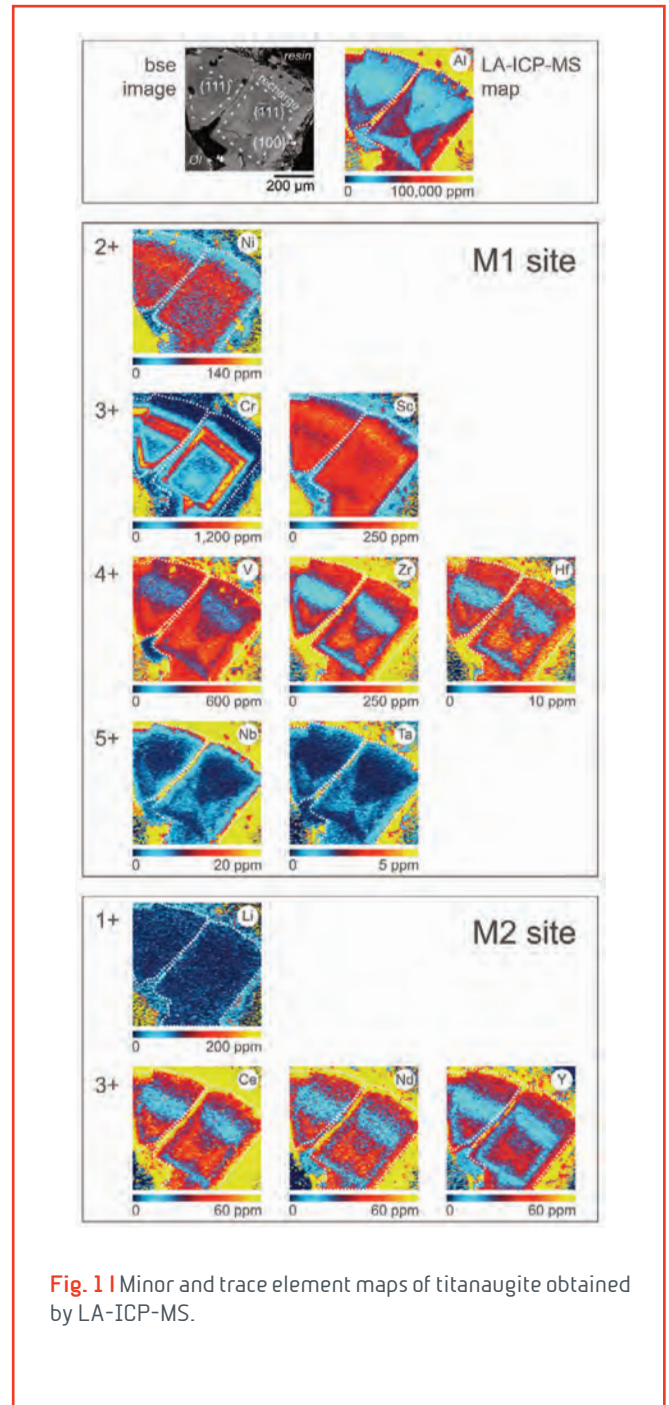
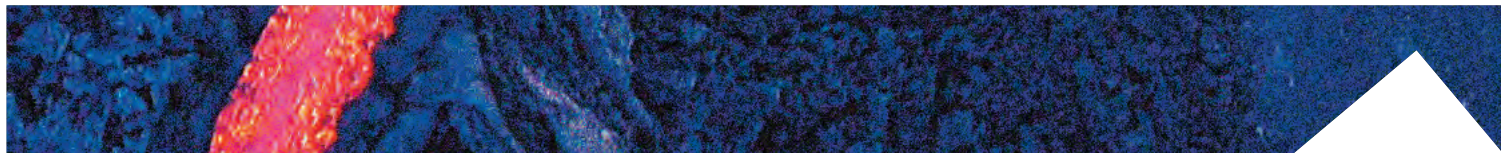
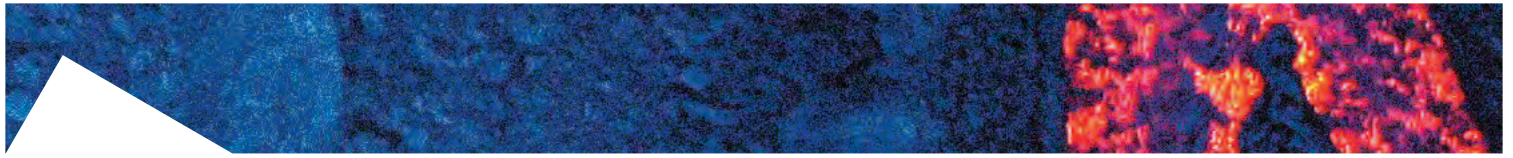


Fig. 1 | Minor and trace element maps of titanite obtained by LA-ICP-MS.

sectors $\{-111\}$ correlate with enrichments in rare earth elements and highly charged high field strength elements due to cation exchanges driven by kinetic effects. In contrast, transition metals (Cr, Ni, Sc) show little partitioning



into sectors and strong enrichments in concentric zones following resorbed surfaces, interpreted as evidence of mafic recharge and magma mixing. Our results document that kinetic partitioning has minor effects on the compositional variations of cations with low charge relative to the ideal charge/radius of the structural site they occupy in the clinopyroxene lattice. We suggest that this may be due to a lower efficiency in charge balance mechanisms compared to highly charged cations. It follows that compatible metals such as Cr can be considered trustworthy recorders of mafic intrusions and eruption triggers even in sector-zoned crystals. We also observe that in alkaline systems where clinopyroxene crystallisation takes place at near-equilibrium conditions, sector zoning should have little effect on Na-Ca partitioning and in turn, on the application of experimentally calibrated thermobarometers. Our data show that whilst non-sector-zoned crystals form under relatively stagnant conditions, sector zoning develops in response to low degrees of undercooling, such as during slow magma ascent. Thus, we propose that the chemistry of sector-zoned crystals can provide information on magma history, eruption triggers, and possibly ascent rates.



Compositionally zoned clinopyroxene crystals record fluctuations in the Agnano Monte Spina (Campi Flegrei, Italy) magma plumbing system

Pelullo C., Arienzo I., D'Antonio M., Nazzari M., Pappalardo L., Petrosino P.

In the framework of the Timescales of magmatic processes, a project involving a collaboration between the INGV (Istituto Nazionale di Geofisica e Vulcanologia) and the DiSTAR of the University of Naples Federico II, quantitative chemical analysis on clinopyroxene crystals from the Agnano Monte Spina (AMS) eruption (Campi Flegrei caldera, South Italy) were performed with the Jeol JXA 8200 SuperProbe Electron Probe MicroAnalyzer at the HPHT Laboratory of INGV, in Rome.

Zoning patterns preserve a record of magmatic processes over the lifetime of the crystal, from initial nucleation to final quenching upon eruption. Perturbations in magmatic variables (such as composition, volatile content, temperature, pressure, and oxidation state) can result in complex textural patterns of crystal growth and dissolution, with associated changes in crystal chemistry causing crystal zonation. Here a detailed characterization of the complex sequential zoning has been carried out on clinopyroxene crystals erupted during the 4690-4300 a cal BP AMS eruption, considered as reference event for a future large-scale explosive eruption at Campi Flegrei caldera. Particularly, we investigated the compositional record preserved in clinopyroxene crystals from selected sub-units of the AMS pyroclastic sequence. Detailed concentration profiles (20-600 μm long, spacing 2,5-10 μm ; Figure 1a) of major elements (Si, Ti, Al, Fe, Mg, Mn, Ca, Na) were measured along different directions in a total of 42 clinopyroxene crystals. The zoning patterns of Fe-Mg and selected elements (e.g. Al, Ti) often consist of two or more compositional plateau with both sharp and/or slightly diffuse boundaries between them (Figure 1b). The plateau composition is interpreted to represent growth of clinopyroxene under a constant set of intensive thermodynamic variables (pressure, temperature, composition, fugacity of volatile species), each characterizing a magmatic environment. A detailed systemization of the information stored in the sequential zoning reveals the existence of at least five magmatic environments (ME). These are characterized by different clinopyroxene composition (Figure 1c-d): M0 ($\text{Mg}^{\#}= 85-91$, number of crystals=26/41), M1 ($\text{Mg}^{\#}=80-84$, number of cry-

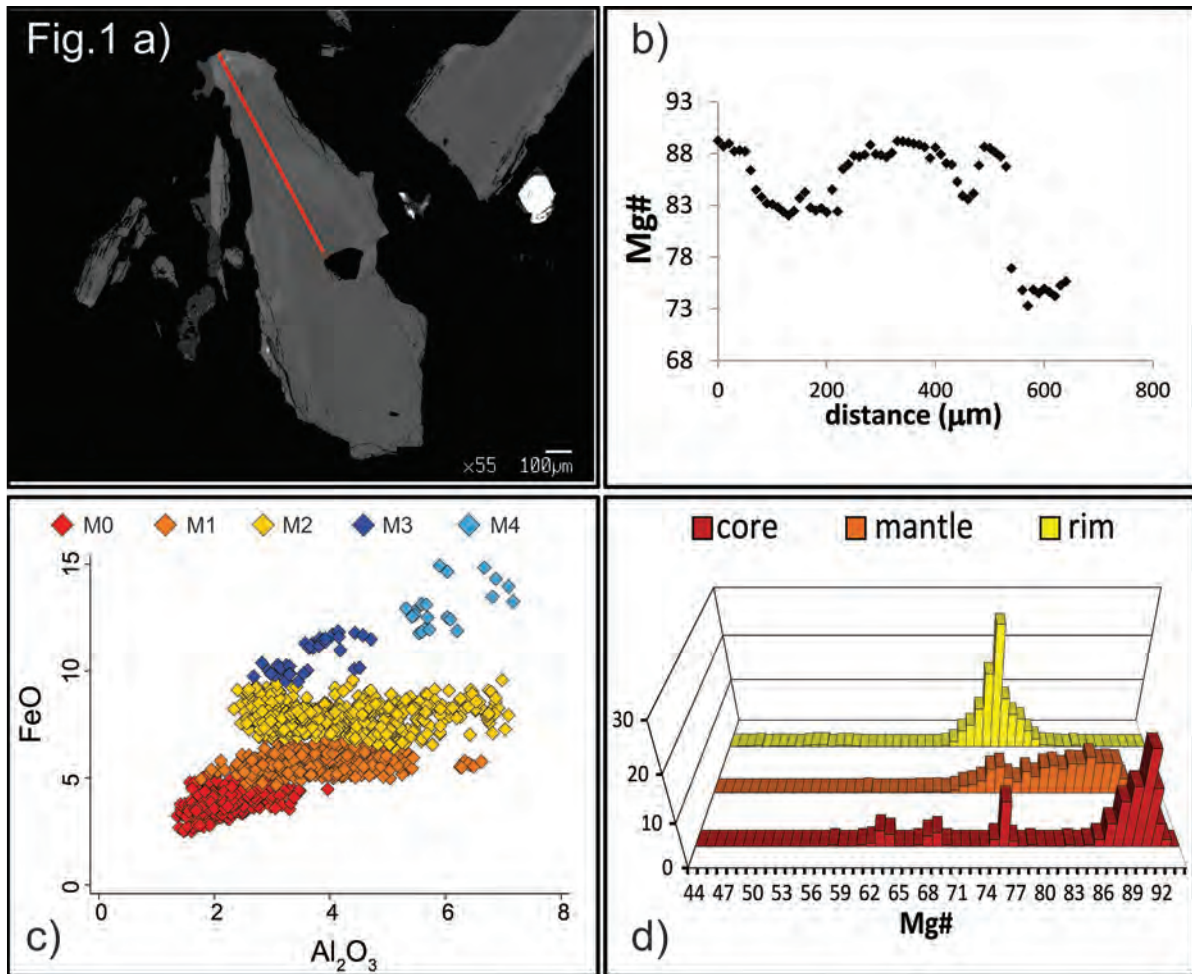
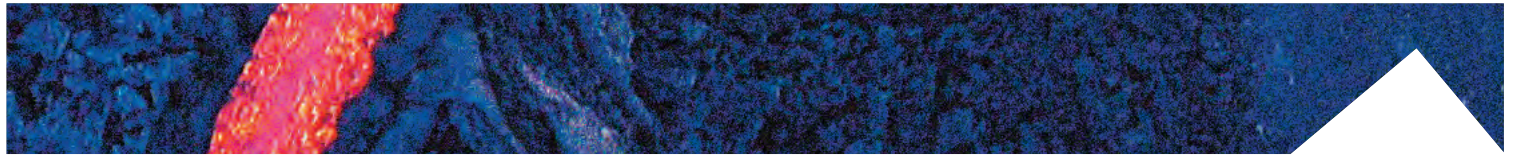
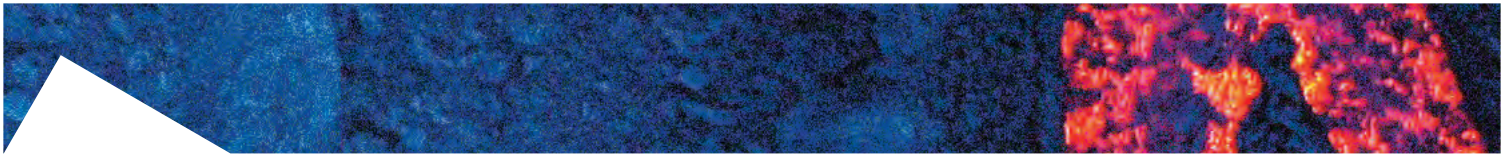
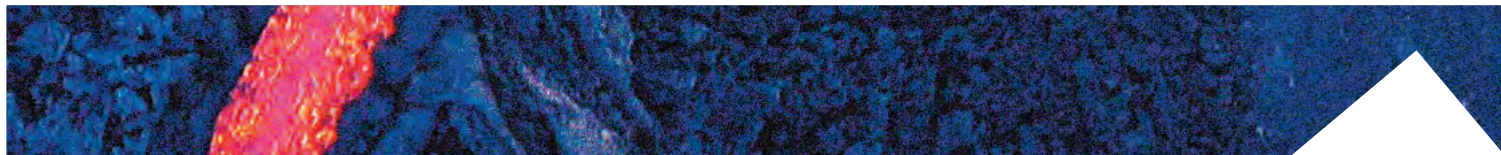


Fig. 1 a) BSE image of a clinopyroxene crystal from A-MS eruption; b) Mg# variation along the core to rim transect; c) Harker diagram showing the Al_2O_3 contents vs. FeO of the analysed samples; d) Mg# frequency histogram of the clinopyroxene crystal from A-MS eruption.

stals=12/41), M2 (Mg#=70-78, number of crystals=41/41), M3 (Mg#=60-69, number of crystals=3/42) and M4 (Mg# 46-59, number of crystals=1/42). The change in zoning pattern from one plateau composition to another is then equivalent to the transfer of the crystal from one ME to another. This can be accomplished either by the crystal physically moving (transported by melt) from one environment to another, or by the environment itself changing around the crystal (e.g. by cooling, heating or degassing, crustal assimilation etc). We identified main prominent crystal passageways between the environments M0:M2, several connection between M2:M0:M2, M1:M2, M0:M1:M2 and M2:M1:M2 and less abundant passageways between the environments M1:M0:M2, M2:M3:M2, M3:M2 and M2:M4. The large range of chemical compositions and the complexity of the variations recorded in the A-MS



clinopyroxenes suggest they experienced a complex growth before erupting, highlighting the intricate connection between deep and shallow magmatic reservoirs/layers beneath the Campi Flegrei caldera and the heterogeneity of the plumbing system of the A-MS eruption.



Primitive magmas and their crystalline cargoes as witnesses of the source to surface history of alkaline magmas in a complex intraplate polygenetic system: the Dunedin Volcano, New Zealand

Pontesilli A., Brenna M., Ubide T., Mollo S., Masotta M., Caufield J., Le Roux P., Nazzari M., Scarlato P.

Primitive alkaline magmas typically display a significant chemical variability, including magma compositions spanning from subalkaline basalts to basanites and nephelinites, representing extremes in terms of silica undersaturation and alkali enrichments. The large compositional range observed for the primitive spectrum of intraplate alkaline magmas has alternatively been attributed to different extent of asthenospheric/lithospheric mantle contributions and/or crustal contamination scenarios. On the other hand, the existence of different parental magmas has long been deemed responsible for the diversification of liquid line of descents leading to phonolites and trachytes, the typical alkaline evolved end-members, separated by a petrologic thermal boundary, and exhibiting a complex range in eruptive behaviors. Thus, a better understanding of early differentiation processes and storage conditions in continental intraplate alkaline volcanoes will not only have important petrologic implications but will also impact on hazard assessment considerations in these often widely populated volcanic areas. In this study we investigated, from a mineralogical and petrological point of view, basaltic magmas in the Dunedin Volcano (Otago region, southern New Zealand), representing the intraplate alkaline volcanic system in which the liquid line of descent leading to either trachyte or phonolite magma compositions were originally proposed. The observed compositional spectrum from subalkaline to alkaline basalts and trachyandesites is associated with systematic variations in whole rock major and trace elements and in isotopic compositions, displaying also a remarkable petrographic heterogeneity in the phenocryst cargo (Figure 1). More in detail, an increase in radiogenic Sr ($^{87}\text{Sr}/^{86}\text{Sr}$) in subalkaline lavas is shown to be inconsistent with crustal contamination, implying the presence of an EMII-like isotopic signature in the asthenospheric source, while the HIMU-like isotopic characteristics of most DV magmas are best accounted by derivation from a metasomatized lithospheric mantle, in agreement with previous studies on intraplate magmatism in the region. A detailed micro-chemical study of the crystalline cargo in DV basaltic products allowed reconstruction of

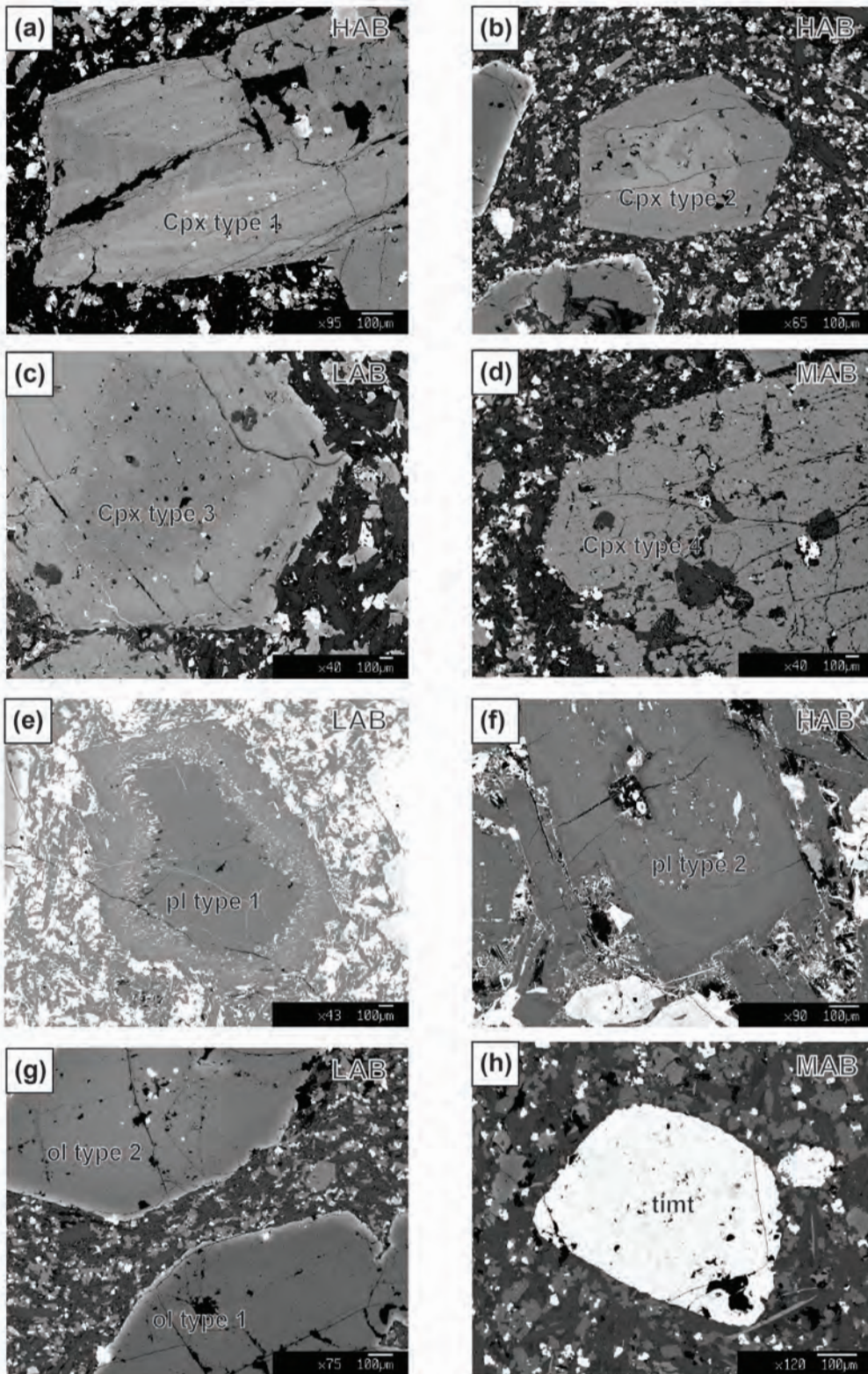
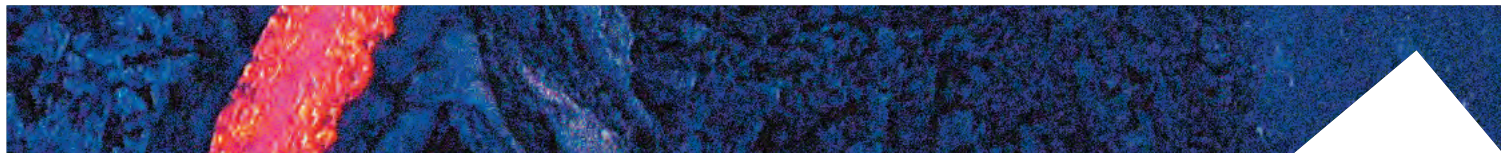
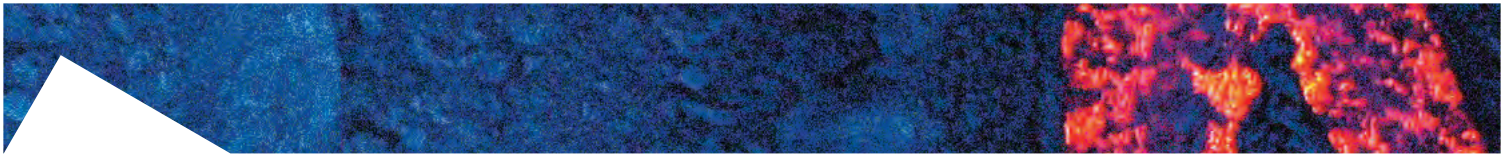


Fig. 1 | Main phenocryst types documented in basaltic magmas from the Dunedin Volcano. HAB, MAB, LAB denotes high, mid and low alkali basalts, respectively, being characterized by progressively lower contents in alkali/ SiO_2 . a-d: four main types of clinopyroxene (cpx) phenocrysts, displaying diverse textures and compositions. e,f: two main types of plagioclase (pl) crystals. g: two olivine types with distinct Mg-contents (darker: higher Forsterite content) coexisting in the same low alkali lava. h: titanomagnetite phenocrysts are found across most samples, with limited compositional variability.



physico-chemical conditions relevant to magma storage and early differentiation processes, highlighting a crystallization window mainly comprised between 1.0 and 0.7 GPa according to clinopyroxene barometry, suggesting the deeper parts of the plumbing system are comprised between upper mantle and lower crustal depths, in agreement with geophysical data. Multi-stage ascent in the central part of the volcano, where lower alkaline magmas were erupted, is witnessed by an increased complexity of the phenocryst cargo, featuring Mg and Cr-rich relic clinopyroxene cores as well as resorbed and overgrown plagioclase crystals. Highly alkaline basalts in the peripheral part of the DV are feeded directly from lower crustal depths, occasionally carrying along mantle xenoliths. Our study represents the first thermobarometric appraisal of the DV system, and evidences how integration of whole rock and mineral-scale investigation may help in disentangle complex magma source to surface histories in intraplate alkaline volcanoes. Different primitive magma compositions are stored in multiple magmatic reservoirs, located at different depths, and erupted in different sectors of the volcano. As magma composition is modulated by processes in the mantle source, these latter ultimately play a fundamental role in shaping the architecture of the DV plumbing system.



Observing volcanic activity and morphological changes associated with the 3 July and 28 August 2019 paroxysmal eruptions at Stromboli volcano (Italy) using UAVs

Ricci T., Civico R., Andronico D., Del Bello E., Pizzimenti L., Scarlato P., Taddeucci J.

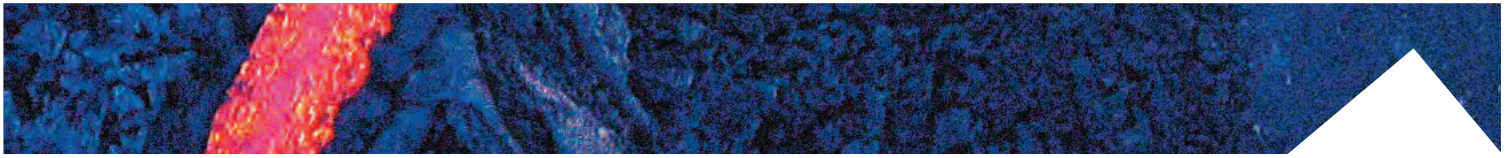
Observing volcanic activity and resolving morphological changes on active volcanoes through time is key to understanding active volcanic processes. Unmanned Aerial Vehicles (UAVs) have recently become a powerful platform for aerial observation and data acquisition allowing close and detailed observation of the volcanic activity up to the eruptive vents. Moreover, they permit a rapidly-deployable, low-cost alternative to both classical manned aerial photogrammetry and airborne lidar.



Fig. 1 | Stromboli, August 4, 2019: aligned vents in the NE sector of the crater terrace (left) and lava flows in the upper Sciara del Fuoco in proximity of the SW sector of the crater terrace.

We therefore decided to use UAVs at Stromboli for a twofold objective: to monitor morphological changes of the volcanic edifice producing accurate, high-resolution digital elevation models (DEMs) and to observe the volcanic activity.

Five high-resolution UAV surveys have been performed since May 2019. Using Structure-from-Motion (SfM) techniques we generated DEMs of the crater terrace area, of lava flows and Sciara del Fuoco. The obtained DEMs have a resolution of 0.2-0.5 m. The comparison of the multi-temporal DEMs allowed for the evaluation of the height and volume variations due to the 3 July and 28 August paroxysms as well as for the months before and after these two

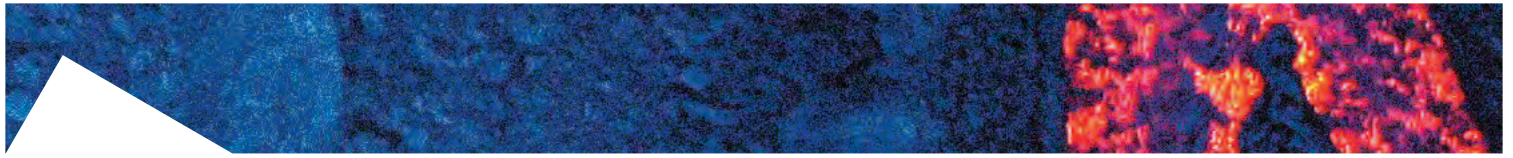


events, for the morphological variations occurred in the crater terrace and for the evolution of the lava flow field.

Since the 3 July paroxysm, UAVs revealed to be fundamental for the observation of the volcanic activity reducing the exposure of operators to volcanic hazards when the INGV video surveillance network (both thermal and visible) in the summit area of the volcano was destroyed.

The combined use of UAVs and SfM techniques are crucial for improving our capabilities to collect frequent and low-cost measures on landscape changes associated with the dynamics of active volcanoes.

The observation of volcanic activity and the data collection, as well as the temporal comparisons of the DEMs, represent a fundamental contribution to volcanic hazard assessment and can support civil protection operations and risk mitigation actions.

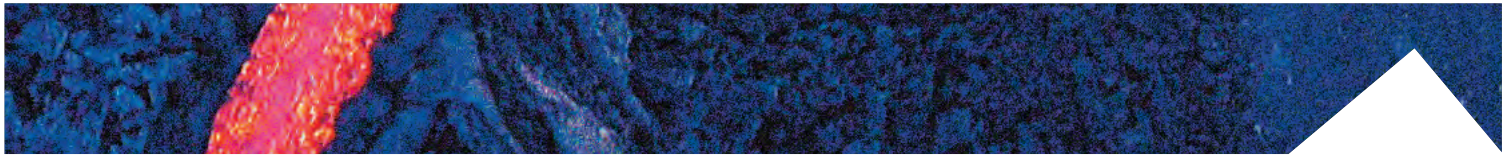


Degassing behavior at basaltic volcanoes: New insights from experimental investigations of different conduit geometry and magma viscosity

Spina L., Cannata A., Morgavi D., Perugini D.

Understanding the intimate link between the dynamics of the magmatic fluids in the feeding system and the related geophysical markers at the surface is crucial for both research and monitoring purposes. However, volcanoes are generally inaccessible to direct observation, for they sink their roots in deep, inaccessible regions of the Earth Crust. This evidence has induced a flourishing number of indirect techniques to reconstruct quantitatively the fluid dynamics and degassing state of active volcanoes and link them to observable parameters at the surface. We reviewed the ample literature addressing degassing state in basaltic volcanoes, particularly by means of 1) the investigation of seismo-acoustic signals and 2) the use of analogue laboratory techniques to mimic shallow conduits. The geometry of the feeding system has a fundamental role in controlling both the behavior of the two-phase mixture and the release of elastic energy, nevertheless its interplay with volcanic flow remains poorly explored or substantially subjected to oversimplification. Therefore, we performed a set of experiments aimed to investigate an unexplored issue, that is the effect of irregularity (i.e. departure from an ideal smooth cylindrical shape) of the conduit surface. The experiments were carried out by providing Air-gas mixture to the analogue conduit through a compressor system, connected to a set of flow-meters (Cryotek Eng). The analogue conduit is hooked to a steel support, which is on turn granting for the suppression of oscillations of the steel support, external to the experimental device. A set of sensors, measuring the elastic signals radiated along the conduit and in the atmosphere were deployed along the experimental conduit. In details, one ceramic shear accelerometer ICP J352C33 model (PCB Piezotronics) with a sensitivity of 0.1 V/g in the band 0.5–10,000 Hz and ii) two piezo-film sensors SDT Shielded Piezo Sensors with a sensitivity of 15–20 mV/ μ strain;) were located at different step along the conduit. One microphone ICP 378B02 model (PCB Piezotronics) with a sensitivity of 50 mV/Pa in the band 7–10,000 Hz (± 1 dB), and ± 2 dB in the band 3.75–20,000 Hz was positioned above the experimental vent.

In order to reproduce different extent of roughness of the conduit surface, we defined a protocol to realize a set of in-



From Spina et al. 2019

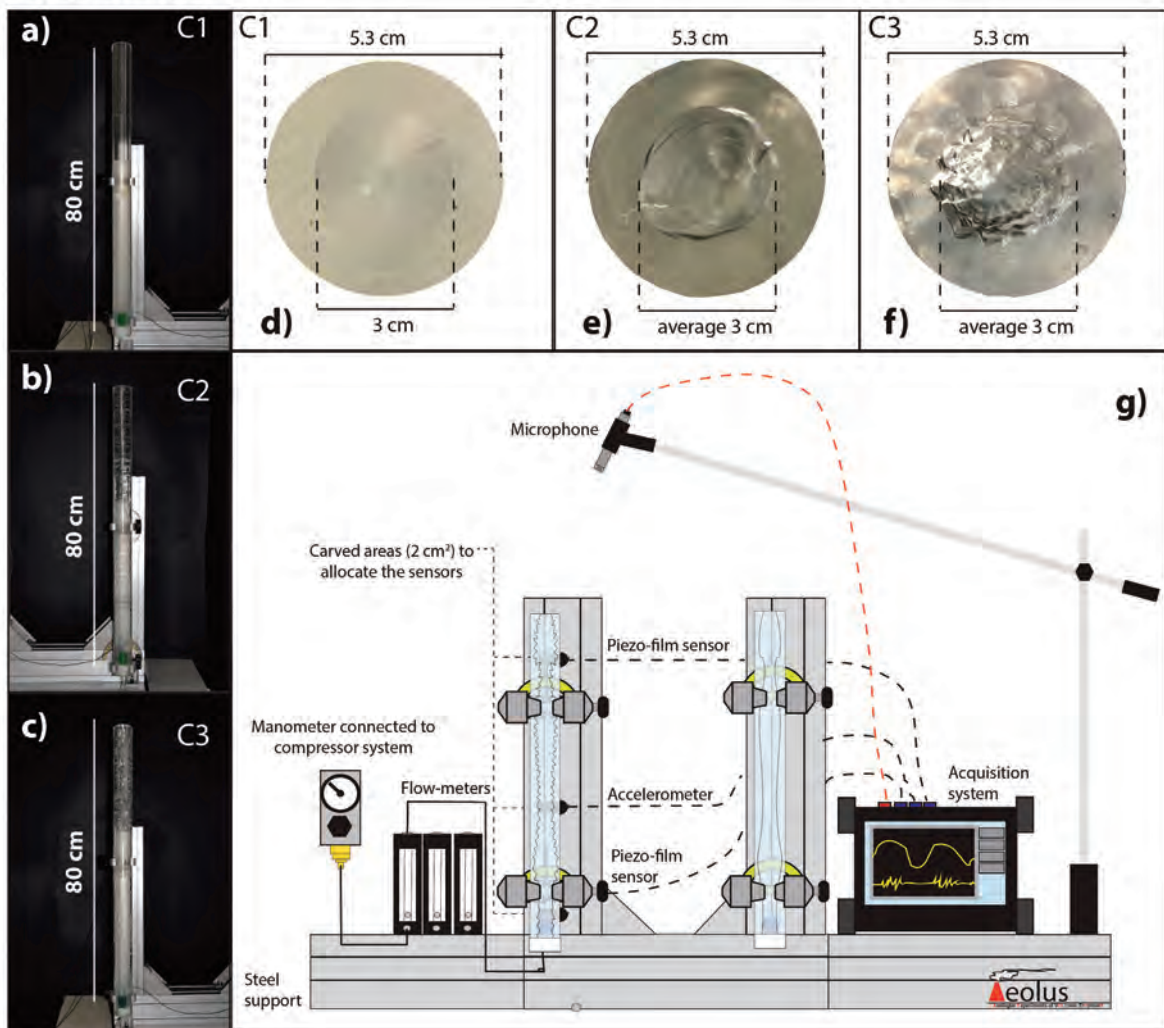
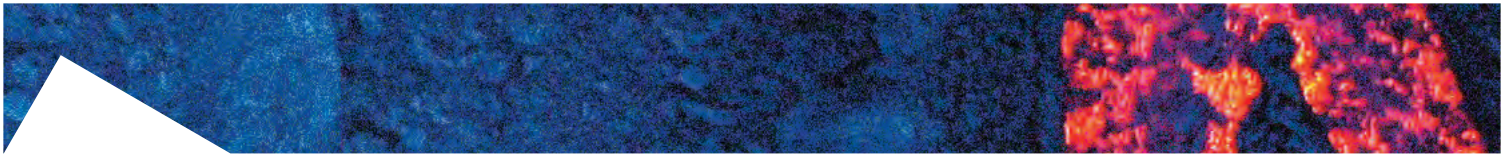


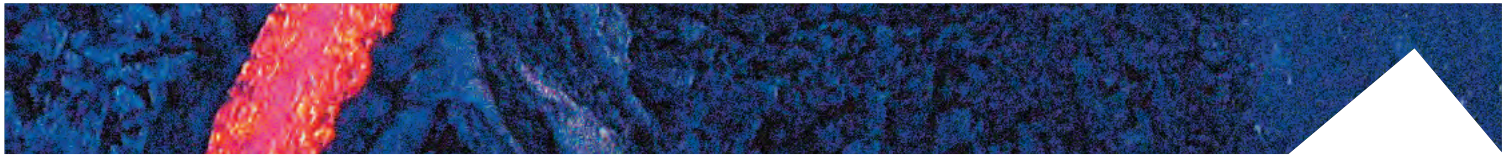
Fig. 1 | (a, b, c): Frontal picture of the experimental conduits C1, C2 and C3, respectively. (d, e, f): Top picture of the experimental conduits C1, C2 and C3, respectively. (g) Sketch of the experimental device (not to scale) for reproducing volcano degassing pattern and measuring the related seismo-acoustic signal (modified from Spina et al. 2019a).

house-made epoxy conduits with various fractal dimension of the internal surface (D_c). Fractal surfaces, generated by using the Matlab code provided by Candela et al. 2009, were processed to obtain a solid mesh representing the conduit mould. The conduit moulds are 3D printed using polylactic acid (PLA) filaments using a Ultimaker 2[®] printer. Then a silicone elastomer (Rhodosil Silicone 3527AB[®]) was poured inside, to obtain the model of the conduit internal volume, that is fixed within plastic tubes with diameter of 5.3 cm. The empty space between the silicone model and the plastic tube is then filled with epoxy Resine 131 AB[®] and dried in the oven at 80 °C for 1 h. After removal of the tubes and of the silicone conduit models, the epoxy conduit sections were polished at their junction



and longitudinally glued together.

Several experiments were performed exploring various degassing patterns (bubbly, slug and churn flow) using silicone oil as a proxy for magma and by changing systematically: 1) injected gas flux (5 to 180×10^{-3} l/s); 2) analogue magma viscosity (10 to 1000 Pas); 3) fractal dimension (D_c) of the conduit surface (i.e. $D_c=2$, $D_c=2.18$ and $D_c=2.99$). Results show that viscosity strongly influences the transition among degassing patterns and the recurrence rate of slug bursts at the surface. Moreover, we observed an increase of the exponent of the power law equation linking squared seismic amplitude to gas flow rate with conduit roughness; the opposite trend was noticed with increasing liquid viscosity. These results have important implications for linking seismic tremor to eruption source parameters such as the volume discharge rate at different volcanoes or for investigating its temporal evolution at a single vent.

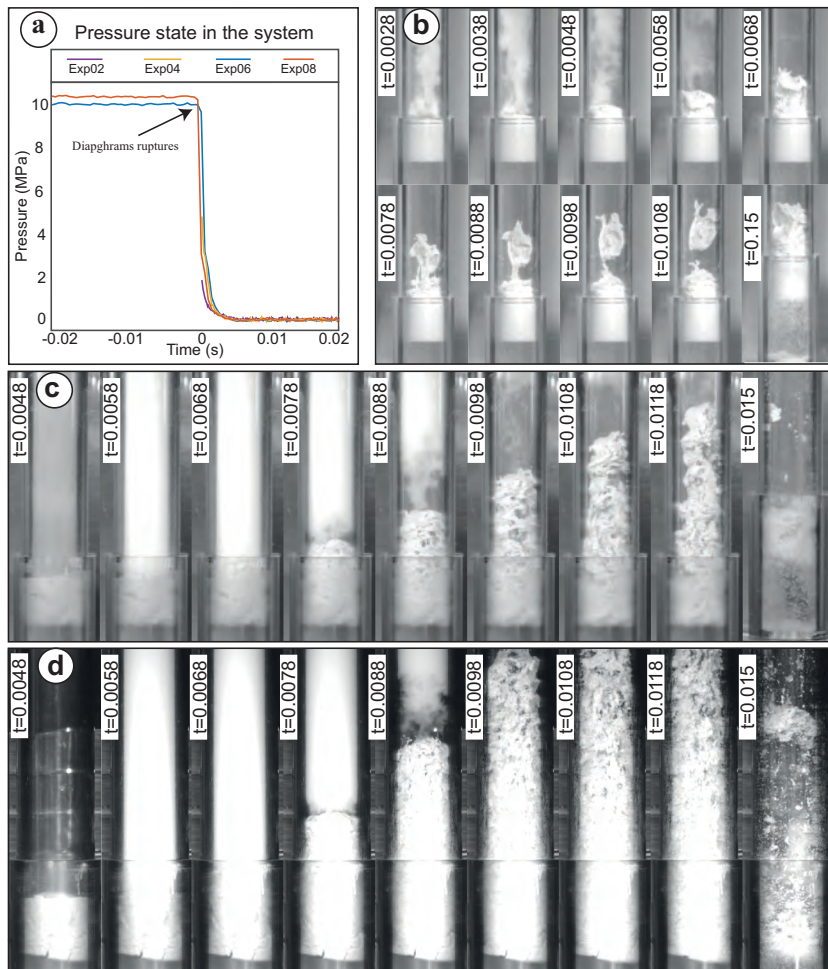


Gas mobility in rheologically-layered volcanic conduits: The role of decompression rate and crystal content on the ascent dynamics of magmas

Spina L., Morgavi D., Costa A., Scheu B., Dingwell D.B., Perugini D.

The rheological behavior of magmas, which is a fundamental aspect of the state of ascending fluid, is highly sensitive to crystallinity, liquid composition and vesicularity, that are in turn expected to dramatically change in response to the new thermodynamic conditions. As a result, rheological contrasts at shallow depth within the feeding systems of volcanoes are likely to be ubiquitous. Generally, such rheological contrasts represent the transition from a low viscosity crystal-poor, bubble-free, water-rich melt to a highly viscous crystal-rich, vesicular magma containing a water-poor melt. Notably, the rheology of the shallow conduit has been found to modulate flow dynamics and eruptive style, with obvious implication for hazard evaluation. With the aim of investigating the viscous flow dynamics of rheologically-layered volcanic conduits, we performed decompression experiments in a shock tube using a magma analogue system characterized by a low-viscous Layer L (10 Pas) at the bottom and a high-viscous particle-bearing Layer H (≥ 1000 Pas) at the top. Silicone oil was used as a proxy for basaltic magma, and mixed with spherical glass beads to account for the contribution to the rheological contrast deriving from shallow degassing and crystallization. After complete sample saturation in Ar-gas, decompression experiments were performed by varying systematically: 1) the decompression rate (ca. 10^{-2} or 10^4 MPa/s); 2) the crystal content in the high viscosity magma (0, 10, 30 and 70 vol.%); 3) the volume ratio of the two rheological layers (Layer H/Layer L equal to 0.6 or 0.3). Gas mobility was tracked by using a high-speed camera with sampling rates of 5000 and 50 fps for the instantaneous and slow decompression experiments, respectively, and a pressure sensor located at the top of the experimental conduit.

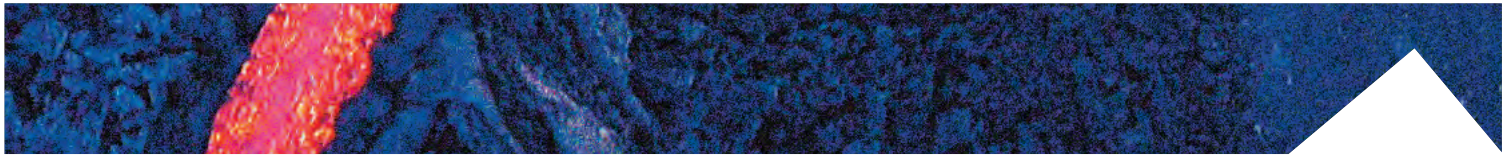
Our results indicate that decompression rate exerts the most dramatic role, yielding changes in time-scale of outgassing up to two orders of magnitude, and affecting the style of decompression response (permeable outgassing or fragmentation). In fast decompression experiments, the solid fraction affects the spatial pervasiveness of fragmentation of Layer H, ranging from a complete absence of fragmentation (0 vol.%) to complete disruption (70 vol.%) at the same



From Spina et al. 2019b

Fig. 1 Details of fragmentation process in particle-bearing experiments. (a) Pressure curves for fast decompression experiments without (Exp02) and with (Exp04-Exp06-Exp08) particles. (b, c, d) Snapshots of Exp04 (10 vol.%), Exp06 (30 vol.%) and Exp08 (70 vol.%), respectively. Spatial scale is provided by the diameter of the experimental conduit, which is equal to 2 cm (modified from Spina et al.2019b).

decompression rate, directly influencing the fragmentation efficiency of the upper layer. Additionally the solid fraction strongly modulates gas mobility, and affects the extent of mingling in the experimental conduit. These results demonstrate that the that rate of crystal growth at the shallow portion of the magmatic column severely affects permeability; and that the control exerted by crystallinity on gas loss has direct implications for hazard assessment.



A multi-parametric characterization of the explosive activity of Batu-Tara Volcano (Indonesia)

Spina L., Del Bello E., Ricci T., Taddeucci J., Scarlato P.

Batu Tara is an active volcano located in the Lesser Sunda Archipelago (Indonesia), often associated to Stromboli volcano for morphological similarities (i.e. the analogue dimension of their edifice and the presence of a Sciara del Fuoco-like depression) and short-term eruptive behavior. According to Darwin Volcanic Ash Advisory Center, the volcano is active since 2007, nonetheless due to its remote location, an exhaustive characterization of the Batu Tara activity is lacking. With this aim, we conducted a multi-parametric campaign of three days of almost continuous recording (04-06 September 2015). The FAMOUS setup was deployed at 1226 m from the active vents and included: 1) high-speed visible camera acquiring images at 500 frames per second (fps); 2) a thermal infrared (FLIR) camera acquiring at 50-200 fps; 3) a visible time-lapse camera (GO-PRO) acquiring at 0.2-0.5 Hz (2 - 5 s interval); 4) a broadband microphone (freq. range of kHz to 0.1 Hz) sampling at 10 kHz. During the field campaign the eruptive activity was characterized by Strombolian-Vulcanian explosions. Here, data from the thermal camera and the microphone are compared to obtain a comprehensive description of Batu Tara explosive activity.

A dataset of 72 acoustic events was selected using STA/LTA algorithm, fixing a short and a long time window of 1 and 5 seconds, respectively, a trigger threshold equal to 4 and a de-trigger threshold of 1.5. After careful evaluation of the frequency distribution of the spectral amplitude of the acoustic events, the signal was sub-sampled at 100 Hz. Acoustic events show a relatively widespread duration and peak-to-peak amplitude with a mean value of 8 seconds and 34.3 Pa, respectively. Spectral analyses, performed on a window of 15 seconds, reveal a peak frequency of 1.20Hz. We also evaluated the mean frequency (i.e. center of mass of the spectrum) and the percentages of frequencies above 3 Hz. Such parameters provide an estimate of the spectra distribution in case of non-monochromatic events. The mean value of mean frequency corresponds to 3.5Hz, reflecting the presence of higher frequency component in the spectra. All the same, although most of the dataset have percentage of frequencies higher than 3 Hz below 30%, in some cases such parameter can reach up to 70%. The relative presence and dominance of higher frequencies in the spectrum reflects on the

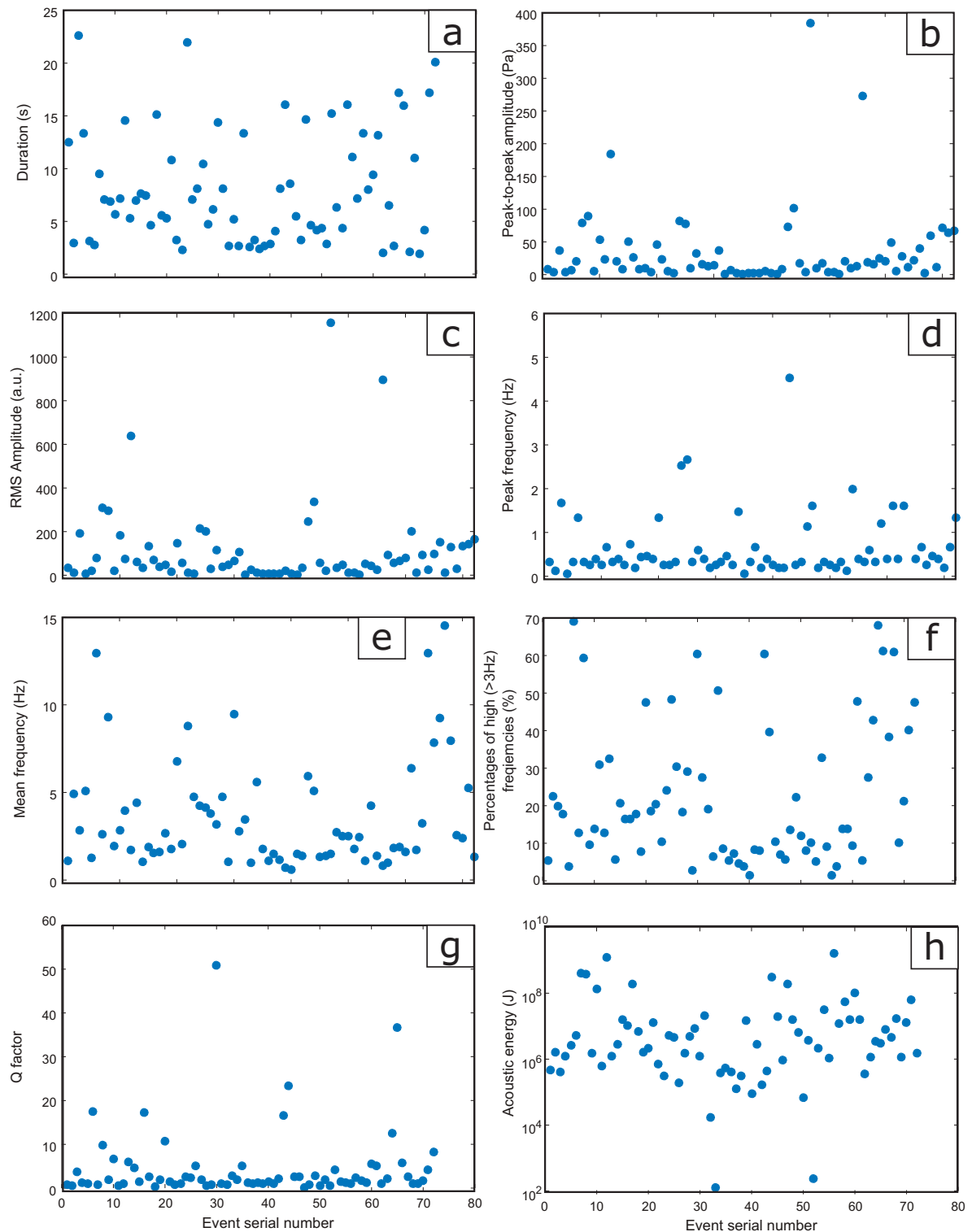
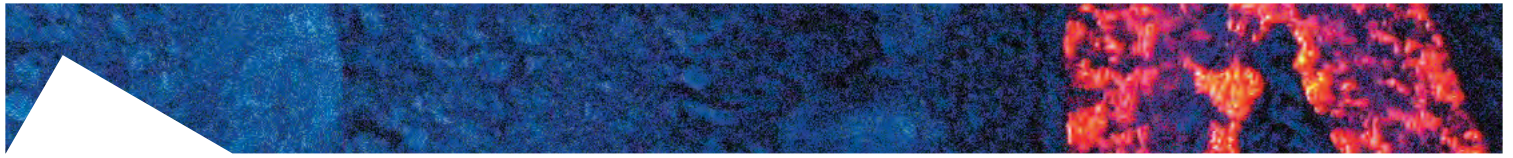
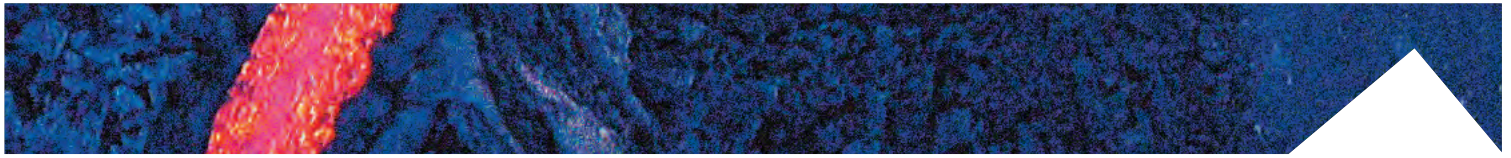


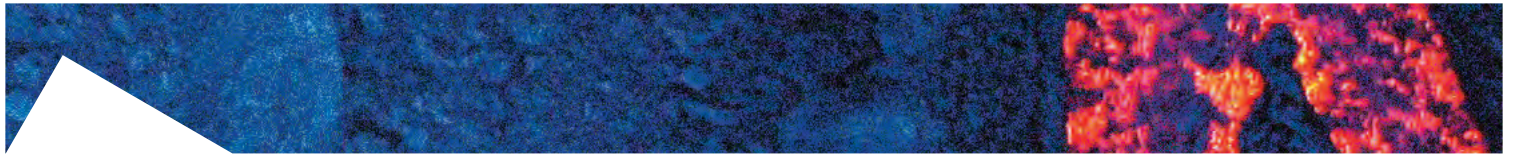
Fig. 1 | Results of different analyses in time and frequency domain of the acoustic events associated to explosive activity from Batu-Tara volcano. (a) Duration; (b) Peak-to-peak amplitude, (c) Root-Mean-Square amplitude, (d) Peak frequency, (e) Mean frequency, (f) Percentages of frequencies above the threshold of 3 Hz, (g) Quality factor, (h) Acoustic Energy (J).



family classification of the acoustic events, that was performed by cross-correlating the spectra, following. Accordingly, the acoustic dataset can be classified in six families, covering the 75% of the dataset, and mainly reflecting the monochromatic nature of the events or the different partitioning of the energy among two frequency peaks below 5 Hz. Finally, we evaluated the acoustic energy and the Quality factor. The former was estimated following Zobin et al. (2019) and –with few exceptions– range from 10^4 to 10^9 J, coherently with literature data on Strombolian-type eruptions. Quality factors were evaluated using the Sompi technique with an order of the autoregressive model of 16, and are mostly clustered below the value of 10.

Concerning the thermal signal, we scrutinized the data to identify transients marking explosive activity by using STA/LTA trigger with a length of the short and long windows of respectively 20 and 800 frames, a trigger and a de-trigger threshold of 4 and 1. Among the 83 triggered thermal transient, a subset of 48 thermal events with clear acoustic counterparts was selected. Different parameters were investigated by using in-house-built algorithms such as the maximum high and velocity of the bombs, the average plume high and velocity, the duration and energy of the thermal transients. Finally, a qualitative parameter, i.e. the ash index, was assigned basing on the ash content of the explosion by visual observation.

Notably the acoustic energy scales with the maximum velocity of the ejected bomb, suggesting that overpressure of the gas slug reaching the surface is controlling both parameters. Additionally, we found that the highest quality factor in the dataset are commonly linked to low ash index (i.e. ash-free events).

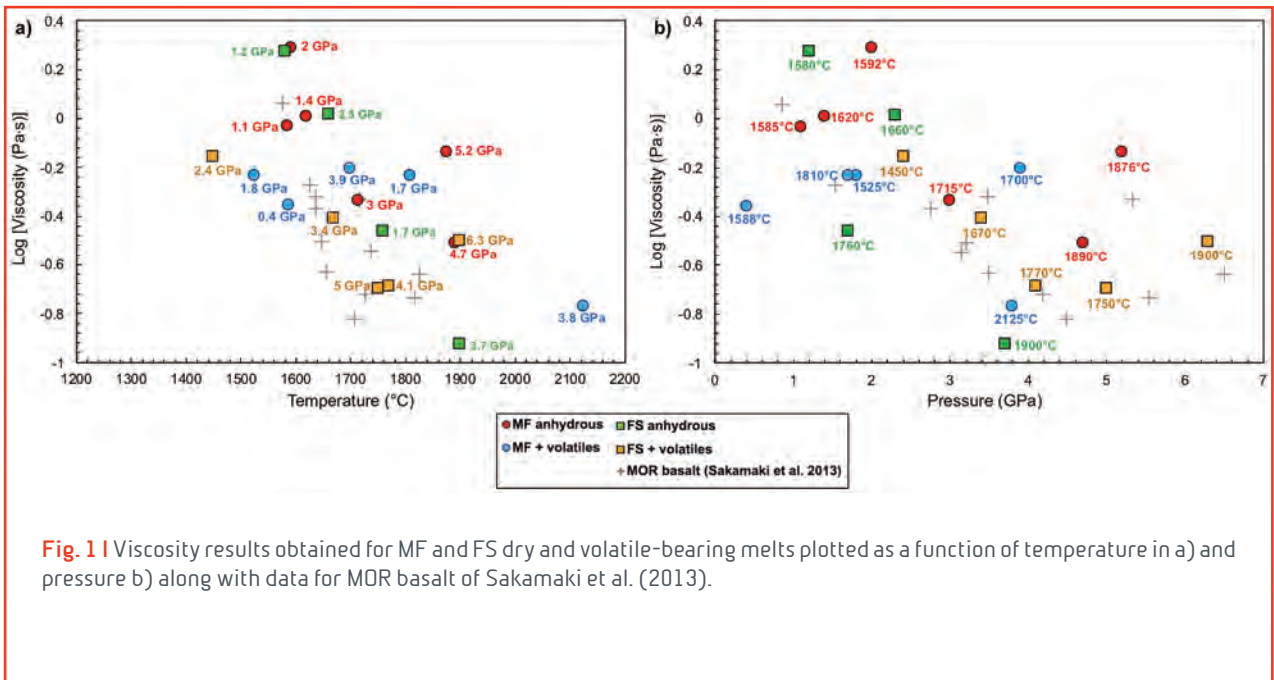
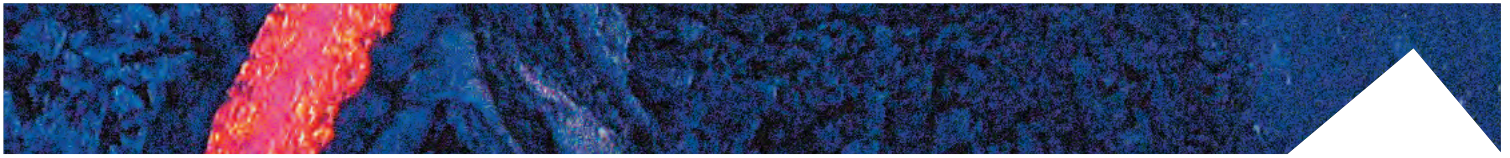


In situ viscosity and structural measurements of anhydrous and volatile-bearing primitive magmas of Alban Hills and Mount Etna at upper mantle pressure-temperature conditions

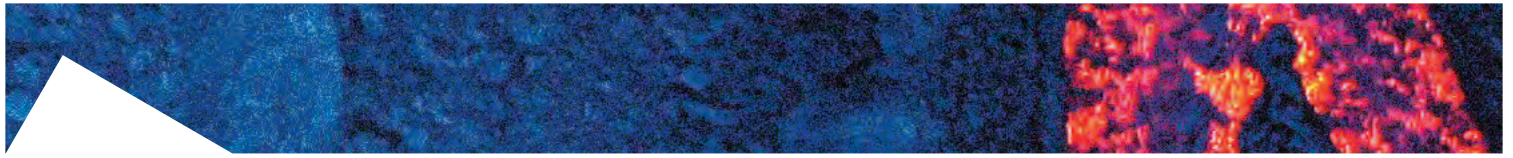
Stopponi V., Stagno V., Misiti V., Poe B. T., Romano C., Scarlato P.

Viscosity is the key parameter controlling the dynamics of magmas from the source rock in the mantle up to shallower depths and it is intrinsically linked to the atomic arrangement of their structure. Mantle magmas can dissolve significant quantities of volatiles (e.g. CO_2 , H_2O) and whether they stagnate at depth or sustain the feeding system of active volcanoes depends on their rheological properties with respect to the surrounding mantle. Therefore, the knowledge of their viscosity at conditions of their formation is of viscosity and structure of K-rich basalt (MF) and Mg-rich picobasalt (FS), representative of the most primitive lavas erupted from the active volcanic districts of the Roman Province (Alban Hills) and Mount Etna, respectively, both showing geochemical evidence of a mantle origin.

In order to perform such experiments, a total of four different glasses were synthesized from either natural powdered rock samples or oxide and carbonate mixtures as starting materials. Synthesis of glasses was conducted at the HP-HT laboratory of INGV (Rome) using the furnace to obtain a dry homogeneous glass, while the QUICKpress was used to add CO_2 and H_2O to the dry glass through HP-T experiments. Viscosity and structural experiments were conducted at pressures of 0.4-6.3 GPa and temperatures between 1450 and 2125°C using the Paris-Edinburgh press combined with the in-situ X-ray synchrotron facility at beamline 16 BM-B of HPCAT, at Argonne National Laboratory (Lemont, IL, USA). Viscosity experiments were carried out using the falling sphere technique. The use of a high-speed camera combined with ultrafast X-ray imaging allowed the descent of a Pt sphere through the molten sample to be recorded and then tracked as function of time. Viscosity was then calculated from the determined terminal velocity by using the Stokes law. Melt structure measurements were carried out using multi-angle energy dispersive X-ray diffraction at high pressure and high temperature in order to determine the structure factor and interatomic distances (T-O, T-T where T= Si^{4+} , Al^{3+}) through the reduced pair distribution function. The



recovered quenched products from in-situ experiments were then analysed with the JEOL JXA-8200 electron microprobe (INGV) to investigate their texture, chemical composition and crystallized phases, where present. The experimental viscosity data range between 2 and 0.1 Pas as a function of P and T (Figure 1) with T exerting a strong effect at comparable pressure conditions. We observed a decrease in viscosity with increasing pressure up to ~4.5 GPa, followed by a positive correlation after such turnover pressure. This is attributable to changes in T-O length as determined by our structural measurements and by Sakamaki et al. (2013) for MOR basalt. Our viscosity data allowed the calculation of the hydrostatic melt mobility, proportional to the gravity-driven melt transportation, which was estimated to vary from ~0.6 to 0.2 g·cm⁻³·Pa⁻¹·s⁻¹ within the compositional range presented in this study and to model their migration rate through mantle lithologies as a function melt fraction, grain size, chemical composition and depth.



K in omphacite geobarometer

Zordan S., Nestola F., Misiti V.

The project aimed to estimate experimentally the K solubility in omphacitic pyroxenes at different P-T interval to construct a possible relationship between pressure and K content.

It is well known that the increase of P in omphacitic clinopyroxenes could be accompanied by an increase of K in its crystal structure (substituting Ca and Na). Nevertheless, so far a reliable geobarometer based on the K content in clinopyroxenes does not exist yet. Thus, we performed a series of experiments using a natural omphacitic pyroxene coming from the MUST (Museo Universitario di Scienze della Terra, La Sapienza University, Rome). The starting material had a K_2O content of 0.58 wt %.

We run 3 experiments (as reported in table 1, Figure 1a, b and c) using omphacite crystals doped with different amount of K_2CO_3 (from 2.78 to 4.30 wt%) and temperature, pressure and experiment duration as reported in Table 1.

SAMPLE	EXP	P (GPA)	T °C	T (H)
CPX1	QP13-22	1.5	650	72
CPX2	QP13-24	2.0	800	48
CPX5	QP13-26	2.5	900	12

Table 1 | Pressure and temperature conditions at which the experiments were run. In the last column the duration time is reported for each experiment.

The chemical analyses performed on the three samples here investigated show that increasing the pressure and temperature the K_2O content increases linearly from 0.69 up to 1.63 wt%. Although we could only use three samples, however, as shown Figure 2, the pressure – K_2O content could provide a preliminary linear trend with the equation reported within the Figure.

Comparing our equation with estimates of pressure based on the K_2O contents in literature, we can definitively state that our data are in very good agreement.

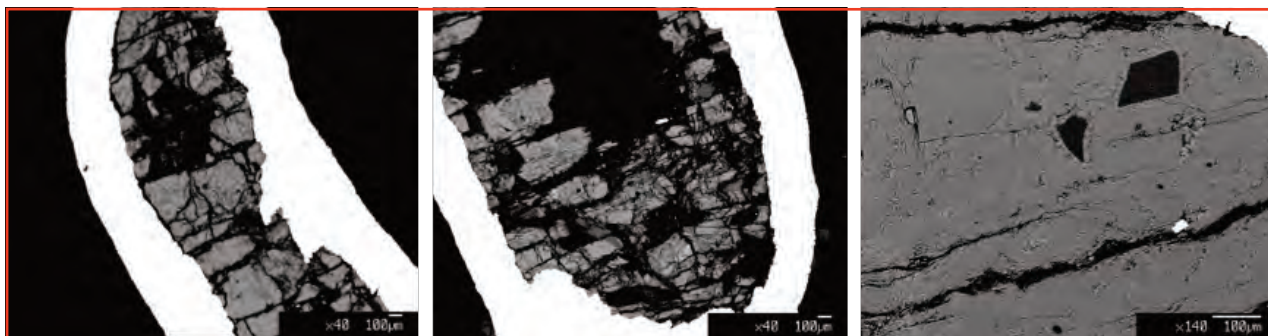
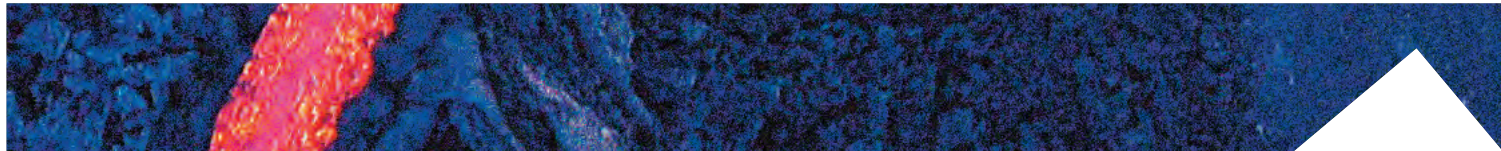


Fig. 1 | Samples of the clinopyroxenes exposed after the experiment runs. On the left image the sample CPX1, whereas the sample CPX2 is shown on the middle image. The sample CPX 5 is relative to the right image.

The experimental approach used in this work is very promising and could provide a very reliable tool to obtain pressure values for natural clinopyroxenes from different geological environments.

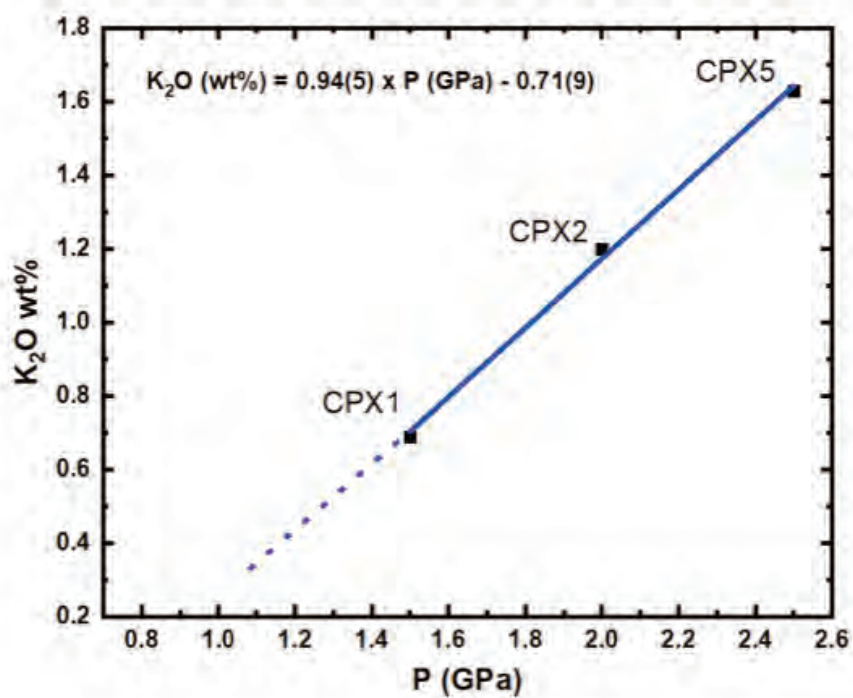
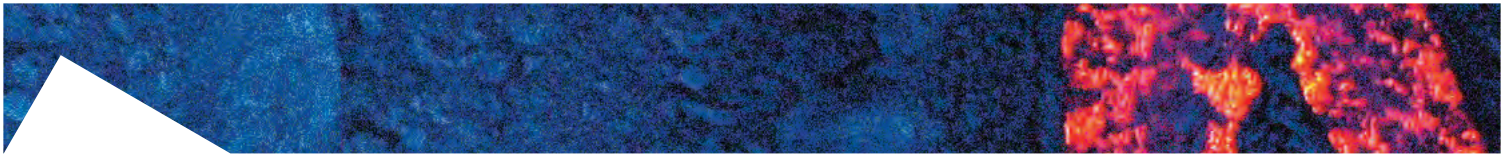


Fig. 2 | K₂O content versus pressure for the three samples analyzed in this work.



The southernmost occurrences of the volcanic-rich horizon of 5.5 Myr in Central Italy

Potere D., Iezzi G., Scisciani V., Nazzari M.

The 5.5 Myr of the Messinian volcanic-rich layer has been already studied in the outcrops along the central portion of Apennines, from Piavola (Forlì-Cesena, Emilia Romagna) to Basciano (Teramo, Abruzzo). It has been interpreted either like a primary fallout or as a secondary turbiditic deposit. In this study the two southernmost sites of the volcanic-rich horizon are investigated by field observations, mesoscopic and microscopic (optical and electronic) methods, XRPD, EPMA-WDS and bulk chemical analyses. Here, two sections are considered, located close to the villages of Castiglione a'

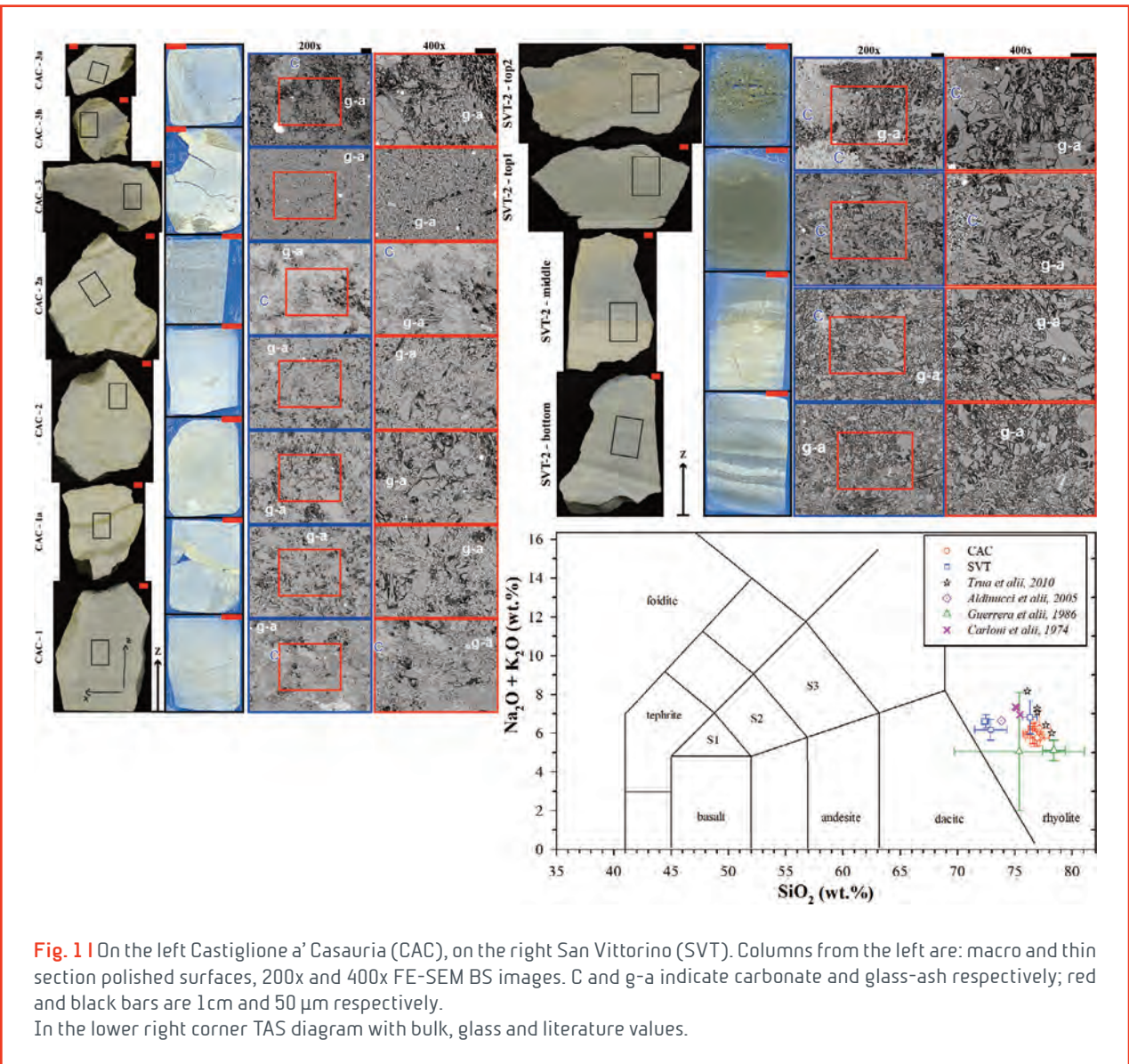
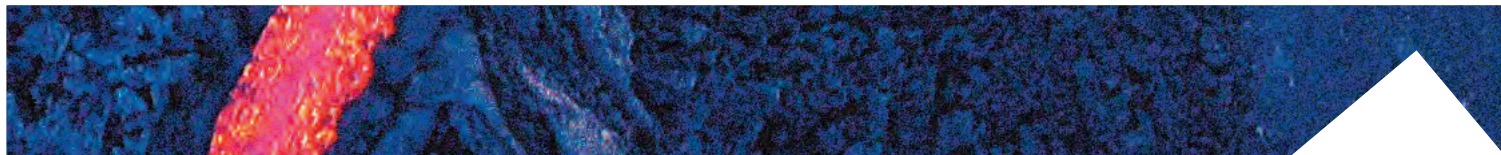


Fig. 1 | On the left Castiglione a' Casauria (CAC), on the right San Vittorino (SVT). Columns from the left are: macro and thin section polished surfaces, 200x and 400x FE-SEM BS images. C and g-a indicate carbonate and glass-ash respectively; red and black bars are 1cm and 50 μm respectively. In the lower right corner TAS diagram with bulk, glass and literature values.



Casauria (CAC) and San Vittorino (SVT), in the sedimentary Laga basin. Four and fifteen samples were collected from SVT and CAC, respectively.

The SVT XRPD patterns, collected with a Si nominal zero background sample holder, show the presence of montmorillonite (MNT), biotite (BT), illite (ILL), quartz (QZ), sanidine (SND), anorthite (AN), clinopyroxene (CPX), calcite (CLC) and dolomite (DLM), plus a clear presence of a non-crystalline silicate glass. The CAC XRPD spectra are similar, but free of QZ and CPX. Starting from these results and according to stratigraphy, we prepared four SVT and seven CAC thin sections, as well as macro polished surfaces imaged with an high-resolution scanner (HRS) to investigate macro textural and sedimentary features. The polished surfaces of thin sections were observed with transmission optical microscopy with magnifications of 25x and 100x and with FE-SEM in BS mode with five progressive magnifications from 100x to 1600x. Optical and BS-SEM analyses show that all these samples are mainly composed of blocky glass shards and bubble-wall fragments, with a minor amount of tubular micro-pumices. In line with XRPD results, the silicate crystal content detected by microscopic analyses is very low, about ≤ 5 area%; the abundance of carbonates is instead variable (Figure 1).

The bulk compositions of two SVT and two CAC samples are rhyolitic in the TAS diagram, with a SiO_2 , LOI and $\text{CO}_2 + \text{H}_2\text{O} + \text{S}$ averaging on 64(1) and 68(2), 11(0) and 12(1), 11(0) and 11(1) wt.%, respectively (Figure 1). The glass composition determined with EPMA indicate again a rhyolitic composition, with a SiO_2 and $\Delta\text{Fe}_2\text{O}_3(100\% - \text{tot_Fe}_2\text{O}_3)$ averaging on 71(0) and 71(0) and from 8(1) to 8(0) wt.%, respectively. Thereby, the amount of H_2O still dissolved in the glass is extremely high; the amount of LOI close to 11 wt.% are associated to H_2O and OH contained in phyllosilicates (MNT, ILL) crystallized by weathering processes, plus those contained in the glass. Since MNT and ILL are not detected by SEM into the glass shards, it is possible to conclude that they precipitate at the boundaries or among ash particles.

The volcanic deposits have very similar textural, mineralogical and geochemical features between themselves and are also very close to those already investigated in the northern outcrops. Their stratigraphic attributes plus the presence of carbonate phases suggest that SVT and CAC are remobilized volcanic deposits. The more southern deposit (Basciano, Teramo) reported in Trua et al., 2010 is located about 30 and 40 km NNW away from CAC and SVT. Therefore the source(s) of CAC and SVT should be Basciano or a more southern location.

8.2 ROCK PHYSICS AND EARTHQUAKES

How hot is a lab-earthquake?

Aretusini S., Cascajero A.N., Spagnuolo E., Tapetado A., Vazquez C., Di Toro G.

Frictional heating in faults during seismic slip induces a temperature increase on the rubbing contacts and within the slipping zone which activates deformation processes and chemical reactions resulting in dynamic weakening.

An independent measurement of temperature would allow to correlate frictional strength with temperature and to constrain the deformation processes and associated chemical reactions activated during seismic slip. So far, in-situ temperature measurements performed at high acquisition rates (from kHz to MHz) and high spatial resolution ($< 0.1 \text{ mm}^2$) were impossible to achieve due to the large thermal inertia of traditional techniques (i.e., thermocouples). As a consequence, temperatures in the slipping zone sheared at seismic slip rates (1 m/s) were often modelled numerically using

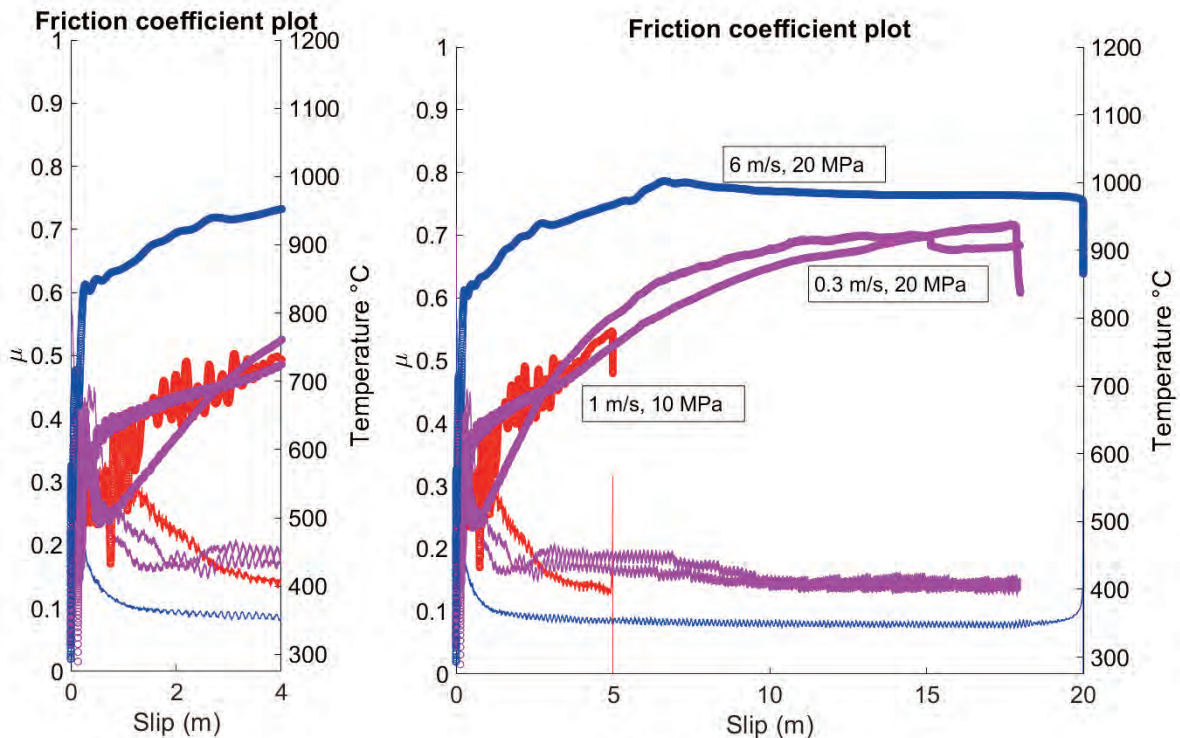
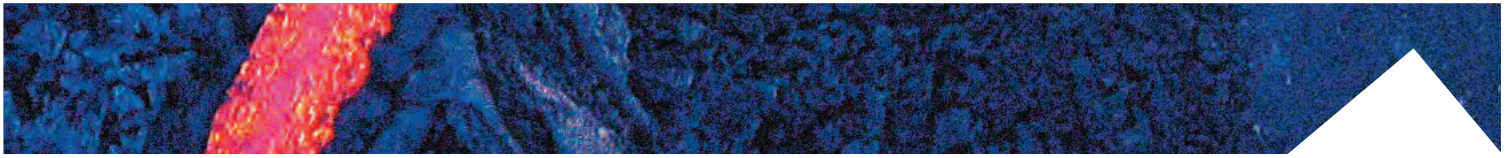


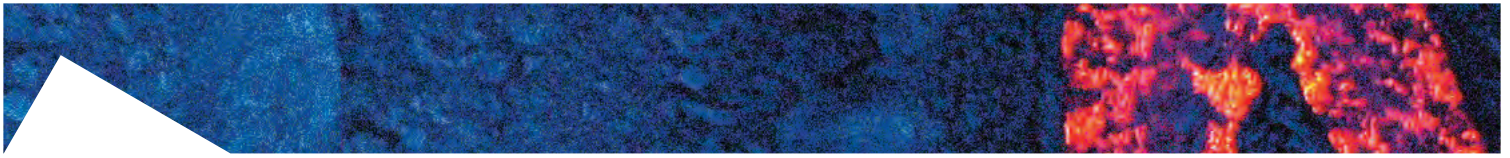
Fig. 1 | High-velocity friction experiments and temperature measurements of Carrara marble bare surfaces. Friction coefficient (i.e., the ratio of shear stress and normal stress) is presented versus fault displacement for four high velocity friction experiments. With increasing temperature, dynamic weakening increases. The lowermost friction coefficient is achieved at temperatures of ca. 980 °C, coincident with a temperature plateau which indicates the occurrence of decarbonation reaction.



the frictional power (shear stress x slip rate) dissipated on the slipping zone as an input parameter, but by making poorly constrained estimates about (1) the partitioning of the dissipated power between frictional heating and wear processes or, worse, (2) other energy sinks that would result in the buffering of the temperature increase (e.g., endothermic reactions).

Here we reproduced earthquake slip in the laboratory via high velocity friction experiments (SHIVA rotary apparatus, INGV, Rome) performed on Carrara marble rock samples, slid at 20 MPa effective normal stresses, slip rates ranging from 0.03 to 6 m/s, up to 20 m of total displacement. During the experiments, the bulk temperature of the slipping zone was measured at acquisition rate of 1 kHz with optical fibers conveying the IR radiation from the hot rubbing surfaces to a two-colour pyrometer.

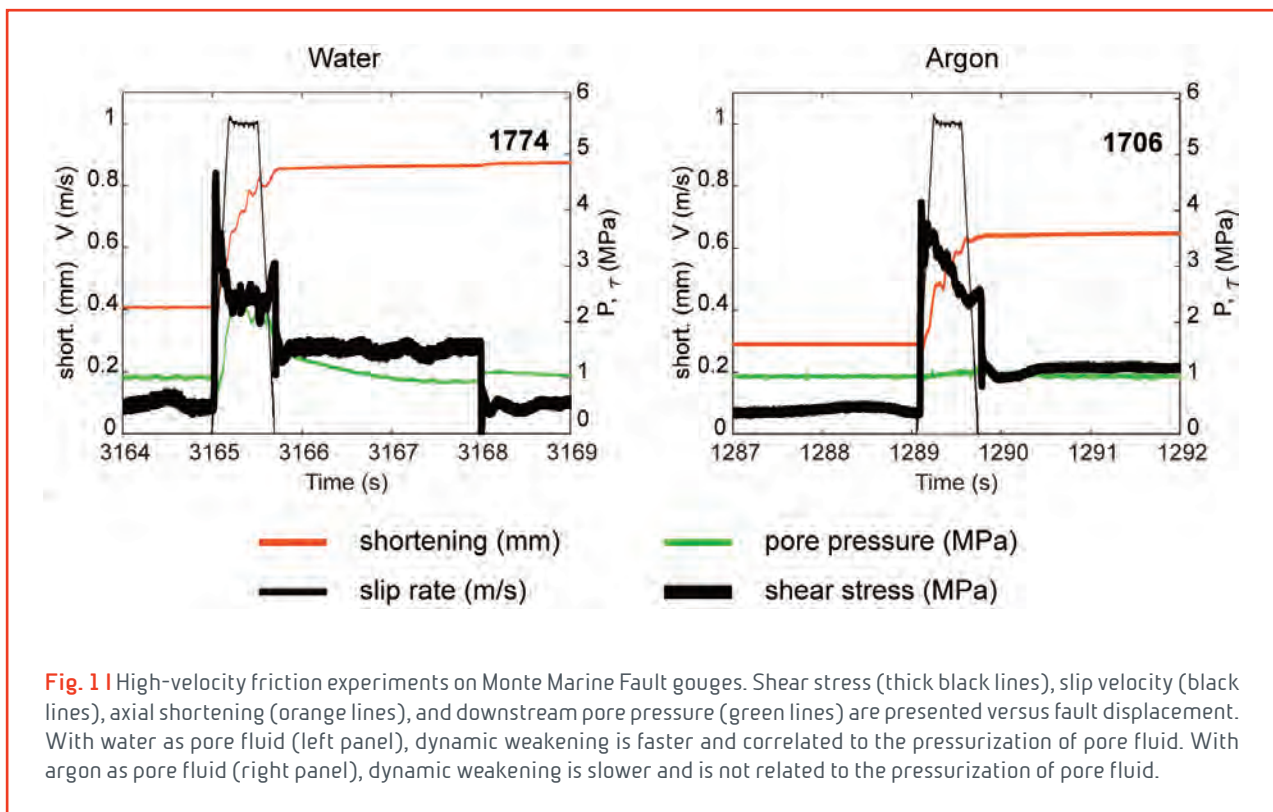
Our data provide the first real-time measurements of the bulk temperature developing by frictional heating and of the dependence of frictional heating with slip rate and displacement during seismic slip in carbonate-built rocks. These and future similar experiments will shed light on the mechanics of carbonate-hosted earthquakes, a main hazard in the Mediterranean and other areas worldwide.



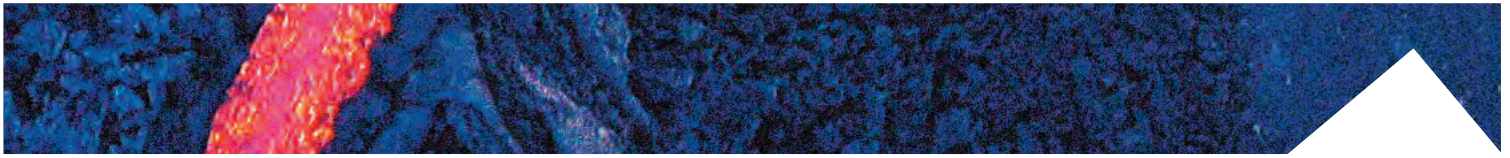
Dry vs wet deformation processes during seismic slip under fluid pressurized conditions in natural carbonate fault gouge

Cortinovis S., Aretusini S., Nazzari M., Di Toro G., Balsamo F.

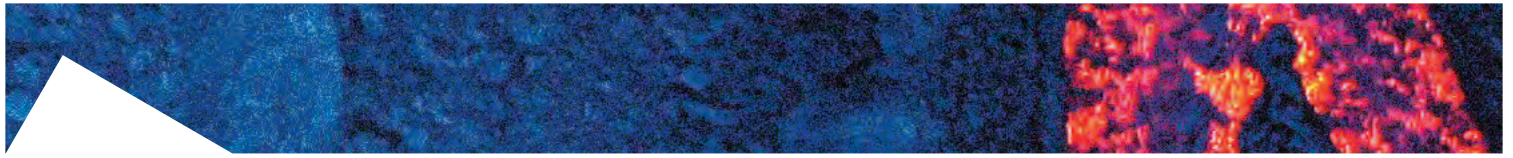
Seismic rupture propagation is influenced by the presence of pressurized fluids, as demonstrated in many published studies. This is especially valid in carbonate rocks, where the occurrence of water in proximity of the slip surface favours the failure of asperities and consequently fault weakening behaviour. It is proved that water-dampened gouges weaken faster than in room-dry condition, to a higher steady-state shear stress. Within this study, we present a series of friction experiments performed with the Slow to High Velocity Apparatus - SHIVA (HPHT lab, INGV, Roma) on a natural fault gouge of mixed dolomite (80%) and calcite (20%) collected in the damage zone of the Monte Marine Fault



(Central Apennines, Italy). We perform experiments at effective normal stresses of 1 and 5 MPa, slip velocities of 0.001 m/s and 1 m/s, and a total displacement of 0.5 m in both dry and wet conditions. We examine the influence of pore fluid pressure using first water as pore fluid, to simulate wet conditions, and then Argon as pore fluid, to simulate dry conditions. For the first time, we measure pore fluid pressure during slip thanks to the presence of a pressure transducer



located on the downstream of the pore fluid pressure circuit. Mechanical data show that carbonate gouges sheared at seismic velocities become weak because of water pressurization. Combining mechanical data and microstructural analysis, we show that water-saturated compared to argon-saturated gouges are weaker at seismic slip rates implying that pore pressure increase is a more effective weakening mechanism than comminution and nanoparticle plastic deformation.



Friction experiments on anorthosite gouges: implications for the mechanisms of long runout landslides on the moon

Magnarini G., Aretusini S., Mitchell T.M., Di Toro G., Schmitt H.H.

Evidence for the presence of a long run out landslide at the Apollo 17 landing site opened important implications about mechanisms of reduction of friction on planetary bodies in the absence of an atmosphere and water availability. Dry granular fluidization involving interaction between regolith particles has been considered the most likely process during emplacement of the Apollo 17 landslide, as well as for other lunar mass-wasting instances discovered in recent years thanks to new high-resolution imagery. To simulate the landslide event we performed friction experiments with SHIVA to explore the dynamic weakening mechanisms during landslide emplacement in totally dry environment. In particular, we tested anorthosites from the ESA Sample Analogue Curation Facility (Hawell, Oxfordshire), ground

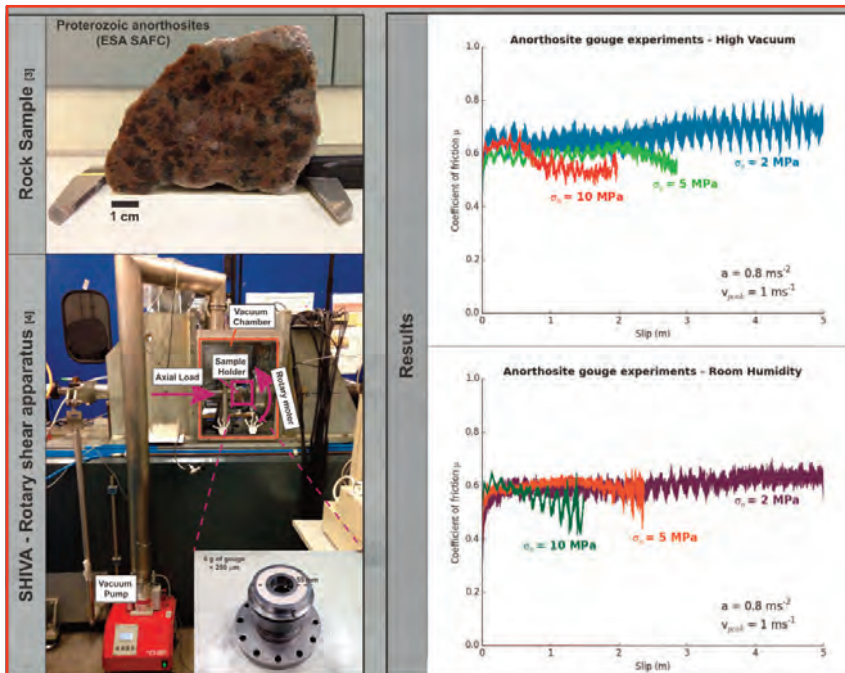
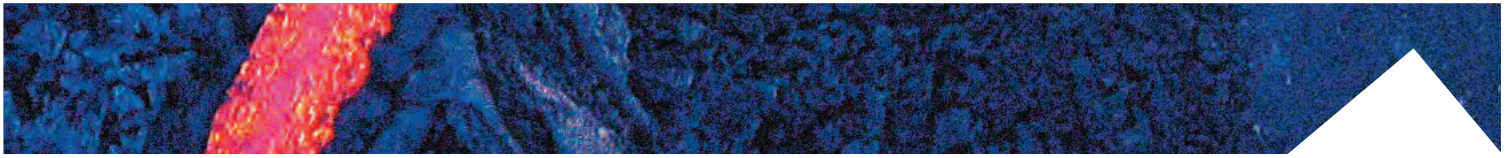


Fig. 1 | High-velocity friction experiments on powdered anorthosites to replicate landslides occurring on the Moon surface. a) Starting material, proterozoic anorthosites (ESA SAFC). b) Slow to High Velocity friction Apparatus (SHIVA, HPHT laboratory, INGV, Rome) and experimental setup for the powdered rock friction experiments. c) Experimental results presented as friction coefficient versus fault displacement, under high vacuum (top panel) and room humidity (bottom panel) conditions. At the tested conditions, dynamic weakening is not triggered and friction coefficient remains high ($\mu=0.6$).

to a fault gouge (grain size $<250 \mu\text{m}$). High velocity friction experiments were run at 2, 5, and 10 MPa under vacuum dry ($<10^{-4}$ mbar) and room humidity conditions imposing slip pulses with 0.8 m/s^2 acceleration, 1 m/s peak velocity, and up to 5 m of displacement. Dynamic weakening was not observed suggesting that thermal weakening processes might be subordinated to other processes which still need to be investigated.



Beyond Byerlee friction, weak faults and implications for slip behavior

Collettini C., Tesi T., Scuderi M.M., Carpenter B.M., Viti C.

Some faults are considered strong because their strength is consistent with the Coulomb criterion under Byerlee's friction, $0.6 < \mu < 0.85$. In marked contrast, numerous studies have documented significant fault weakening induced by fluid-assisted reaction softening that generally takes place during the long-term evolution of the fault. Reaction softening promotes the replacement of strong minerals with phyllosilicates. Phyllosilicate development within foliated and interconnected fault networks has been documented at different crustal depths, in different tectonic regimes and from a great variety of rock types, nominating fluid-assisted reaction softening as a general weakening mechanism within the seismogenic crust. This weakening originates at the grain-scale and is transmitted to the entire fault zone via the interconnectivity of the phyllosilicate-rich zones resulting in a friction as low as $0.1 < \mu < 0.3$.

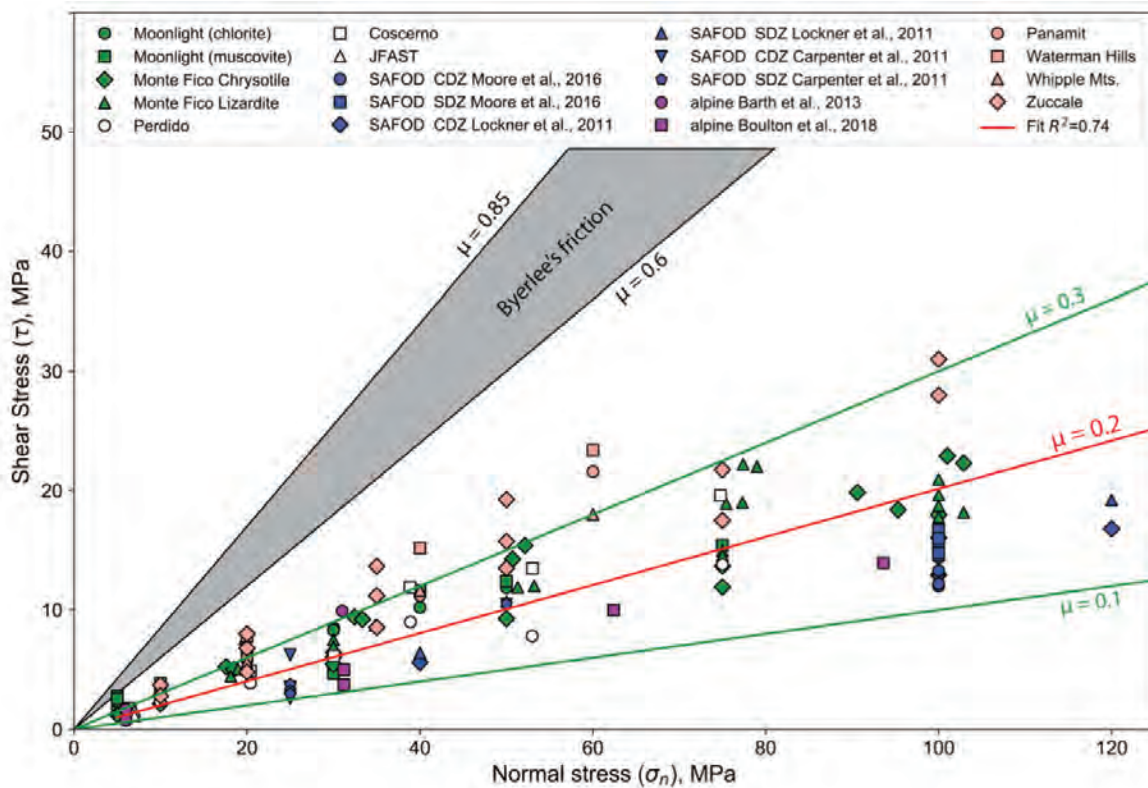
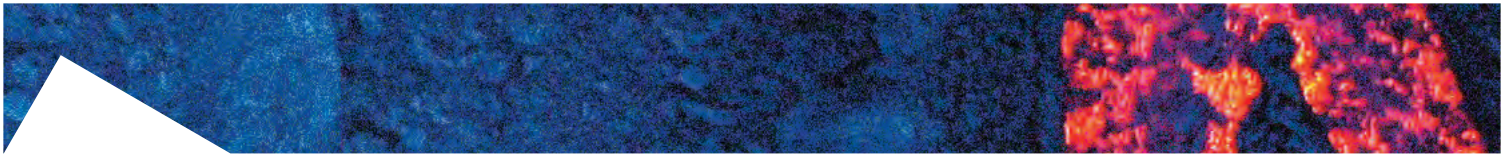
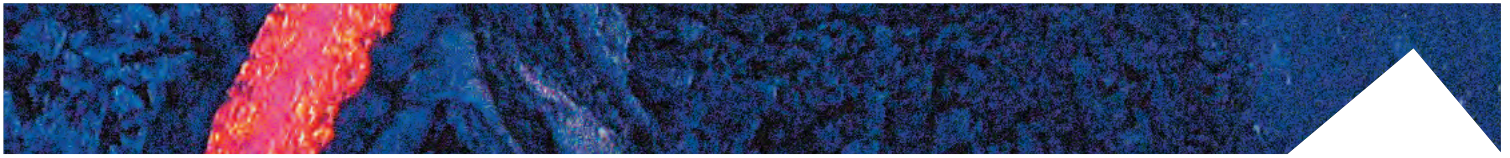


Fig. 1 | Frictional properties of natural phyllosilicate-rich faults.



Collectively, geological data and results from laboratory experiments provide strong supporting evidence for structural and frictional heterogeneities within crustal faults. In these structures, creep along weak and rate-strengthening fault patches can promote earthquake nucleation within adjacent strong and locked, rate-weakening portions. Some new frontiers on this research topic regard: 1) when and how a seismic rupture nucleating within a strong patch might propagate within a weak velocity strengthening fault portion, and 2) if creep and slow slip can be accurately detected within the earthquake preparatory phase and therefore represent a reliable earthquake precursor.



The role of shear fabric in controlling breakdown processes during laboratory slow slip events

Scuderi M.M., Tinti E., Cocco M., Collettini C.

In this study, we analyze slow-slip events obtained during laboratory experiments at the stability boundary ($k \sim k_c$) by matching the critical fault rheological stiffness (k_c) with a decreased machine stiffness (k). To discern the role of shear localization during fault weakening we simulated fault gouges using quartz powders and a mixture of anhydrite and do-

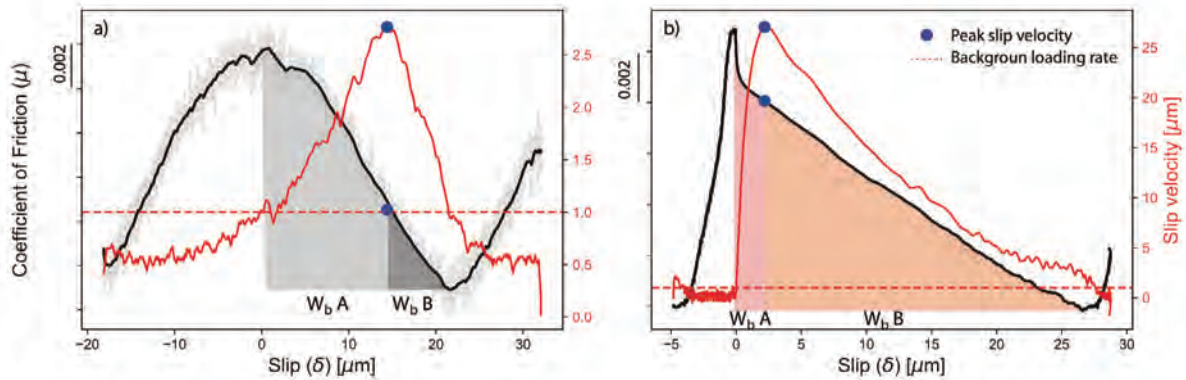
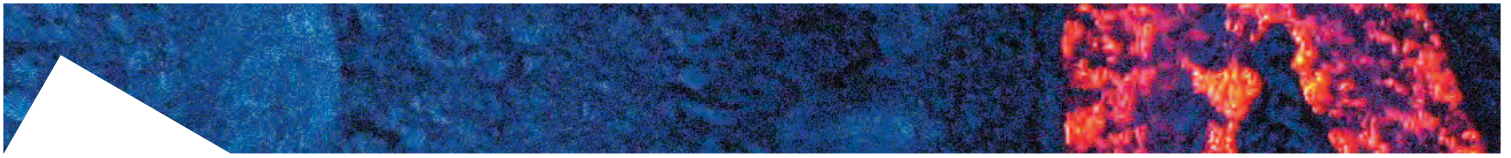


Fig. 1 | Traction evolution (black curves) and the slip velocity evolution (red curves) as a function of slip for quartz (left side) and anhydrite-dolomite mixtures (right side). The shaded area below each slip weakening curve represents the breakdown work, i.e., an estimate of the mechanical work absorbed on the fault plane during rupture. Breakdown work is an energy density (J/m^2). The total breakdown work in each panel is split in two portions (identified by different colours): the breakdown work absorbed before ($W_b A$) and after ($W_b B$) the occurrence of peak slip velocity (shown in the figure by the blue dots). For the Quartz a relevant portion of the mechanical work is absorbed before that slip velocity reaches its peak. For the anhydrite-dolomite mixtures, the larger portion of the mechanical work is absorbed after the slip velocity reaches its peak.

lomite, which have a strong rheological contrast. For both lithologies, slow-slip events have typical friction drop of ~ 0.01 and duration between 6s and 12s. During each event we observe that peak slip velocity is attained before reaching the minimum shear stress, and most of the slip velocity evolution is associated with the dynamic weakening phase.

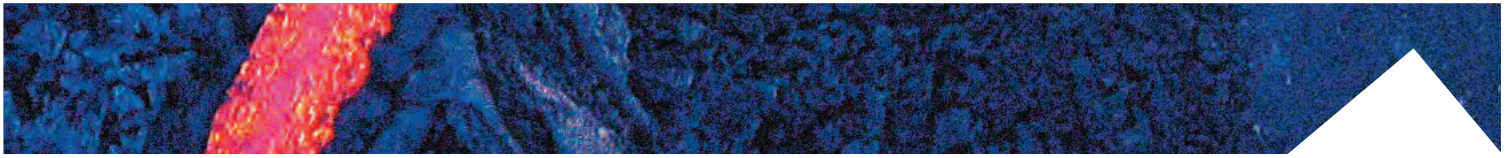
We document that the fault zone fabric controls the slip velocity function as well as the details of micro-mechanical deformation (i.e. dilation/compaction). For quartz gouge, shear deformation localizes along continuous and sharp ($\sim 1\mu\text{m}$ thick) shear planes resulting in a smooth slip velocity function (similar to a Gaussian) where a clear pre-seismic slip is easily detectable. In the anhydrite and dolomite mixture, shear localizes along thick boundary shear planes interconnected



by a P-foliation, resulting in a more distributed deformation, showing a Yoffe slip velocity having a short acceleration phase ($\sim 1s$) with no pre-seismic slip and a long deceleration.

The inferred breakdown work (seismological fracture energy) is very similar for both lithologies, but for quartz we observe a relevant portion of mechanical work absorbed before the main slip acceleration phase, probably due to the compaction within the bulk volume.

Our results confirm that the slip rate function contains the key dynamical information to characterize the evolution of dynamic traction. The retrieved differences in the slip velocity functions and mechanical work absorbed in dynamic weakening depend on the strain partitioning within the fault volume.

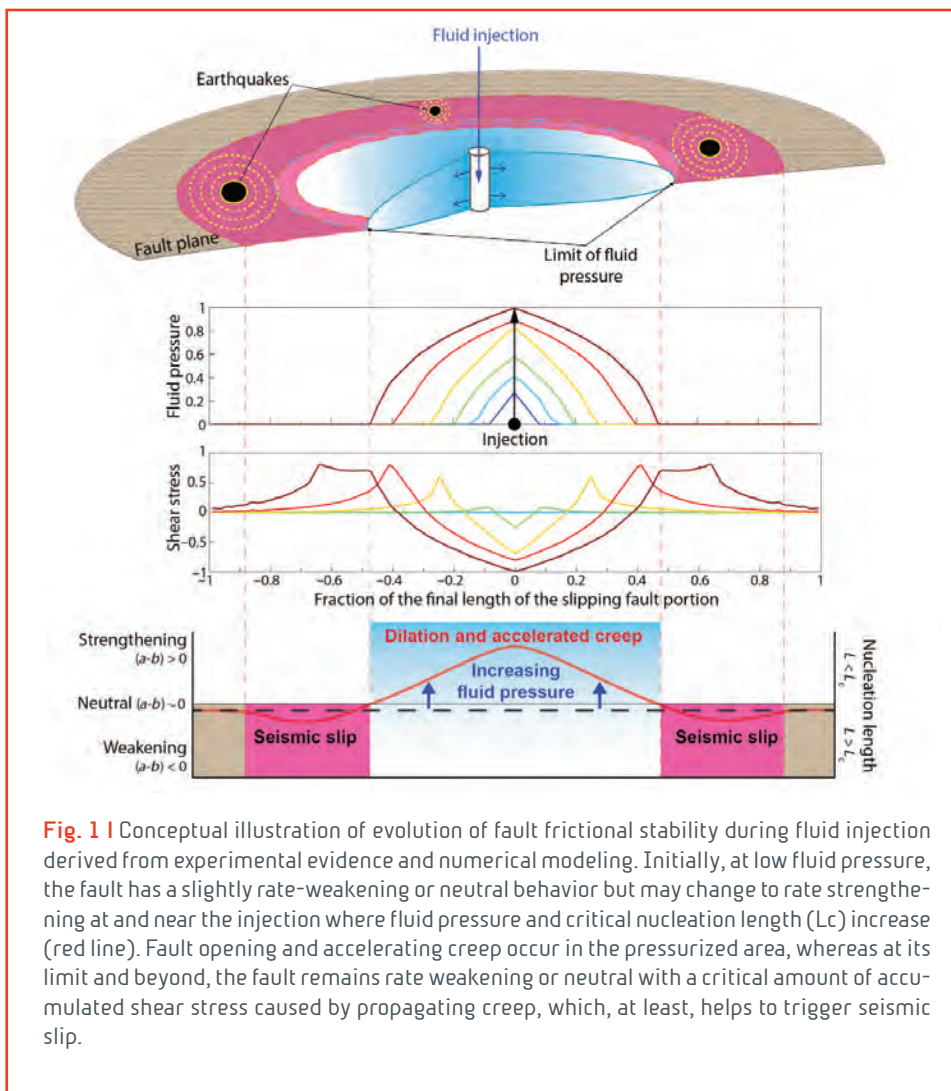


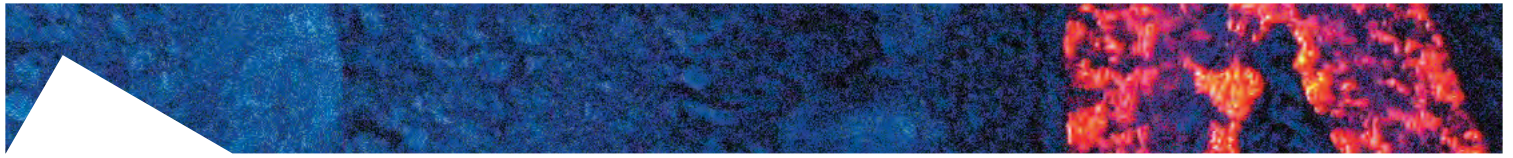
Stabilization of fault slip by fluid injection in the laboratory and in situ

Cappa F., Scuderi M.M., Collettini C., Guglielmi Y., Avouac J.P.

Faults can slip seismically or aseismically depending on their hydromechanical properties, which can be measured in the laboratory. Here, we demonstrate that fault slip induced by fluid injection in a natural fault at the decametric scale is quantitatively consistent with fault slip and frictional properties measured in the laboratory. The increase in fluid pressure first induces accelerating aseismic creep and fault opening. As the fluid pressure increases further, friction becomes

mainly rate strengthening, favoring aseismic slip. Our study reveals how coupling between fault slip and fluid flow promotes stable fault creep during fluid injection. Seismicity is most probably triggered indirectly by the fluid injection due to loading of nonpressurized fault patches by aseismic creep.





CO₂ storage in basalts: trembling up to North?

Giacomet P., Ruggieri R., Scuderi M., Spagnuolo E., Di Toro G., Collettini C.

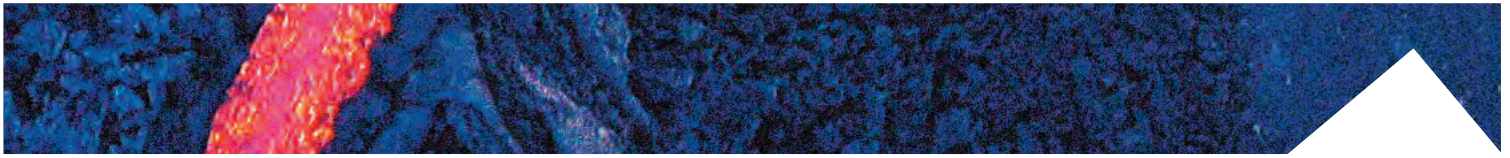
In the last decade, in-situ CO₂ storage into basaltic formations has been proposed as a viable and effective option for locally mitigating the carbon concentration in the atmosphere. The novelty of this method consists in the injection of fully dissolved CO₂ into both shallow and deep basaltic targets (e.g., CarbFix, CarbFix2 pilot projects - Iceland).

However, the well-known relationship between fluid injection and induced seismicity in several geo-energy contexts raised the burning necessity to conduct preliminary rock and fault mechanics studies before upscaling this CO₂ storage technique to the industrial scale, wherein large volumes of fluids are anticipated to be injected in the underground.

In this regard, we undertook friction experiments on basalts using BRAVA and SHIVA deformation machines, both installed at the HP-HT lab of INGV-Rome. Given their abundance in olivine and pyroxene minerals, i.e., the most reactive silicates that release divalent cations required to trap CO₂ into minerals, we selected basalts from Mt. Etna as a good analogue for CO₂ storage basaltic rocks. Our friction tests were specifically aimed at unravelling the frictional strength, stability, and healing properties of the two-fault end members that can be potentially found in geological storage and volcanic settings, i.e. simulated bare surfaces and fault gouge. The applied normal stress σ_n ranges between 5 to 30 MPa and from 5 to 10 MPa for fault gouge and bare surfaces, respectively.

To determine the frictional strength of faults, we deformed experimental faults at constant shear velocity of 10 $\mu\text{m/s}$ until a steady-state condition was attained, obtaining a frictional sliding coefficient μ of 0.59 – 0.78 regardless of experimental conditions. The peculiar geometry of the rotary-shear apparatus SHIVA allowed to assess the evolution of frictional strength of bare surfaces also at high displacements. As expected, faults exhibited slight slip hardening, with friction increasing from ~ 0.6 upon initial slip to ~ 0.7 after 56 mm sliding, in good agreement with previous studies conducted by Marone and Cox (1994) on gabbros, i.e. the equivalent intrusive of basalts.

Friction stability analysis consisted in a series of velocity step increases from 0.1 to 300 $\mu\text{m/s}$ with a constant displacement of 500 μm cumulated during each step. Velocity stepping tests point to a contrasting mechanical behavior between bare surfaces and synthetic fault gouge: while bare surfaces data illustrate a transition from rate-weakening at low sliding



velocity (V) to rate-strengthening behavior at $V > 100 \mu\text{m/s}$ with lack of dependency on the applied σ_n , synthetic fault gouge shows a negative trend of the friction rate parameter ($a-b$) with shear velocity at $\sigma_n > 5 \text{ MPa}$, that turns out to a velocity-weakening behavior at $V > 100 \mu\text{m/s}$. We attribute this different behavior to shear delocalization resulting from production of gouge with shearing in bare surfaces, and to shear localization accompanied by cataclasis and consequent grain size reduction along the Riedel R_1 and boundary B shears in fault gouges, as also testified by microstructural analysis (Figure 1).

To get insights on the healing properties of basalt faults, repeated sliding episodes of $500 \mu\text{m}$ slip at $V = 10 \mu\text{m/s}$ were followed by hold times of 30-100-300-1000-3000 s. The fast healing rates (β) retrieved from the entire compilation of slide-hold-slide experiments associated with the velocity weakening behavior of fault gouge, define high strength zones that potentially induce seismic slip. Conversely, velocity strengthening behavior of bare surfaces at relatively high V , suppresses dynamic frictional instabilities promoting aseismic creep. However, the above data represent just a first step into a better understanding of the frictional properties of basalts into geo-energy and volcanic environments, since the presence of phyllosilicate foliae resulting from hydrothermal fluids – basalt interaction, may modify the stability and healing properties observed in this study.

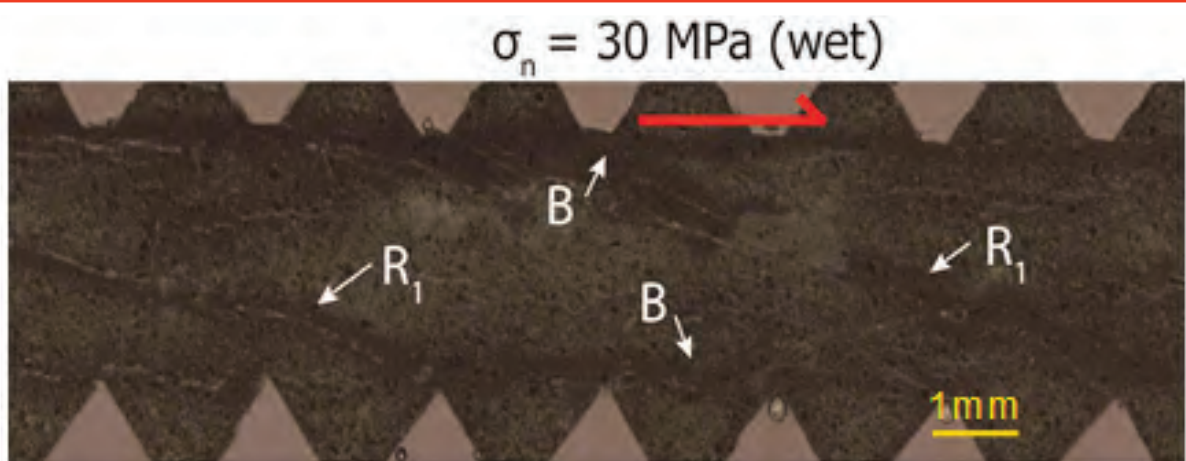
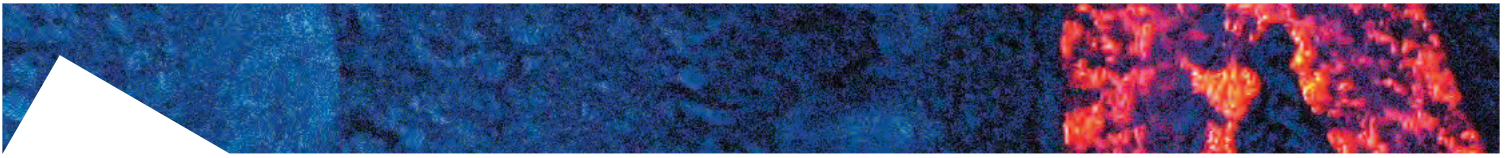


Fig. 1 | Microstructure of post-experimental synthetic fault gouge taken under the optical microscope: development of $\sim 200 \mu\text{m}$ thick R_1 and B shear bands subjected to extensive cataclasis and grain comminution.



Fault friction during simulated Yoffe functions

Harbord C., Spagnuolo E., Di Toro G.

In the past 2 decades we have come to understand that almost all geological materials are frictionally weak during high velocity slip ($>1\text{cm/s}$) expected during earthquakes on geologic faults. This knowledge has almost entirely been gathered by performing experiments using a ‘box-car’ velocity history i.e. with constant acceleration to a constant velocity followed by a constant deceleration to zero velocity. Box-car slip histories are probably not representative of natural fault slip behaviour, where elastodynamic models and source time functions suggest complex fault slip histories. In low velocity friction experiments prior sliding history plays an important role in fault strength with important implications for the nucleation of earthquakes. Here we investigated the role of varying slip histories during high velocity fault sliding, utilising a Yoffe function (elastodynamic solution to the velocity field of a propagating crack) with varying initial accele-

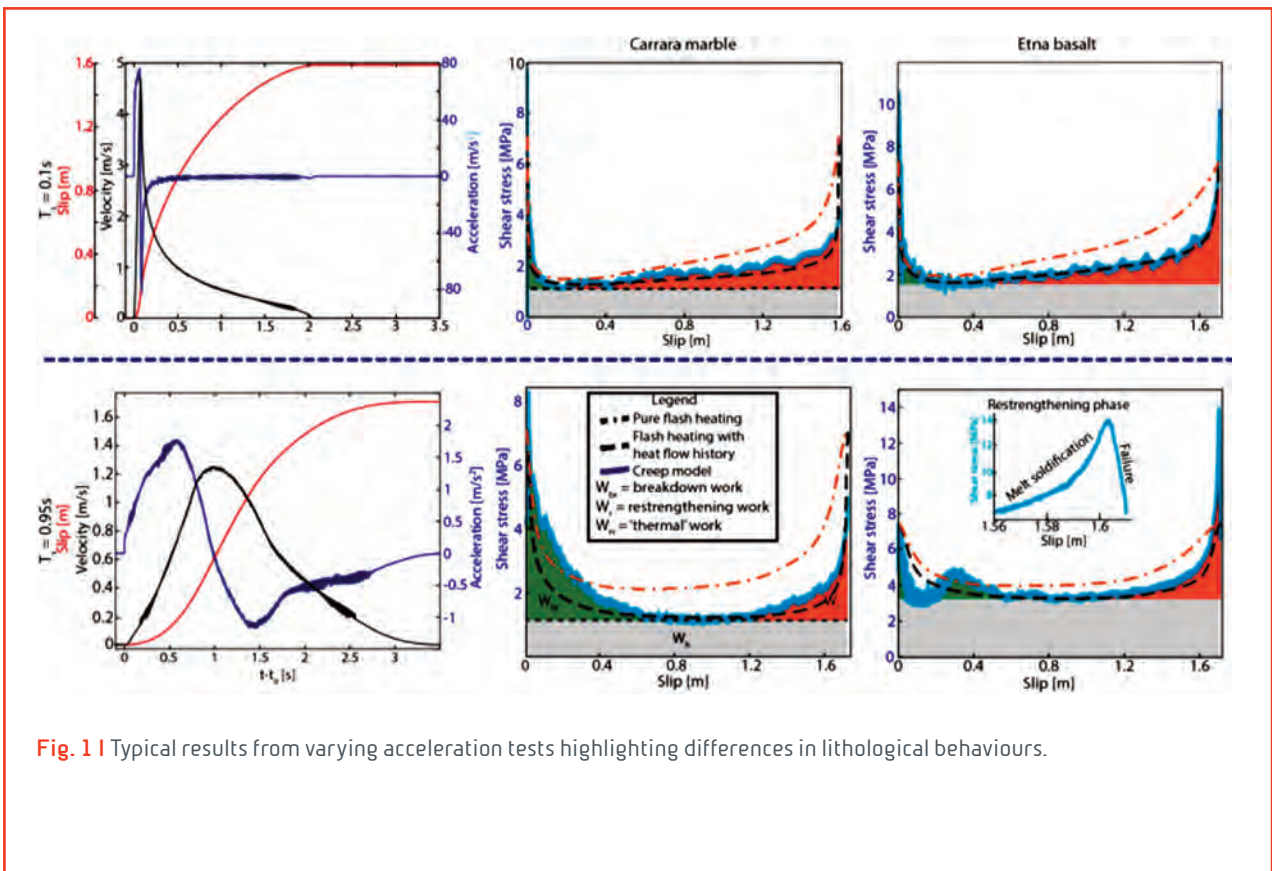
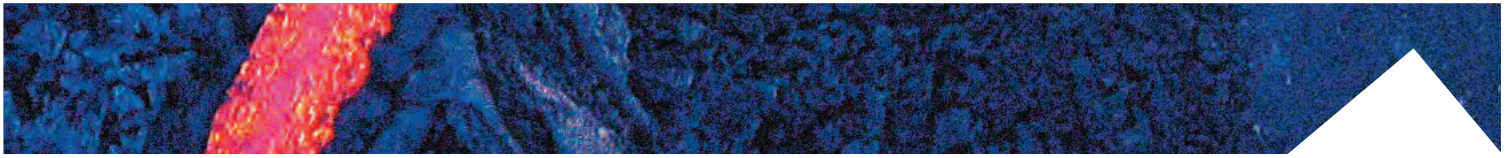
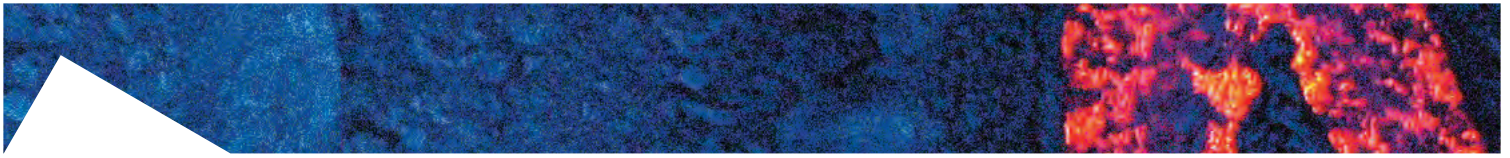


Fig. 1 | Typical results from varying acceleration tests highlighting differences in lithological behaviours.

ration to simulate M0 6 earthquakes in Etna Basalt and Carrara Marble. To perform these tests several developments were made to the control routine of SHIVA involving the integration of the motor control in the data acquisition program.



Results show that the breakdown work scales with the initial acceleration rate of the fault, and faster acceleration results in a shorter weakening distance scaling as τ^{-1} . The effects of prior sliding history become more pronounced as slip progresses, and the strength preceding deceleration is well explained by a model considering the heat flow history of the fault. Restrengthening behaviour is more complex and shows a lithological dependence, whereby faults lubricated by melt develop cohesion become strong with friction coefficients in excess of 1. Alternatively in Carrara strength remains lower than predicted by models. The results demonstrate that weakening laws are generally applicable to variable slip histories, and show that heat flow is fundamental to high velocity frictional behaviour. However more systematic work is required to understand the nature of restrengthening behaviour and its consequences on repeating earthquakes. For natural earthquakes this shows that faster ruptures have lower breakdown work, consistent with linear elastic fracture mechanics and natural observations.



The physical properties module (PPM), development, calibration and testing

Harbord C., Tisato N., Spagnuolo E., Di Toro G.

As seismic waves propagate through the earth's crust they are attenuated, this is either by means of scattering or the intrinsic viscoelastic response of the deforming material. Since attenuation is dependent on the material properties of the deforming rocks it can be used as a geophysical tool to image the earth. The interaction of attenuation with geologic

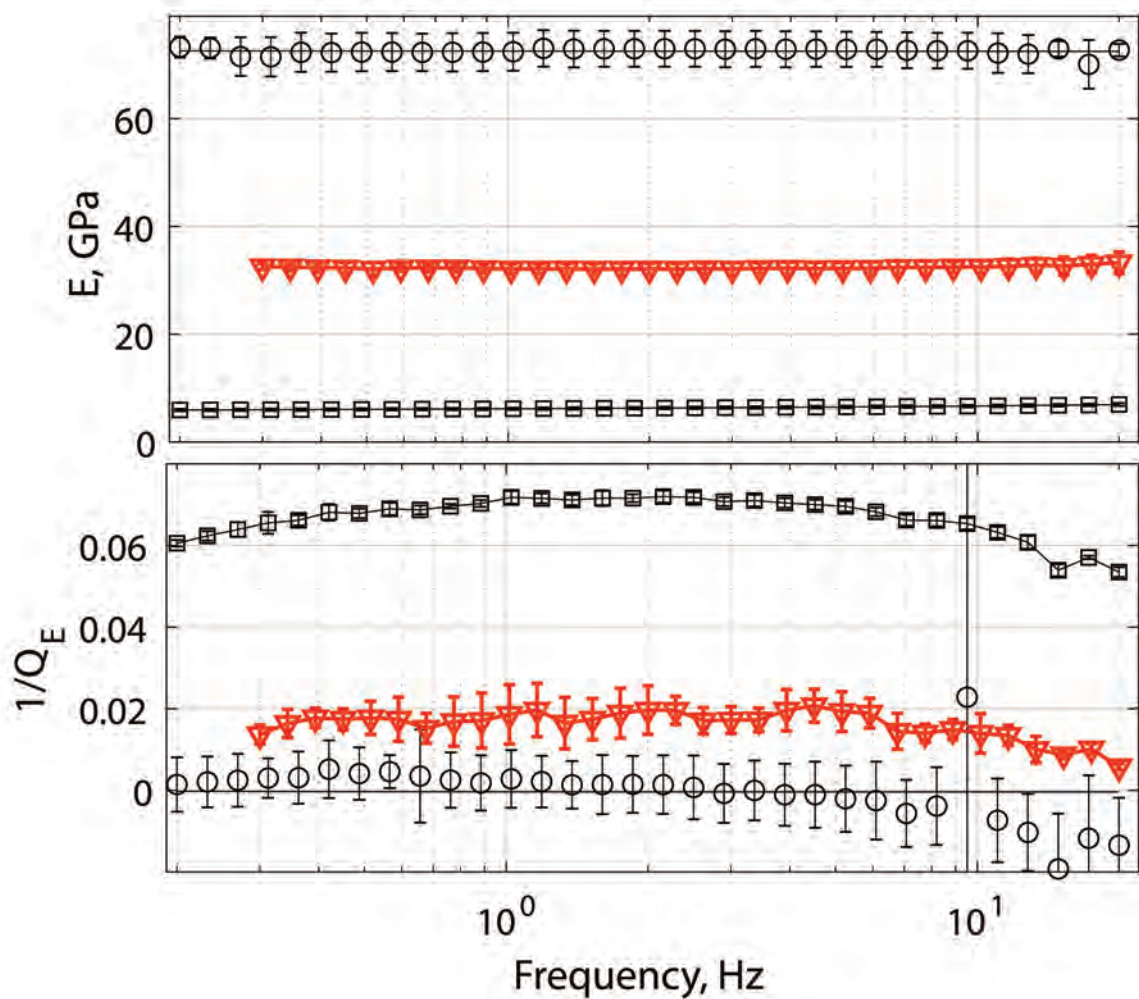
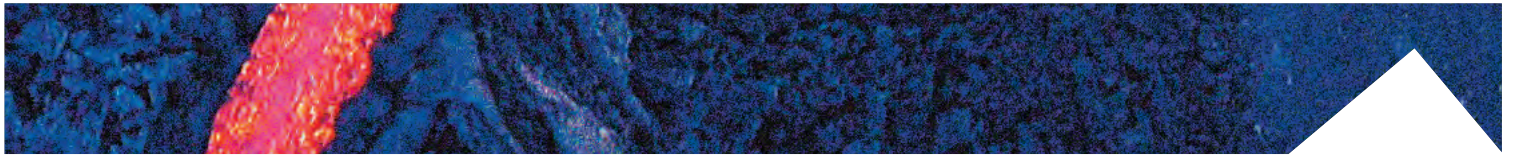
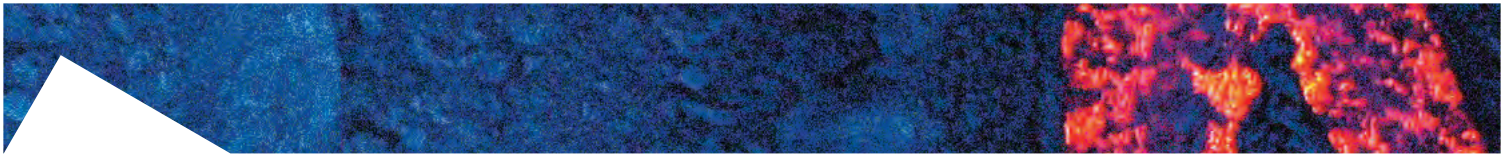


Fig. 1 | Calibration measurements of frequency dependent attenuation in PMMA ($Q^{-1} \approx 0.04-0.07$), Aluminium ($Q^{-1} < 0.005$), showing agreement with previous studies (e.g. Tisato and Madonna, 2012). Calibration of E was obtained by assuming E of Aluminium = 70 GPa. Signal phases were affected by a constant phase of -0.05 rad probably introduced by the sensor electronics. Sensors have been recently factory-recalibrated to overcome such issues.

faults is poorly understood and may represent a chance to remotely investigate the state of a fault during the seismic cycle. In order to investigate attenuation we have developed a new 'Physical properties module' (PPM), designed to



measure the intrinsic attenuation of deformed faults at seismic frequencies (0.01-100 Hz) in SHIVA. The bespoke module consists of a high resolution load cell (accuracy $<1\text{N}$) and strain gauge (accuracy $\sim 1\text{n}\epsilon$) positioned in series with a large piezo-crystal motor which oscillates the rock sample across the frequency range. A MATLAB based program has been developed to control and acquire data during frequency sweeps which is fully interactive with live data processing capabilities, provided the user with real time information on the experiment progress. Full calibration of the unit has been undertaken, including electronic hardware timing tests, load cell calibration and the utilisation of known standard materials (Aluminium and PMMA) with good agreement between results from the module and published literature values. In the near future the module will be used to investigate attenuation at varying degrees of accumulated shear strain and fault development during progressive fault slip in SHIVA.



Pressure-solution creep leads to strain hardening in mylonitic amphibolites: examples from the Ben Hope Sill, Moine Supergroup, NW Scotland

Pozzi G., Tesei T., Schorn S., Bowen L., Holdsworth R.E.

Amphibolites are typically produced during regional metamorphism of mafic-ultramafic rocks in the hydrated middle and lower crust. Despite their abundance, their rheology is somewhat enigmatic, especially when compared to better-known quartzo-feldspathic and phyllosilicate-rich rocks.

We investigated the ductile deformation of amphibolites associated with the Ben Hope Sill in Port Vasgo (NW Scotland) combining field and microstructural observations (see Figure 1, thin sections) with Electron Backscattered Diffraction analysis (at the department of physics, Durham, UK; see Figure 1, pole Figures hbl) and Micro-Probe chemical analysis (at the INGV, Rome, IT).

The Ben Hope Sill is a metamorphosed mafic body embedded within the Moine metasediments that experienced tight to isoclinal sheath folding and ductile Caledonian thrusting (local D2 event) under lower amphibolite-upper greenschist

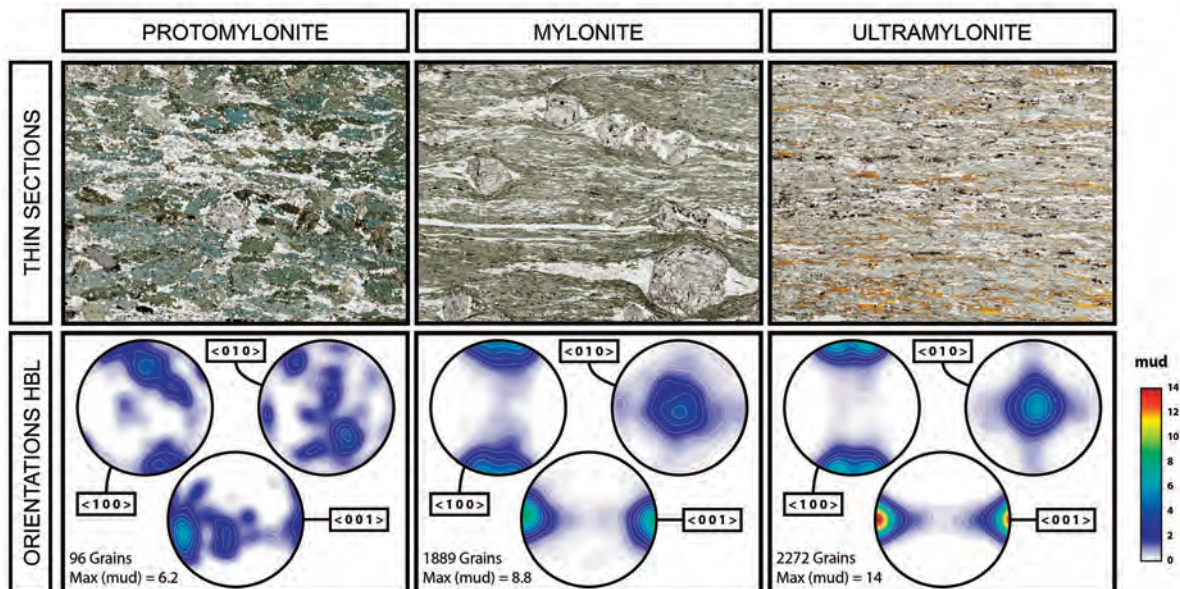
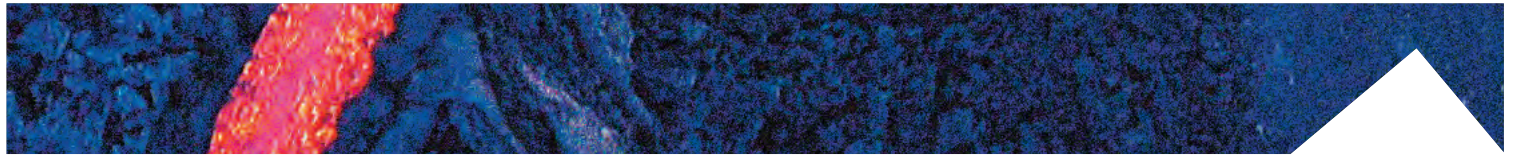
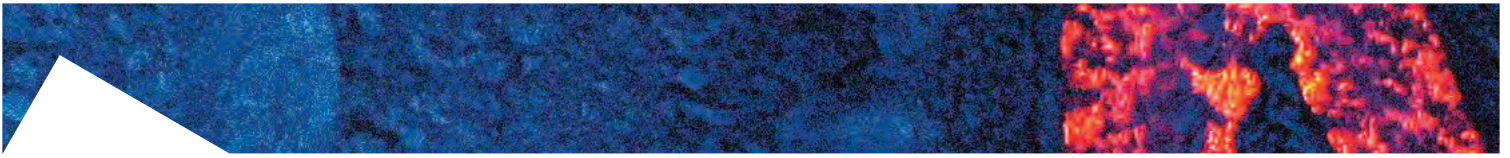


Fig. 1 | Progressive deformation stages in amphibolite rocks (from protomylonite, low strain, to ultramylonite, high strain). Thin sections: plane polarized light imaging of amphibolite thin sections Orientations hbl: Pole figures obtained from crystallographic analysis of hornblende crystals (SEM electron back-scattered diffraction).



facies conditions. Pervasive ESE mineral lineations and widespread shear criteria (S-C fabrics, asymmetric pressure shadows) consistently indicate top-to-the-WNW transport during D2 mylonitization. At the outcrop scale, the sill constitutes a series of spatially associated 0-10 m thick layers displaying progressive strain localization, from pockets of almost undeformed lenses (protomylonite) to pervasively mylonitized horizons (ultramylonite). The undeformed lenses are characterized by massive, coarse-grained amphibolites (hbl+qtz+plg+grt) in which static growth of poikiloblastic hornblende and almandine garnet, hosts a fabric of an earlier (D1) event. Within amphibolite mylonites formed during D2 shearing we infer progressive pressure-solution of quartz, plagioclase and amphibole demonstrated by: i) the decrease in modal abundance of plg and qtz and increase/recrystallization of hbl; ii) the precipitation of hbl in pressure shadows and iii) the growth of Ca-rich rims of porphyroblastic garnet. Moreover, pockets of (locally sourced) overpressured fluids are represented by 1-30 cm veins of quartz (Cal) that cross cut the shear bands and are locally highly strained into sheath folds. Thin horizons, typically observed at the edge of the deformed sill, show enrichment in biotite at the expense of the amphiboles and progressive brittle fragmentation of garnets (Figure 1, ultramylonite). Hornblende crystals show progressive strengthening of their crystal preferred orientation from the less deformed domains to the ultramylonite (pole figures hbl).

Collectively, these observations suggest that initial D2 strain softening and localization within the amphibolites is guided by pressure solution. However, strain softening is limited by the sluggish kinetics of hornblende pressure-solution. Therefore, enrichment of amphiboles above a critical volumetric threshold leads to a substantial hardening of the mylonites causing, together with local fluid overpressure, brittle failure and ingress of metasomatic fluids. We emphasize the importance of fluids in supplying and removing chemical species during deformation, leading to complex brittle-viscous deformation cycles in amphibolitic rocks under middle crustal conditions.



Viscosity measurements on extracted bitumen of the Majella reservoir (Central Italy)

Ruggieri R., Trippetta F., Del Bello E.

Since physical properties of viscosity fluid, as bitumen, are strongly temperature dependent, thus we carried out viscosity measurements in order to investigate the rheology property of bitumen. This bitumen was extracted by HCl dissolution of hosting carbonate rock, collected in the northern flank of the Majella (Central Italy), where several oil seeps of asphalts and bitumen found at surface, mainly associated to the Bolognano Formation. Viscosity measurements were determined at temperature of 90°C and 110°C using a rheometer AntonPaar Physica MCR301, equipped with parallel-plate geometry setup. This geometry is characterized by two plates (~ 2 mm diameter): the lower plate is fixed and heated at the test temperature, while the upper plate can rotate. Since the investigated bitumen was in a solid state, before of the viscosity

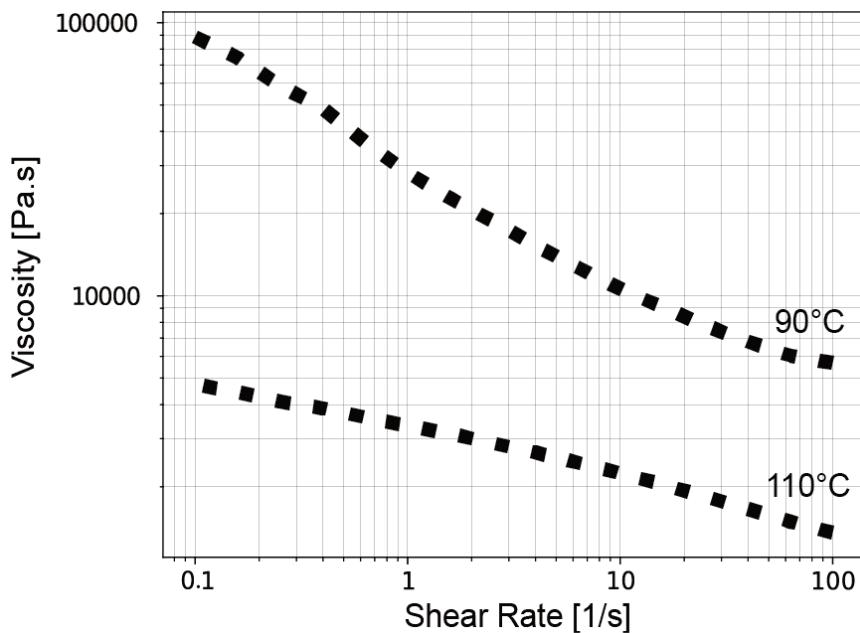
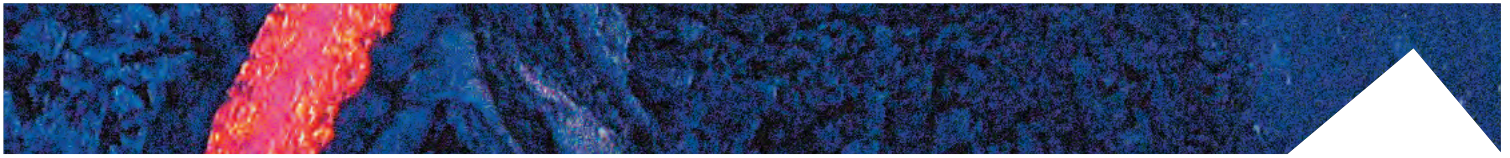


Fig. 1 | Plot of viscosity measurements, conducted on extracted bitumen, as a function of shear rate for two investigated temperatures (90° C and 110° C).

measurement, we have heated the bitumen sample at the same temperature at which viscosity was measured. After ten minutes, the heated bitumen sample was removed from the oven and was sandwiched in between the parallel plates. Once the lower plate had reached the test temperature, a rotational speed was

applied, and the viscosity measurements were performed in a wide range of the shear rates from 0.1 to 100s⁻¹. As expected, viscosity measurements depict a strong dependence with temperature. Basically, an increasing temperature from 90°C to 110°C causes a reduction of one order of viscosity magnitude, from 8.89 × 10⁴ to 4.74 × 10³Pa·s at the initial shear rate of 0.1 s⁻¹ (Figure 1).



Earthquake reactivation and seismic slip in presence of viscous fluids

Cornelio C., Passelegue F., Spagnuolo E., Di Toro G., Violay M.

One of the most alarming recent findings in solid earth sciences is the worldwide exponential increase of man-induced seismicity. The latter is due to engineering operations in deep reservoirs for hydrocarbon production, wastewater and CO₂ storages and exploitation of geothermal resources which result in the reactivation of faults hosted in the reservoirs. While the reactivation of faults due to fluid pressure has been extensively studied, the influence of fluid properties including its viscosity has been overlooked, even if the viscosity of injected fluids spans from the one of water to that of honey. In this study, we aim at understanding the influence of fluids viscosity on seismic slip initiation and propagation. We present more than 40 friction experiments performed in the rotary shear apparatus SHIVA (INGV), at effective normal stress up to 10 MPa on experimental faults of granite. Four different fluid viscosities were tested: water ($\eta \sim 1$ mPa s) and three mixtures of water with glycerol concentrations of 60%wt., 15%wt. and 0.1%wt. ($\eta = 10.8$, 109.2 and 1226.6 MPa s) at fluid pressure P_f of 2.7 MPa and under drained conditions.

To study the earthquake reactivation phase, we incremented stepwise the shear stress on the experimental fault up to the initiation of fault slip. Instead, to study the seismic slip phase, we performed velocity-controlled experiments imposing

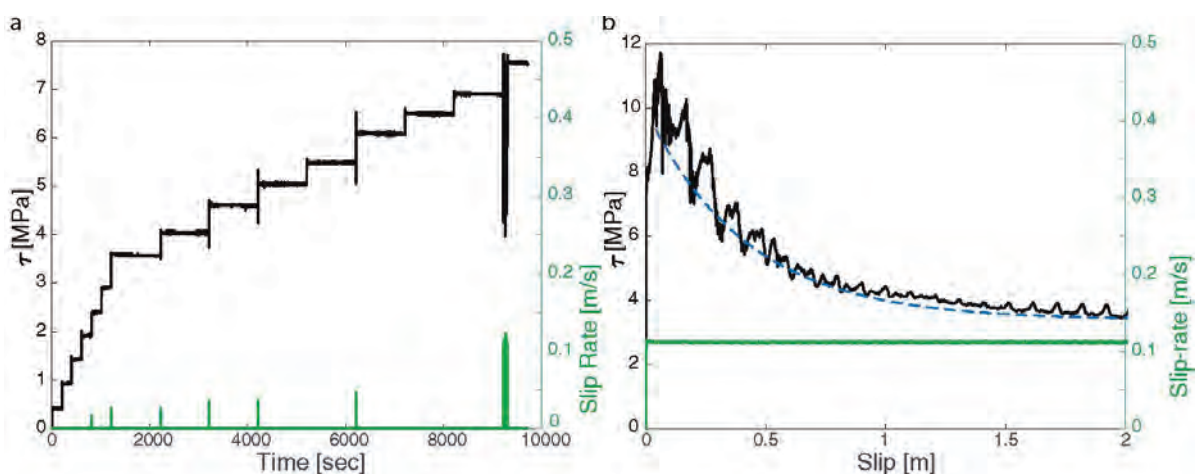
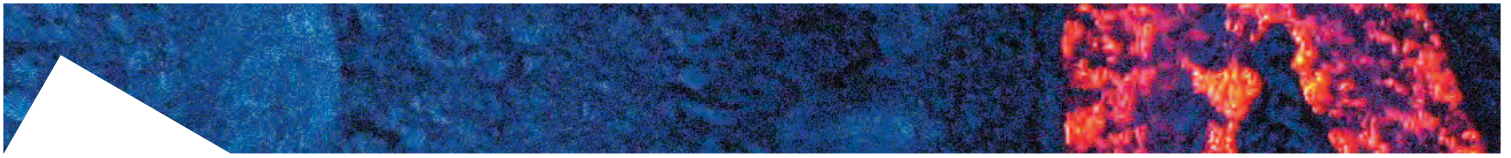


Fig. 1 | Experimental curve results a) Evolution of shear stress and slip rate versus time in an experiment performed under torque control mode to investigate earthquake nucleation. Experiment performed in presence of mixture 40% water 60% gly. b) Evolution of shear stress and slip rate versus slip in an experiment performed under velocity control mode to investigate earthquake propagation. Experiment performed in presence of mixture 40% water 60% gly.



slip-rates ranging from 10 $\mu\text{m/s}$ to 1 m/s and recording the evolution of the dynamic fault strength with slip.

Mechanical data show that fluid viscosity does not influence the reactivation of the fault, which occurs at a friction coefficient of ~ 0.6 in all conditions tested, in agreement with the Byerlee's law. Moreover, the experiments performed under room-humidity conditions show a phase of precursory activity before slip acceleration up to seismic slip rates ($> 1 \text{ cm/s}$) that is absent in the experiments performed in the presence of fluids.

During seismic slip, the role of fluid viscosity is even more important. Indeed, fluid viscosity affected the fault weakening

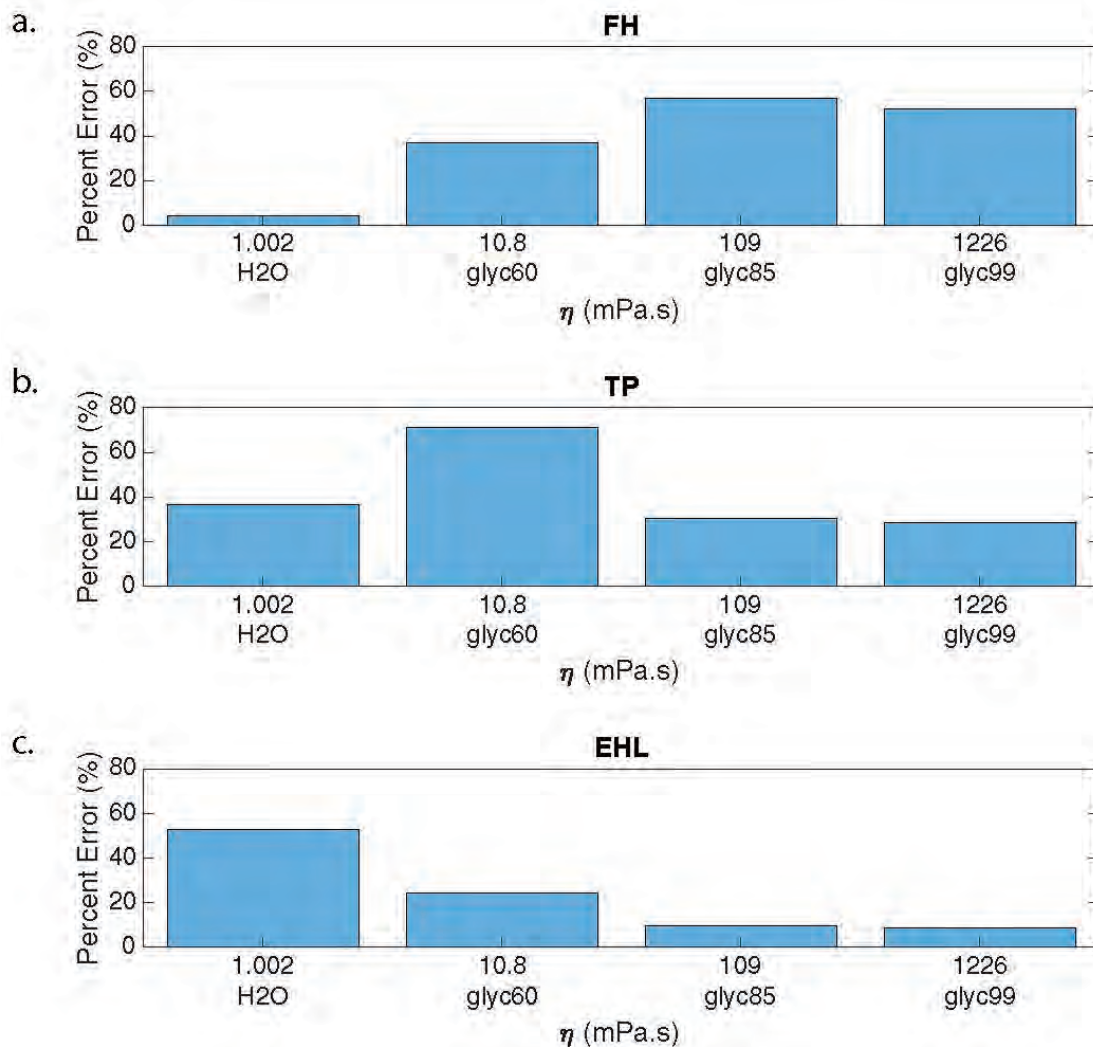
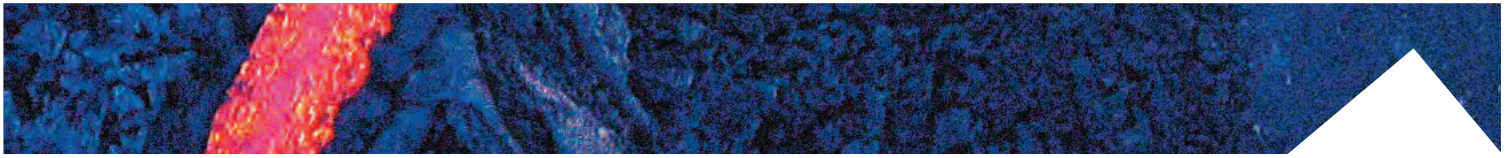
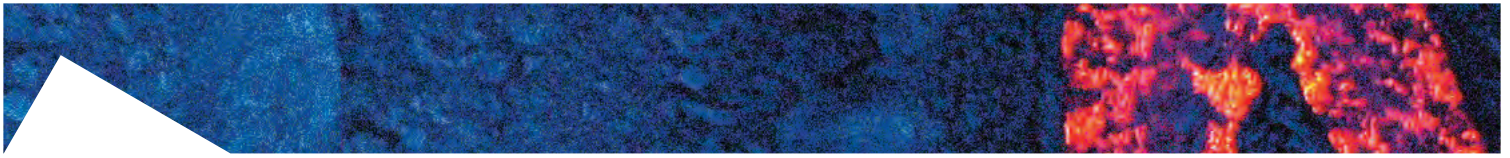


Fig. 2 | Percent error between the measured minimum shear stress and the estimated one for (a) Flash heating (FH), (b) Thermal pressurization (TP), and (c) elasto hydrodynamics (EHL). According to this analysis, FH occurred only in the experiments performed with 100% distilled water, and EHL in the experiments performed with glycerol. Instead, modelling suggests that TP was never activated in the experiments.



mechanism: flash-heating was the dominant weakening mechanism in room-humidity and water-saturated conditions, whereas the presence of more viscous fluids favored the activation of elasto-hydrodynamic lubrication, with implications on dynamic fault strength, and earthquake energy budgets.



Controlling factors on the shallow co-seismic slip at the Sumatra subduction zone megathrust

Spagnuolo E, Vannucchi P., Aretusini S., Nielsen S., Di Toro G.

Rupture models of the 2004 Mw 9.2 Sumatra-Andaman EQ imply shallow co-seismic slip with suggestions that slip could have even extended close to the trench particularly along the southern portion of the Sumatran margin. Geophysical imaging of the Sumatran accretionary prism suggested that the shallow plate boundary interface propagates through sediments deposited in the Warton Basin near the base of the Bengal-Nicobar fan and even in pre-fan layers. However, imaging was not able to identify the precise location of the frontal megathrust, and three “candidates” for this sediment horizon were proposed in the input section. IODP Exp. 362 sampled these layers to investigate the characteristics of the input material and the factors controlling shallow seismogenic slip potential. We conducted

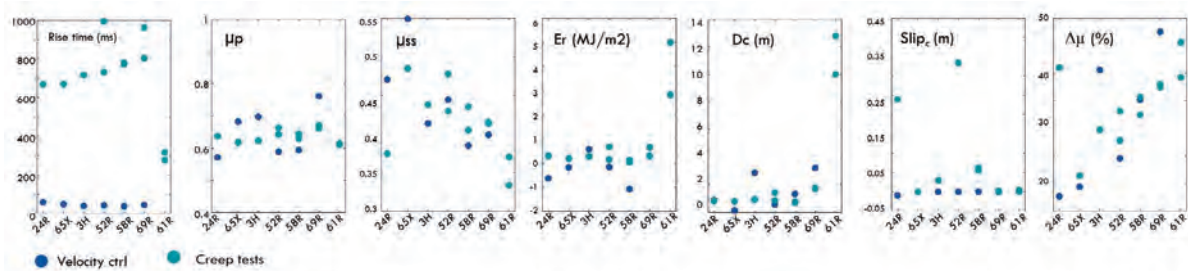
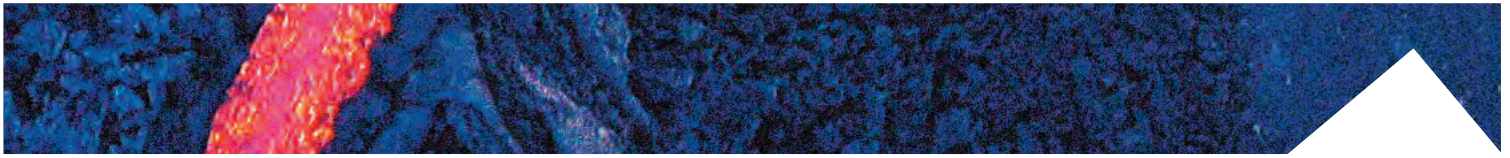


Fig. 1 | The peak of friction is large for all the lithologies (~ 0.65). 24R and 52R are more stable and cumulate a high slip before the MI. 24R and 52R also coincides with the layer that possibly host frontal decollement from seismic. Frictional instabilities through 61R accelerates faster. 61R also records the largest E_r . D_c and stress drop. 69R, 65X, 61R behave like locked fault patches. They can cumulate high stress and release it all at once. 24R, 52R, 58R, 3H behave like creeping patches and release the stress by creeping but also through small fast (> 0.1 m/s) events. Thus, though the high velocity weakening behavior seems similar for all fault materials the way the layers cumulate and adjust the shear stress is different resulting in a different E_r and in a different fault stability. Layers 69R, 65X, 61R are prone to larger strain energies E and capable of accumulating the elastic strain required to produce a “locked” patch on a plate interface at shallow depths but elastic strain must not be released by adjacent weaker lithological units.

an innovative set of experiments – “creep tests” – where shear stress is increased step-wise until the onset of accelerated fault slip. Unlike the usual creep tests, this novel technique allows us to observe a very broad spectrum of slip behaviors that spontaneously occur upon faulting, from aseismic creep to accelerated slip at seismic slip rates (1 m/s). Creep tests will also avoid forcing dynamic weakening as a consequence of the seismic slip rate – i.e. at 1 m/s all materials tend to have a remarkable slip weakening behavior. These tests reveal that although the dynamic



weakening behavior seems similar for all the “candidate” fault materials, the way in which they accumulate and adjust their shear stress differs one from the other, resulting in two endmember fault stability characteristics, explained using the energy budget for rupture propagation. Specifically, we identified a pre-fan layer that can accumulate high stress and release it all at once through a fast (>1 m/s) event, behaving like a locked fault patch. Most of the other layers, although still able to accumulate stress, release elastic shear stress both by creeping and also by short-lasting fast (> 0.1 m/s) events, behaving like creeping patches which can accelerate up to seismic slip rates. These conclusions hold if elastic strain is not released by adjacent weaker lithological units. Deformation features in the lower plate as well as in the prism, and plate flexural bending can all exert a key role in building up elastic stress favoring fault propagation – as well as fault nucleation – in the candidate decollement layer.

Improvements of the axial load and control on the Slow to High Velocity Apparatus (SHIVA)

Di Stefano G., Aretusini S., Harbord C., Spagnuolo E., Di Toro G.

SHIVA (Slow to High Velocity Apparatus) is an experimental electro-mechanical apparatus, developed to conduct rock mechanics experiments and reproduce the interaction between stressed fault rock samples in the laboratory. These experiments are important to better understand the physics of earthquakes under different boundary conditions.

Used for several years in the HP-HT laboratory, SHIVA is a complex technological apparatus in continuous evolution: several subsystems contribute to the functioning of the apparatus and, in recent years, some of these have been improved and updated in order to allow researchers engaged in the experiments to plan and design new-concept experiments to make it possible to study phenomena related to the nucleation, propagation and arrest phase of earthquakes.

To increase and stabilize the normal load in SHIVA, a significant update was performed in 2019. The old mechanical horizontal load system, based on a pneumatic actuator (piston) and an amplifying lever (factor 2.7) capable of producing an axial thrust of 50kN, has been dismantled and replaced with a new electromechanical system (Figure 1).

The old pneumatic system was controlled by an industrial type digital pressure regulator, with a range 0-9 bar, a re-

solution of 0.02bar and a response of 0.2s for a step equal to 50% of the full scale value. In the past the regulator controlled the air pressure in the pressurization line (not in the actuator chamber directly) keeping it equal to the reference value (set-point), set in the device via the computer of SHIVA. The force generated by the piston, axial load on the rock samples, was measured by a load cell in line with the sample axis and was not utilised as a feedback parameter. The signal of the load

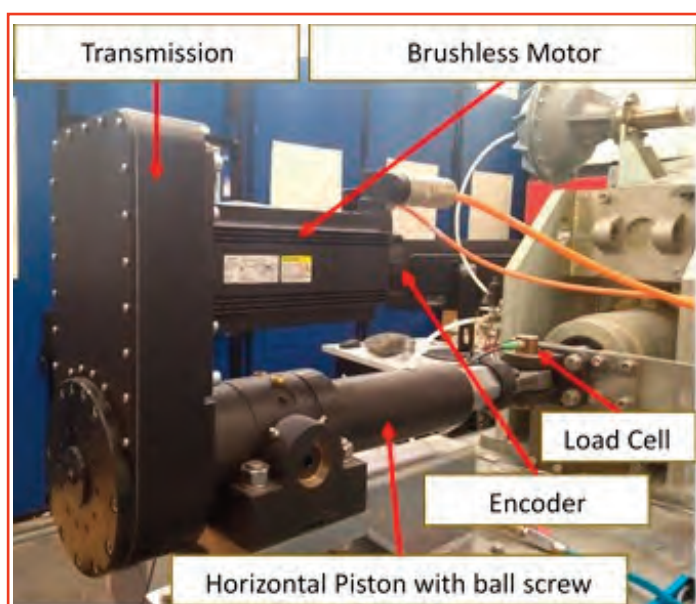
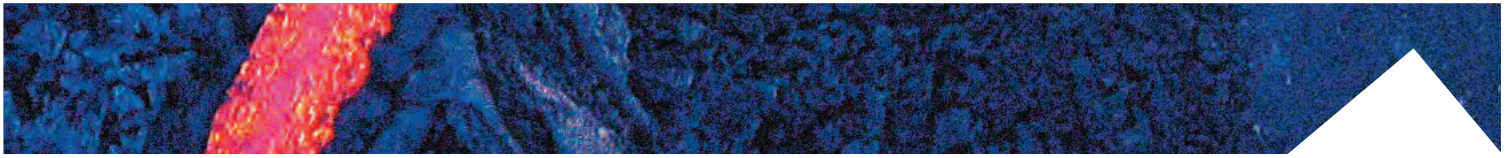


Fig. 1 | Newly installed electro-mechanical system to generate the axial load on SHIVA.



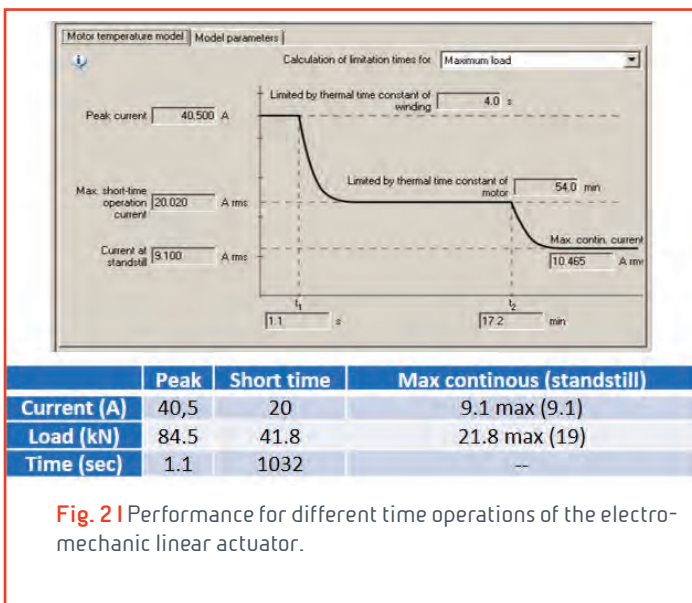
(process variable), acquired by the load cell, was not used to modulate the reference value (set-point) of the pressure regulator and therefore to reach a desired value of the axial load on the rock samples. This type of control (open-loop) on the axial thrust did not take into account any load changes in the air pressurized system and subsequently axial load oscillations on the rock sample were often encountered, reducing the reproducibility of experimental data. The new actuator (Figure 1) is comprised of a 3-phase Brushless motor (Rexroth, type: MSK071D-0300), a transmission unit and a screw piston with recirculating balls (Rexroth, type EMC-105-HD-1) that pushes on the samples. This system is capable of generating a load of 84kN for about 1s.

The new electromechanical system is powered by a configurable driver (IndraDrive HCS01), which also assumes the function of regulator and/or controller, if inserted in a closed loop configuration. The drive has PID functionality (Proportional, Integral and Derivative) which can be configured by a PC through an Ethernet network connection based on industrial protocols (EtherCat, CANBus) and to enter other parameters during a control process.

The new electro-mechanical assembly is installed on the device using a mechanical interface. A new load cell, Batarow model MB671, is installed between the piston and the stationary load column. The output signal (voltage \pm 10V with \pm 0.2V F.S.) is connected into one channel of the NI9205 module installed in the cRIO chassis in the electronic box of SHIVA.

Utilising the SHIVA computer and the IndraWorks application it is possible to control the motor speed or torque (thrust

of the piston) with open loop control. For an automatic control of the axial thrust, a closed loop with standard numeric regulator (PID type) has been implemented on the FPGA of the cRIO as shown in the Figure 3. In this way it is possible to control the axial load so that it can assume desired values or profiles, using the axial load signal as feedback. As showed in the picture, the thrust signal is digitized and compared with



a desired load value. The numerical value of the error (Err) is processed by the PID and converted to analog signal applied to the Drive; the drive acts directly on the speed of the motor (or its torque) so that the load assumes the desired value, at a switching frequency of 16kHz.

With the new system the response of the axial thrust applied to the rock sample has been improved; using an engine cooling system we can reach load values higher than the 50kN of the pneumatic system. The next step will be to install a "SoftMotion" module of the new LabVIEW package in order to be able to control the electro-mechanical actuator directly via Ethernet and using the regulation system inside the IndraDrive.

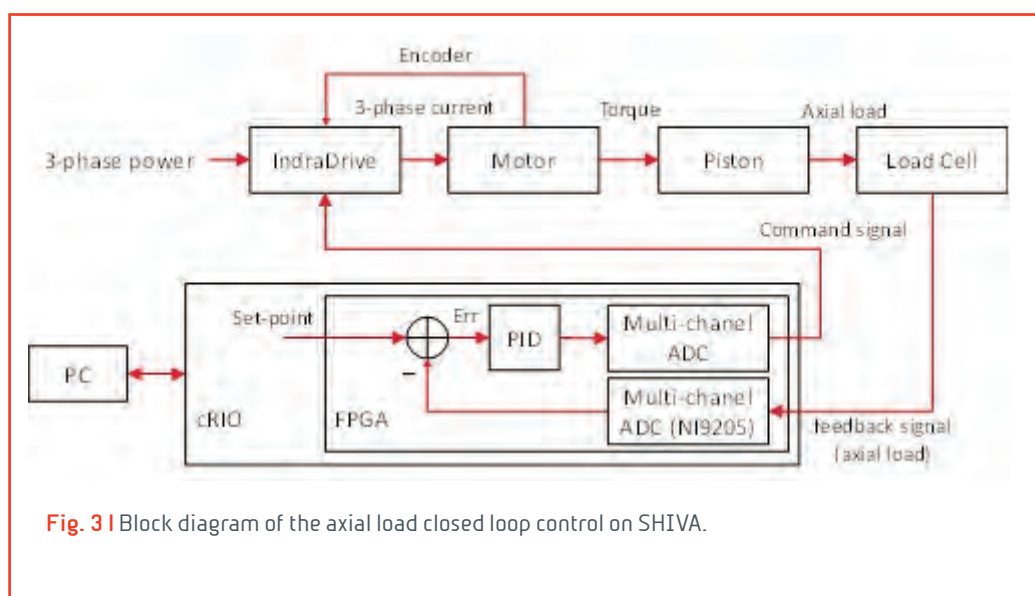
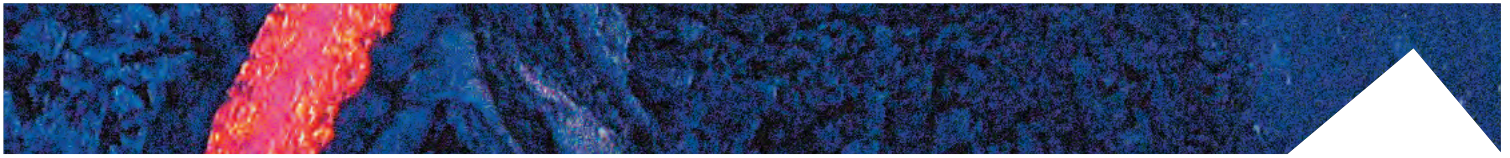


Fig. 3 | Block diagram of the axial load closed loop control on SHIVA.



8.3 TECHNOLOGY

Audio amplifier

Romeo G., Spinelli G.

Three years ago LNTS built and patented (Italian patent application n. 102015000071865) an audio amplifier.

The idea behind this amplifier is to give to the users the possibility to control the transducer's damping factor, in the same way a seismologist can control the damping factor of a geophone. This allows reaching a quality in sound reproduction unreachable without the perfect coupling amplifier-loudspeaker.

The prototype was exhibited during the National Geographic Science Festival in Rome (2019 April 8-14), in a room equipped with a demo desk showing the INGV's amplifier theory of operation (Figure 1, top) and with a listening station (Figure 1, bottom) where the amplifier prototype was connected to two hi-end loudspeakers allowing the public to enjoy few minutes of hi quality music.

The Auditorium show made the amplifier to appear on thematic forums on the web (<http://www.hifi-forumlibero.it/phpBB3/viewtopic.php?t=8545>, <https://melius.club/topic/295648-alta-fedelt%C3%A0-e-sismo->

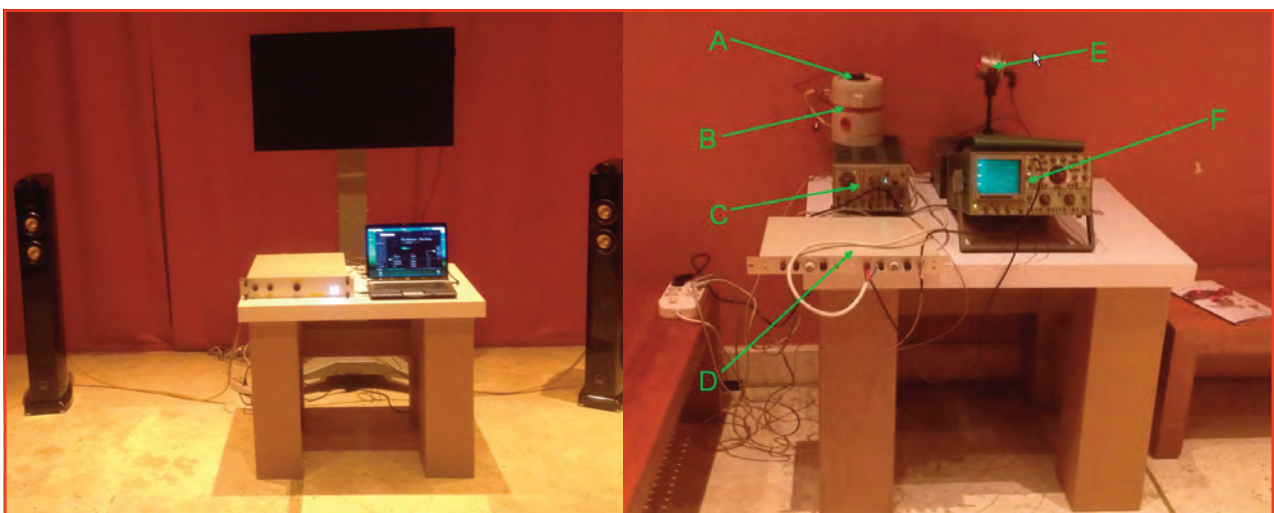
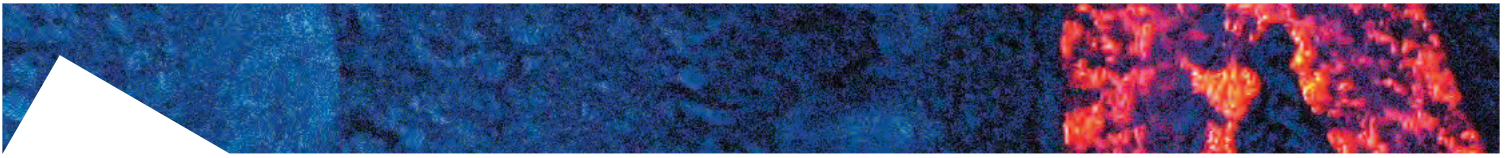


Fig. 1 | TOP: the listening station equipped with the INGV's amplifier connected to a couple of Mistral BOW-A2 loudspeakers. BOTTOM: the demo station showing the effect of the INGV's patent on the position of a loudspeaker's membrane. The amplifier (D), driven by a square wave signal produced by the generator C, is connected to a voice-coil B. The voice-coil position was detected by an optical position detector, E, by means of a solid state laser (A) tied to the voice coil. The oscilloscope F showed the generator's output, the position of the voice-coil, and the amplifier's voltage output.



grafi/) and attracted the interest of Audio Review who offered to test the amplifier in the magazine's lab. Figure 2 shows the frequency response test.

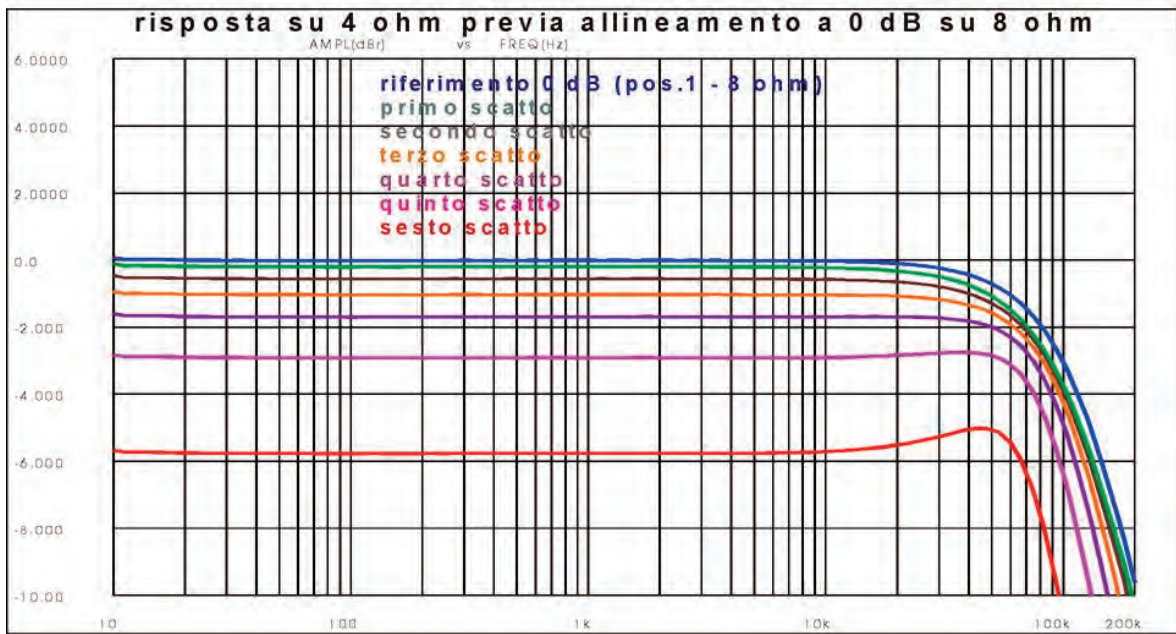
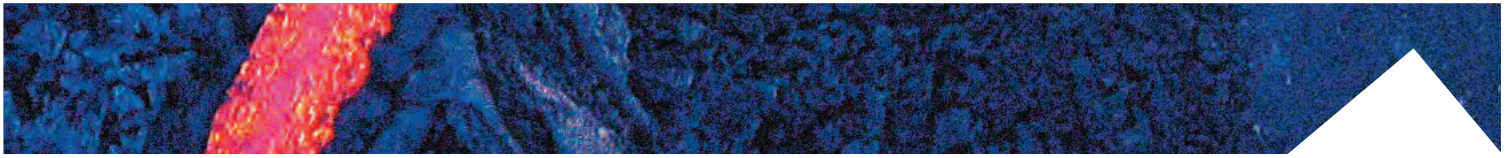


Fig. 2 | Audio Review frequency response test.



MEMS accelerometer for geophysical applications

Pongetti F.

Accelerometers built using Micro Electro Mechanical Systems (MEMS) technology are continuously evolving and are actually very popular due to performance and relatively low cost. We have designed an accelerometer sensor arranging multiple MEMS accelerometer integrated chips, in a grid like displacement. We have also designed a support and coupling mechanical substrate for the MEMS, and a suitable low noise low drift amplifier to interface the device to generic analog to digital seismologic converters (Reftek-130 is been used for testing this prototype). Based on the analog average of several low-cost MEMS this device will offer the performance of a geophysical-grade accelerometer at a fraction of the cost. Moreover such device will be extremely tolerant to strong accelerations, and will not have a preferred working position.

Testing in laboratory and in the field reveal that signal fidelity in comparison to already available commercial seismic accelerometers and velocimeters is very good even if response at the lowest frequencies ($f < 1$ Hz) and at lowest amplitude input acceleration, evidences excessive noise and has to be further investigated. This prototype

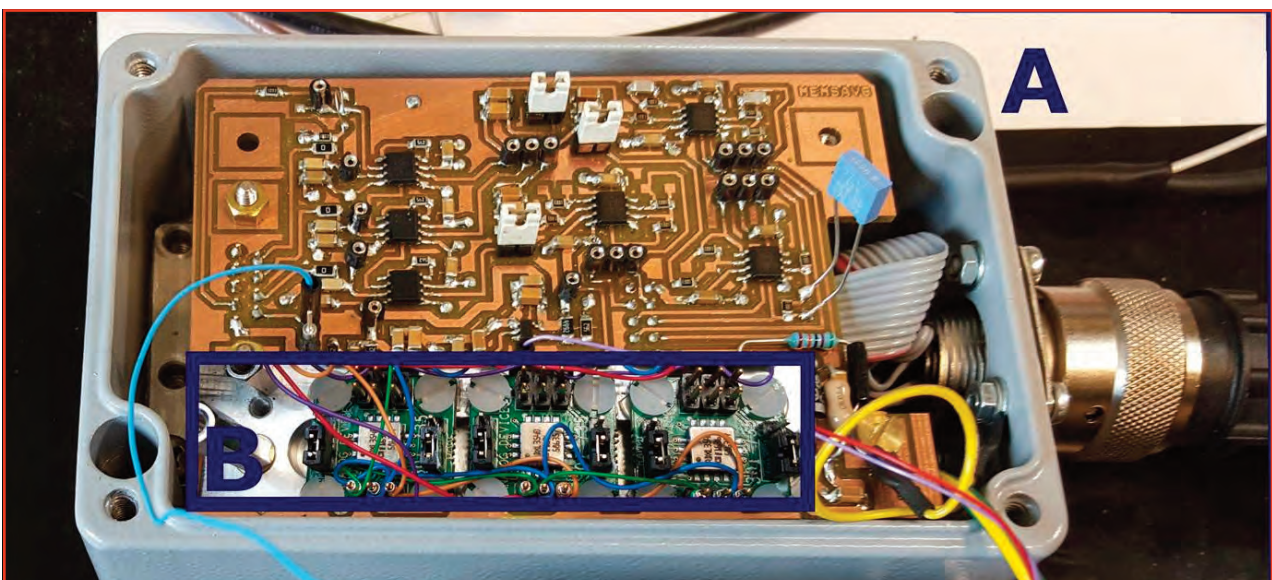
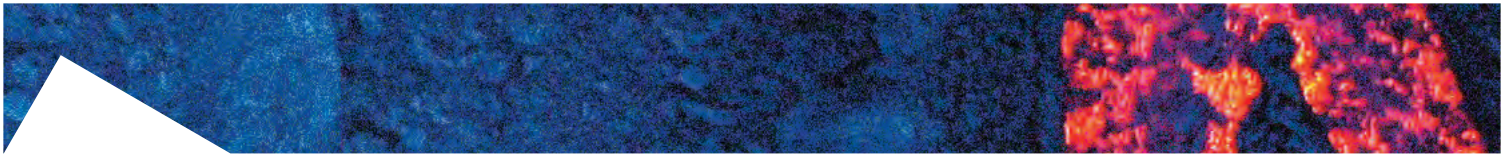
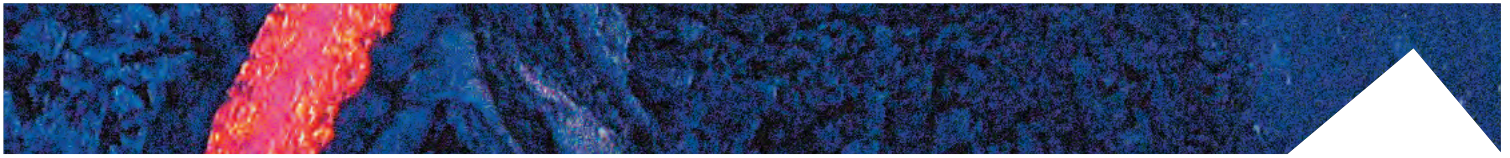


Fig. 1 | Detail A: The instrument's case hosts, at the top level, an electronic circuit for signal conditioning, power supply regulation and connectors wiring. Figure 1, detail B: At the bottom level of the case an aluminum machined plate hosts the array of MEMS.



has been developed using facilities and equipment of the NTS laboratory (New Technology and Instruments), as mechanic and electronic design and simulation CADs, printed circuit board milling machine, 3D printer, circuits assembling tools, electronic testing instrumentation, data analysis software, mechanic shop machining, electronic components warehouse, and many others.



Machine shop activity

Mari M.

Although it cannot be counted as research work, the machine shop work is essential to the conduct of all experimental investigations. Moreover the machine shop is the reference facility for the whole INGV Rome site, and performs several machining on request. Usually the machining average is of 1000 machining per year (from consumable for physics rocks experiments to more complex dedicated parts). As example of the machine shop products Figure 1 shows a MEMS housing to build a geophysical grade accelerometer from low cost chips (left) and some parts built for the restoration of historical instruments (right)

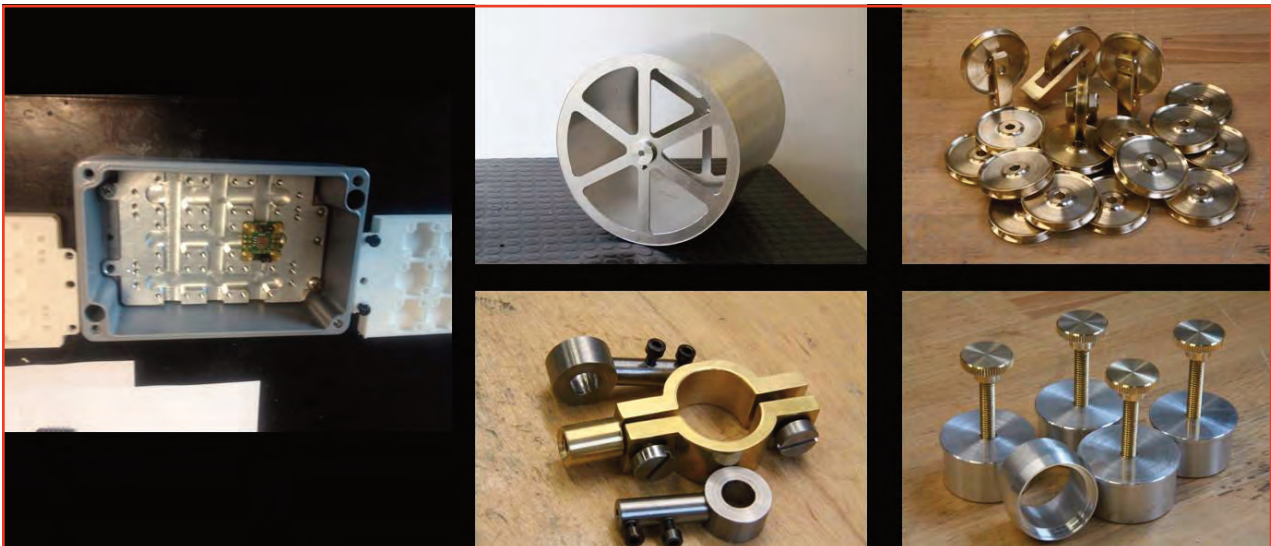
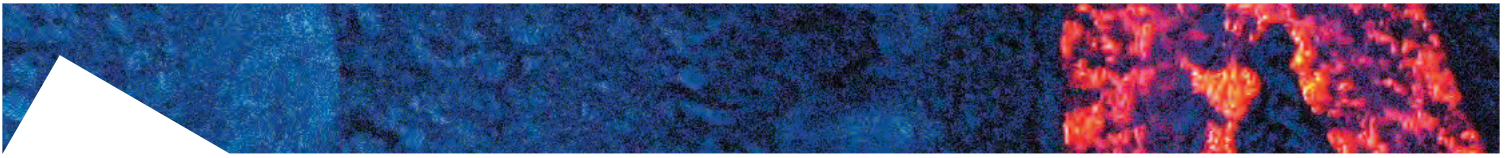


Fig. 1 | Some sample of the machine shop products.

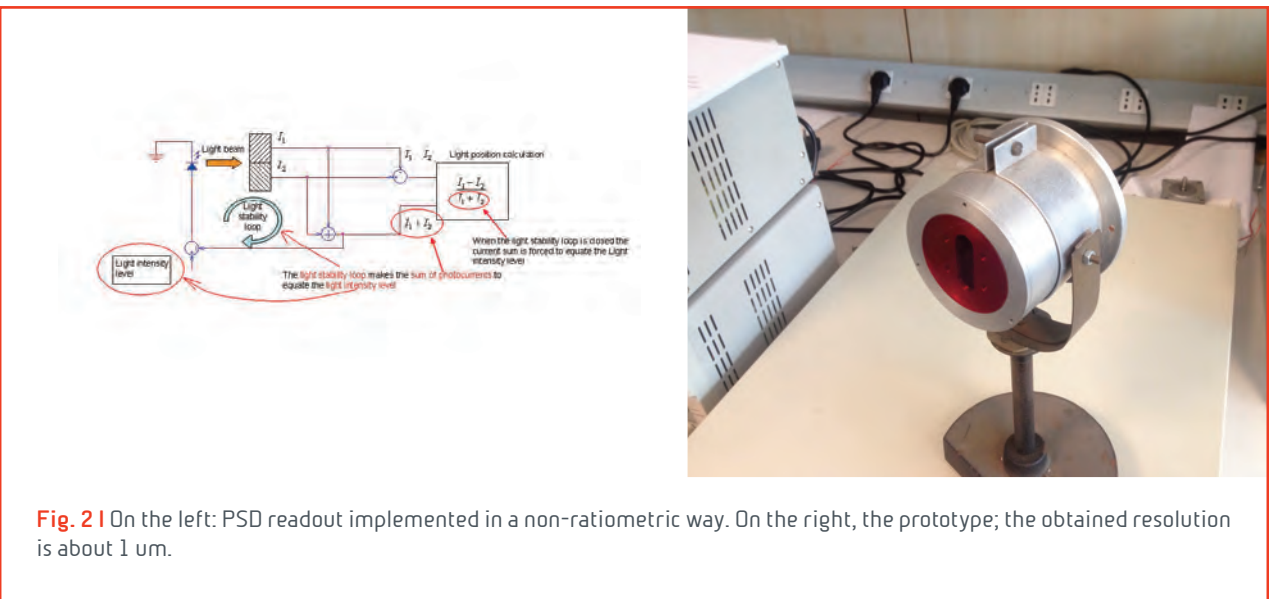
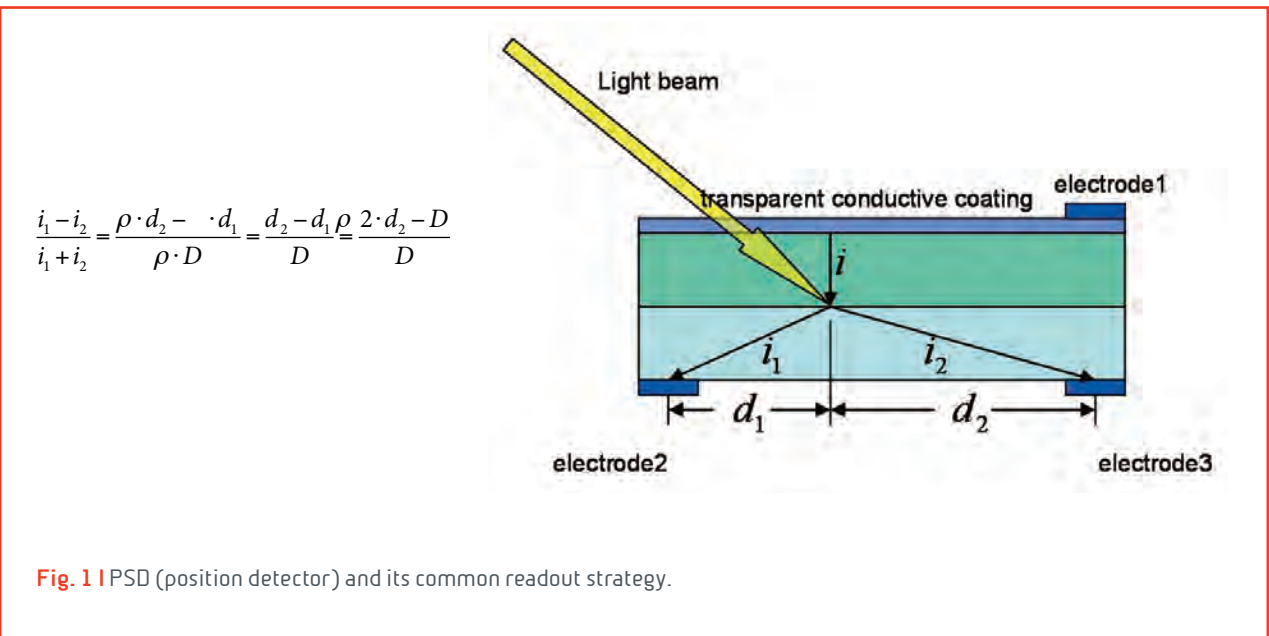


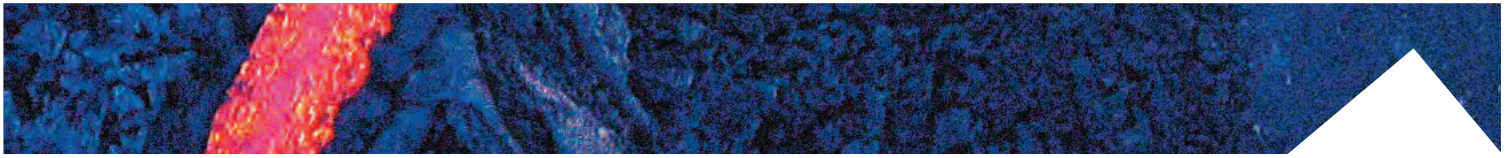
PSD readout

Romeo G.

The demo desk who showed to the INGV's amplifier performances is based on a PSD detector. A small device has been set up for detecting the Voice coil position. Usually PSDs use a ratiometric readout method, making the ratio between difference and sum of currents from the sensor (Figure 1 and 2).

In the prototype the reference sum $i_1 + i_2$ is forced to be constant by the feedback circuit so avoiding the need to compute the ratio (the denominator is constant), making a device robust and easy to be implemented analogically.





The HERMes project

Romeo G., Lepore N., Iarocci A., Spinelli G., Di Stefano G.

As a part of the H2020 HEMERA (<https://www.hemera-h2020.eu/page-d-exemple/work-packages/>) offers launch and accommodation facilities for stratospheric research balloons. Moreover ASI funds Italian projects approved by HEMERA.

The HERMes (HEmera Returning Messenger) is to design, build and fly a stratospheric glider released from a stratospheric balloon. The main goals of HERMes are: data transfer from large stratospheric balloons (too expensive to be transferred by satellite) and sampling and measurement of high atmosphere during the descent (i.e. volcanic cloud investigation).

LNTS is hardly working to design the complete system consisting in:

Balloon side: Power Management module (including solar array); Com & Control module (Iridium and GPS/Glonass); flight computer simulator (Raspberry); Glider release system.

Glider side: autopilot, Comm & Control module (Iridium and GPS/Glonass); Data disk (SSD).

Ground side: Communication and positioning system (Iridium and GPS/Glonass).

LNTS is currently prototyping two modules: the Communication & Control module and the Power Management module.

The first module acquires data from an inertial platform, an altimeter, a GPS and transmits them, together with various

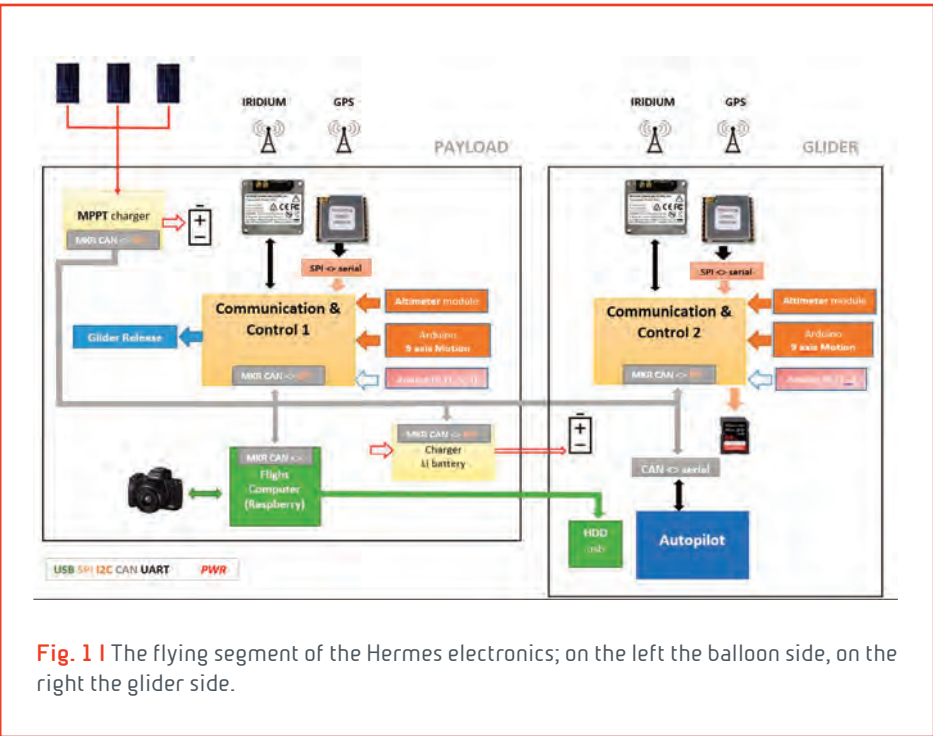
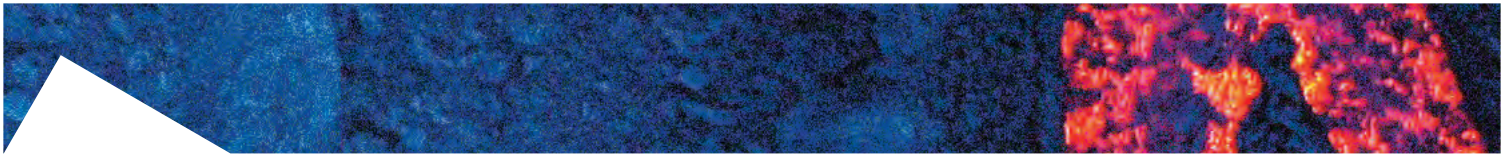


Fig. 1 | The flying segment of the Hermes electronics; on the left the balloon side, on the right the glider side.

housekeeping data, to the ground station via a satellite modem. The module saves the same data on the flight computer and on the SSD on-board the glider. When the module receives the glider release command from the ground station, before executing it, it transmits the coord-



dinates of the landing point to the glider autopilot.

The second module (Power Management), provides the energy for the whole system, keeps the battery charged and warm, and supplies some extra charge for the glider battery, just before releasing. Figure 1 shows the schematic diagram of the air segment of the system.



9 | SEMINARS and TEACHING

Seminars

Di Stefano G. | **General Electronic Physics Department** | Sapienza Università di Roma | March-June

Di Toro G. | **Partecipazione al workshop su “Come l’attività fisica aiuta i ragazzi ad andare bene a scuola”** | Casale Sul Sile (TV, Italy) | April

Di Toro G. | **“Terremoti (e tsunami)”** | Scuola Elementare Reggia dei Carraresi | Padova, Italy | May

Di Toro G., Masoch S. | **La Scienza per la Protezione Civile. Terremoti in Laboratorio** | Virtual tour dei laboratori di Ingegneria Strutturale, Idraulica e Geoscienze | Padova, Italy | October

Di Toro G. | **I terremoti, un’emergenza (anche) di comunicazione: il caso de l’Aquila** | Liceo Scientifico Galileo Galilei | San Donà di Piave (Venezia), Italy | November

Di Toro G. | **Il ciclo sismico. Serie di laboratori con Sistema massa più molla** | I.I.S. Atesino | Este (Padova), Italy | December

Ricci T. | **Campi Flegrei and Vesuvius: volcanic hazards and much more! “Pompeii, Vesuvius, and the Flaming Fields”** | New York University | March 29

Ricci T. | **I vulcani: pericolosità, rischio e aspetti sociali** | Lectiones magistrales “Renato Funicello” 2018-2019 | Tivoli | March 1

Romeo G., Saccorotti G. | **Eppur si muove: terremoti e fenomeni geologici (con particolare attenzione alla strumentazione per rilevarli)** | Lezione a due voci per Pianeta Galileo | Pisa | April 27

Romeo G. | **To boldly go where no man wants to go** | Futuro Remoto | Napoli | May 28

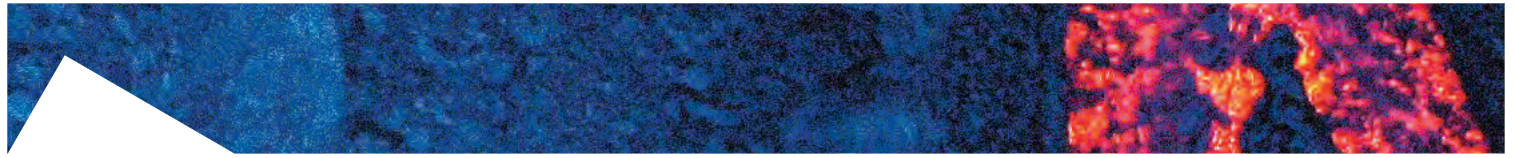
Romeo G. | **Attitude Control System: lessons in the teaching of “Space Astrophysical Methods”** | Sapienza Università di Roma | December 12 - 19

Taddeucci J. | **The birth and rebirth of volcanic ash** | Tsukuba volcanology seminar, NIED | Tsukuba, Japan | May

Taddeucci J. | **In-flight eruption dynamics: approaches at Stromboli** | CONVERSE Eruption Dynamics workshop | San Francisco, USA | December

Training

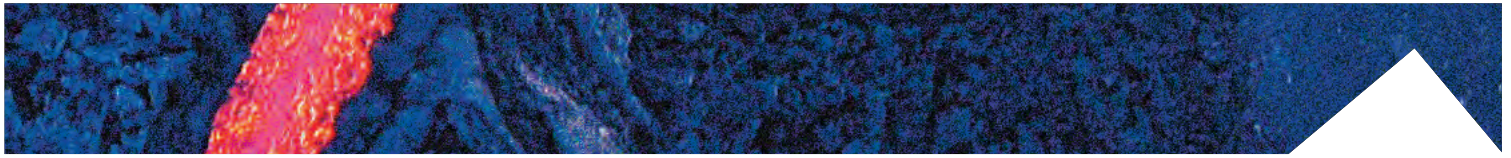
1. Aretusini S. | **Stage | Experimental studies of frictional properties of water- and fluid-rich gouges. Grant from the ERC CoG NOFEAR** | Supervisor: E. Spagnuolo



2. Cantonetti M. | **Stage | Analisi di video ad alta velocità dell'attività esplosiva di tipo stromboliano** | Supervisors: Taddeucci J. - INGV - Roma | Battaglia M. - Sapienza Università di Roma
3. Fontaine F. Robert E., Vaitiligom A., Laborde C. | **Study trip on Italian active volcanoes, August 28 – September 9, 2019** | Collaboration between INGV and La Cité du Volcan, Réunion des Musées Régionaux (Réunion island, Indian Ocean, France DOM) | Supervisor: T. Ricci
4. Gomila R. | **Architecture of fault zones in the continental crust: geological constraints. Grant from the ERC CoG NOFEAR** | Supervisor: E. Spagnuolo
5. Harbord C. | **Experimental studies of elastic properties and attenuation of fault zones. Grant from the ERC CoG NOFEAR** | Supervisor: E. Spagnuolo
6. Pennacchia F. | **Master student training in the use of Analogue Lab and High speedcameras** | Supervisors: G. Giordano - Università Roma Tre | Del Bello E. - INGV - Roma

Thesis

1. Bigaroni N. | **Master Thesis | Experimental study of the evolution of the Vp/Vs ratio with changes in fluid pressure** | Supervisors: Trippetta F. and Scuderi M. - Sapienza Università di Roma
2. Cantonetti M. | **Master Thesis | Studio sperimentale dei getti supersonici e loro implicazioni per le eruzioni vulcaniche Stromboliane** | Supervisors: Taddeucci J. - INGV - Roma | Palladino D. M. - Sapienza Università di Roma
3. Moltoni R. | **Triennale Thesis | Caratterizzazione di rocce di faglia sperimentali** | Supervisors: Collettini C. and Ruggieri R. - Sapienza Università di Roma
4. Moschini P. | **Master Thesis | Relationship between Radon emission and CO2 flux at Nisyros Island (Aegean Sea, Greece)** | Supervisors: Mollo S. and Lucchetti C. - Sapienza Università di Roma | Bini G. - ETH - Zurich
5. Panunzi S. | **Master Thesis | Studio sperimentale dei getti supersonici e loro emissioni acustiche nelle eruzioni Vulcaniche Stromboliane** | Supervisors: Taddeucci J. - INGV - Roma | Palladino D. M. - Sapienza Università di Roma
6. Schiavon B. | **Master Thesis | Termobarometria dei prodotti effusivi ed esplosivi dell'isola di Vulcano** | Supervisors: Mollo S. and Palumbo F. - Sapienza Università di Roma
7. Valentini F. | **Master Thesis | Dinamiche delle eruzioni dello Stromboli dell'estate 2019 sulla base dei prodotti dei social media** | Supervisors: Taddeucci J. - INGV - Roma | Palladino D. M. - Sapienza Università di Roma
8. Valentini F. | **Stage | Analisi di video ad alta velocità dell'attività esplosiva di tipo stromboliano** | Supervisors: Taddeucci J. - INGV - Roma | Battaglia M. - Sapienza Università di Roma



PhD

1. **Bigaroni N. | PhD | Riprodurre il ciclo sismico di una faglia complessa in laboratorio e predire l'andamento con il machine learning | Supervisors:** Scuderi M. – Sapienza Università di Roma | Di Stefano G. | INGV
2. **Del Rio L. | PhD | Mechanism of formation of slip surfaces in carbonate-built rocks: seismic faulting vs. Deep Seated Gravitational Slope Deformation | Supervisor:** Di Toro G. – Università di Padova; co-supervisors Fondriest M., Saroli M., Gori S., Falucci E., Moro M.
3. **Giacomel P. | PhD | Laboratory investigation on the frictional properties of basalts interacting with H₂O- and CO₂-rich fluids and implications for CO₂ storage | Supervisors:** Collettini C. – Sapienza Università di Roma | Spagnuolo E. – INGV | Di Toro G. – Università di Padova
4. **Masoch S. | PhD | Structure, evolution and deformation mechanisms of large displacement seismogenic faults in the continental crust | Supervisor:** Di Toro G.; co-supervisors: Pennacchioni G., Cembrano J.
5. **Mercuri M. | PhD | Struttura e comportamento meccanico di zone di faglia carbonatiche in presenza di plaghe argillose | Supervisors:** Collettini C. and Carminati E. – Sapienza Università di Roma
6. **Nazzari M. | PhD | Unravelling the effect of undercooling on (dis)equilibrium textures and compositions of basaltic magmas | Supervisor:** Mollo S. – Sapienza Università di Roma
7. **Ruggieri R. | PhD | Experimental investigation on fault stability of clay-bearing carbonate fault rocks | Supervisors:** Trippetta F. and Scuderi M. – Sapienza Università di Roma | Di Stefano G. -INGV Roma I
8. **Wei F. | PhD | Investigation of seismic slip in experimental faults under hydrothermal conditions. Chinese Government Scholarship | Supervisor:** Di Toro G. – Università di Padova



101 VISITING SCIENTISTS

Magnarini G. | **UCL** | London | *March*

Yagolnitzer Y. | **University of Otago** | New Zealand | *March*

Jensen E. | **Universidad Católica del Norte** | Chile | *March*

Ubide T. | **University of Queensland** | Australia | *May*

Moraleda A.T. | **Escuela Politécnica Superior, Departamento Tecnología Electrónica, Universidad Carlos III** | Madrid | *April*

Casajero A.N. | **Escuela Politécnica Superior, Departamento Tecnología Electrónica, Universidad Carlos III** | Madrid | *April*

Beard C.D. | **British Geological Survey** | United Kingdom | *May*

Roslizar A. | **Karlsruhe Institute of Technology** | Germany | *September*

Tisato N. | **University of Texas at Austin** | *October*

Niemeijer A. | **Utrecht University** | The Netherlands | *October*

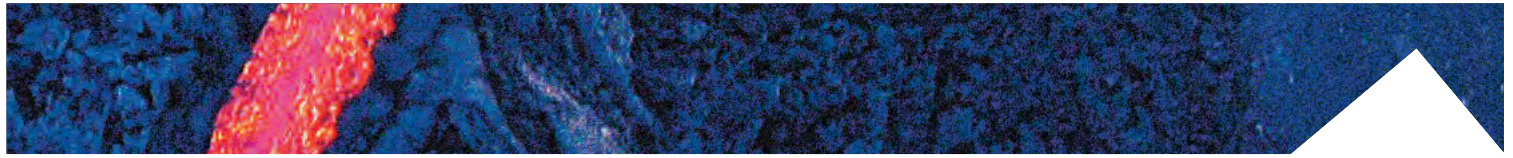
Roubidoux P. | **Boise State University, Idaho** | USA | *November*

Pontesilli A. | **University of Otago** | New Zealand | *November*

Marone C. | **Penn State University** | *November*

Johnson J. | **Boise State University, Idaho** | USA | *November*

Murphy Shane | **IFREMER, Brest** | France | *November*



111 MEETINGS, WORKSHOP and SYMPOSIA

Meetings and sessions organization

Kee K.F., Mastin L.G., Del Bello E.

**Volcanic Eruptions I: Observation, Characterization, and Modeling I- IV
AGU Fall Meeting | San Francisco, USA | 9-13 December**

Stagno V., Gillmann C., McCammon C.A.

**Earth's Volatiles from the Inside Out
AGU Fall Meeting | San Francisco, USA | 9-13 December**

Meetings and sessions attendance

IAVCEI-CVL | 10th Workshop on Volcanic Lakes | Taupo and Rotorua (New Zealand) | 17-25 March

Rouwet D., Tamburello G., Sciarra A., T. Ricci, Caliro S.

Varying CO₂/H₂S ratios above the shallow Fangaia mud pool, Solfatara (Campi Flegrei, Italy)

European Geoscience Union General Assembly | Vienna | 7-12 April

Aretusini S., Cascajero A.N., Spagnuolo E., Tapetado A., Vazquez C., et al.

How hot is a lab-earthquake?

Collettini C., Tesei T., Scuderi M.M., Carpenter B.M., Viti C.

Beyond Byerlee Friction, Weak Faults and Implications for Slip Behaviour

Cornelio C., Passelegue F., Spagnuolo E., Di Toro G., Violay M.

Earthquake nucleation in presence of viscous fluids: Thermal Pressurization or Elastohydrodynamic Lubrication?

Del Rio L., Di Toro G., Fondriest M., Moro M., Saroli M., Gori S., Falcucci E., et al.

Slip surfaces associated with seismic faults and gravitational slope deformations in carbonate-built rocks

Di Stefano F., Scarlato P., Mollo S., Petrone C., Ubide T., Nazzari M., Andronico D.

Major and Trace Element Maps of Zoned Clinopyroxenes at Stromboli: New Clues on Complex Magma Dynamics during 2003-2017 Eruptions.

Di Toro G.

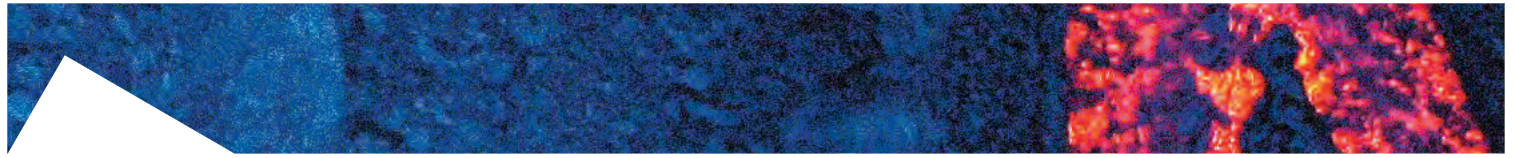
Underperforming European countries in geosciences: the case of Italy.

Di Toro G., Fondriest M., Mitchell T., Gomila R., Jensen E., Sommacampagna C., Masoch S., Bistacchi A., Magnarini G., Faulkner D., Cembrano J., Mittempergher S.

Frictional melting in fluid-rich faults (Bolfín Fault Zone, Chile).

Fondriest M., Mecklenburgh J., Passelegue F., Artioli G., Nestola F., Spagnuolo E., Di Toro G.

Pseudotachylytes alteration and their loss from the geological record.



Giacomel P., Spagnuolo E., Scuderi M., Di Toro G., Collettini C.

Frictional properties of basalts in the presence of water: role of fault displacement.

Gomila R., Jensen E., Fondriest M., Di Toro G., Mitchell T., Bistacchi A., Sommacampagna C., Masoch S., Cembrano J.

Architecture of an exceptionally exposed seismogenic source (Bolfín Fault Zone, Atacama desert, Chile).

Harbord C., Spagnuolo E., Tisato N., Di Stefano G., Di Toro G.

A new module designed to study seismic attenuation in large displacement experimental faults.

Kueppers U., Huber J., Schmid M., Walker B.H., Andronico D., Johnson J.B., Taddeucci J., Sesterhenn J.

Drone-deployed sensors capture multi-parameter perspective of explosions at Stromboli volcano.

Marthe S.G., Nielsen S., Di Toro G.

Earthquakes: from slow to fast, from the field to the laboratory and models.

Nazzari M., Di Stefano F., Mollo S., Scarlato P., Tecchiato V., Ellis B., Bachmann D., Ferlito C.

Modeling the crystallization and emplacement conditions of a basaltic trachyandesitic sill at Mt. Etna volcano.

Masoch S., Fondriest M., Di Toro G.

Cockade breccia: a geological marker of ancient seismic faulting.

Mitterpergher S., Bistacchi A., Nielsen S., Di Toro G., Gukov K.

Roughness, off-fault damage and frictional melt distribution in an exhumed seismogenic fault: quantitative high resolution data from a Digital Outcrop Model study.

Ruggieri R., Scuderi M.M., Tinti E., Trippetta F., Collettini C., Brignoli M., Mantica S., Petroselli S., Osculati L., Volonté G.

Effects of illite content on frictional properties of experimental carbonate faults.

Scuderi M.M., Cappa F., Collettini C., Guglielmi Y., Avouac J.P.

Understanding Injection-Induced Seismicity and Aseismic Fault Slip Coupling Laboratory and In-Situ Experiments with Hydromechanical Models.

Spagnuolo E., Aretusini S., Vannucchi P., Di Toro G., Nielsen S.

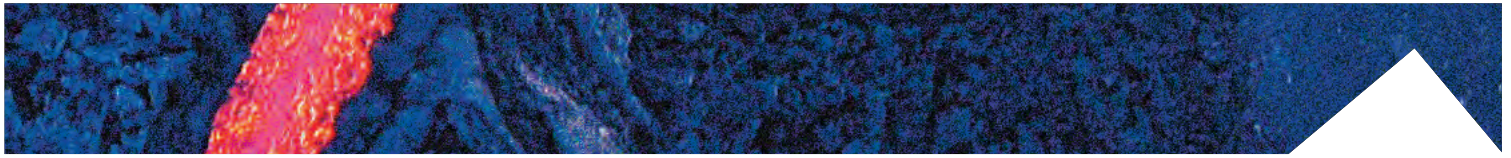
Seismic slip propagation at shallow depth in subduction zones earthquakes: an experimental study on Costa Rica and north Sumatran subduction zone input materials.

Taddeucci J., Peña Fernández J.J., Andronico D., Del Bello E., Johnson J.B., Küppers U., Ricci T., Scarlato P., Sesterhenn J., Spina L.

Vortex rings and acoustic signatures from volcanic jets at Stromboli volcano (Italy).

Tamburello G., Caliro S., Bitetto M., Giudice G., Avino R., Carandente A., Rouwet D., Ricci T., Sciarra A., Aiuppa A., Bagnato E., Minopoli C.

Rapid variations of CO₂/H₂S ratio in the fumarolic plume of Pisciarelli (Campi Flegrei volcano, Italy).



Tinti E., Scuderi M.M., Collettini C., Cocco M.

The role of shear fabric in controlling slip velocity function and breakdown work during laboratory slow slip.

Japan Geosciences Union Meeting | Chiba, Japan | 26-30 May

Taddeucci J., Scarlato P., Del Bello E., Ricci T., Kueppers U., Houghton B.

The in-flight grain size distribution of lapilli and bombs from Strombolian explosions.

Taddeucci J., Alatorre-Ibarguengoitia M.A., Cigala V., Del Bello E., Gaudin D., Kueppers U., Ricci T., Salvatore V., Scarlato P.

The source depth of Strombolian explosions: a multiparametric approach and comparison.

Workshop Fault2SHA | Barcelona (Spain) | 3-5 June

EMERGEO Working Group Etna 2018.

The 2018 Mw 4.9 Etna earthquake: how fault rupture fits SHA based on geologic approaches.

International Conference on Coupled THMC Processes in Geosystems | Utrecht (Netherlands) | 3-5 July

Arestusini S., Spagnuolo E., Di Toro G.

Linking THMC processes to the earthquake energy budget: experimental deformation of smectite-rich gouges.

Del Rio L., Fondriest M., Moro M., Saroli M., Gori S., Falcucci E., Spagnuolo E., Di Toro G.

Mechanism of formation of slip surfaces in carbonate-built rocks: seismic faulting vs. deep-seated gravitational slope deformation (Italian Central Apennines).

Di Toro G., Fondriest M., Mitchell T., Gomila R., Jensen E., Sommacampagna C., Masoch S., Bistacchi A., Magnarini G., Faulkner D., Cembrano J., Mittempergher S.

Frictional melting in fluid-rich faults (Bolfín Fault Zone, Chile).

Fondriest M., Mecklenburgh J., Passelegue F.X., Artioli G., Nestola F., Spagnuolo E., Di Toro G.

Pseudotachylite alteration and their loss from the geological record.

Hung C.C., Kuo L.W., Di Felice F., Li H., Spagnuolo E., Di Toro G., Si J., Wang H.

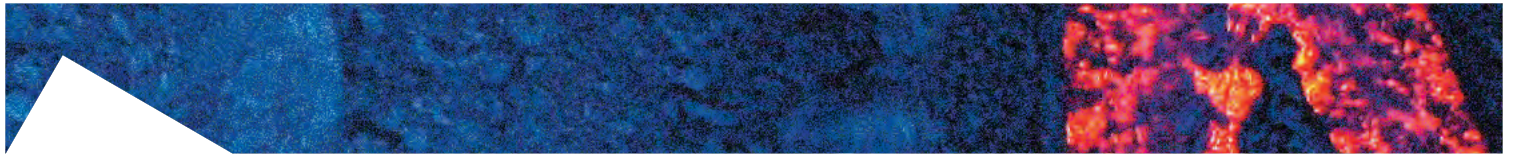
Frictional properties of fault zone gouges from the WFS-3 drilling project (2008 Mw 7.9 Wenchuan earthquake).

Masoch S., Fondriest M., Di Toro G.

Seismic cycle recorded in cockade-bearing faults (Col de Teghime, Alpine Corsica).

Spagnuolo E.

Chemical and hydro-mechanical coupling in fault zones: an experimental overview.



Wang H., Li H.B., Si J.L., Di Toro G.

Geochemistry of pseudotachylyte formed at shallow depths during large in magnitude.

IUGG General Assembly | Montreal (Canada) | 8-18 July

Hughes A., Kendrick J., Di Toro G., Salas G., Lavalleyé Y.

A Field and Experimental Study of Shear Localisation and Frictional Melting in Volcanic Debris Avalanches.

CRUST workshop | Perugia (Italy) | 9-10 July

Del Rio L., Fondriest M., Moro M., Saroli M., Gori S., Falcucci E., Spagnuolo E., Di Toro G.

Slipping zones associated with seismic faults and gravitational slope deformations in carbonate-built rocks (Central Apennines, Italy).

Fondriest M., Bistacchi A., Demurtas M., Balsamo F., Clemenzi L., Storti F., Valoroso L., Di Toro G.

Three-dimensional anatomy of an active seismic source: kinematic complexity and structural inheritance constrained by field observations and present-day seismic activity (Central Apennines, Italy).

20th INQUA Congress | Dublin (Ireland) | 25-31 July

EMERGEIO Working Group Etna 2018.

Surface Ruptures Following The 26 December 2018, Mw4.9, Mt. Etna Earthquake, Sicily (Italy).

Goldschmidt 2019 Conference | Barcelona, Spain | 18-23 August

Di Stefano F., Mollo S., Blundy J., Scarlato P., Nazzari M., Bachmann O.

The Effect of CaO on the Partitioning Behavior of REE, Y and Sc between Olivine and Melt: Implications for Basalt-Carbonate Interaction Processes.

Di Stefano F., Scarlato P., Mollo S., Petrone C.M., Ubide T., Nazzari M., Andronico D.

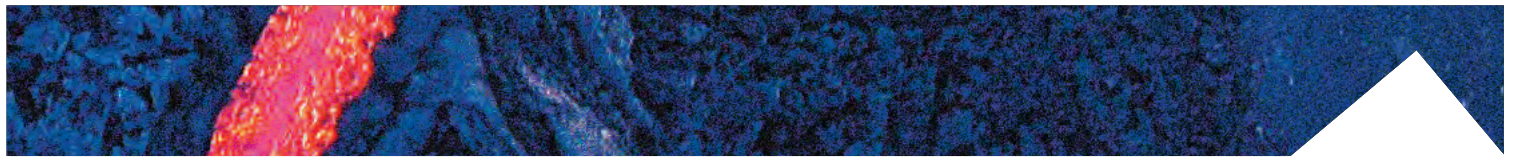
Major and Trace Element Maps of Zoned Clinopyroxenes at Stromboli: New Clues on Complex Magma Dynamics during 2003-2017 Eruptions.

Stagno V.

The Redox State of the Graphite- and Diamond-Bearing Eclogite Xenoliths from Udachnaya Kimberlite Pipe (Siberian Craton): Implication for the Origin of Diamonds.

Stagno V.

Viscosity and Atomic Structure of CO₂-bearing Magmas in the Earth's Interior.



17th International Symposium on Geo-disaster Reduction I Issyk Kul Lake (Kyrgyz Republic) I 19-23 August

EMERGEO Working Group Etna 2018

Surface Ruptures Following The 26 December 2018, Mw 4.9, Mt. Etna Earthquake, Sicily (Italy).

SIMP-SGI-SOGEI Conference I Parma, Italy I 16-19 September

Cortinovis S., Balsamo F., Fondriest M., La Valle F., Di Toro G.

Structural architecture and microstructural properties of the seismogenic Monte Marine Fault Zone, Central Apennines (Italy).

Di Fiore F., Vona A., Romano C., Sulpizio R., Mollo S.

The role of undercooling and strain rate on the syn-eruptive rheological evolution of the magma feeding the Pollena eruption of Somma-Vesuvius (Campania; Italy).

Di Stefano F., Mollo S., Blundy J.D., Scarlato P., Nazzari M., Bachmann O.

The effect of CaO on the partitioning behavior of REE, Y and Sc between olivine and melt: Implications for basalt-carbonate interaction processes.

Giuliani L., Iezzi G., Davis M., Hippeli T., Vetere F., Elbrecht A.L., Nazzari M., Mollo S., Scarlato P.

Onset of crystallization in a cooling MORB: an in-situ DSC investigation.

Giuliani L., Iezzi G., Casarin A., Piattelli V., Lanzafame G., Nazzari M., Ferlito C., Mollo S., Scarlato P., Trabucco F., Colò M.

Textural variations along a vertical section of a distal portion of an Etnean lava flow.

Meneghini F., Aretusini S., Spagnuolo E., Harbord C., Di Toro G.

Weakening mechanisms and rupture propagation along the Hikurangi margin frontal thrust: preliminary results from high speed friction experiments under controlled fluid pressure.

Merico A., Iezzi G., Pace B., Ferranti L., Cremona M., Scafa M., Nazzari M., Colella A., Scarlato P.

Texture of tectonised calcite clasts from a lithified fault core: a case study from the San Benedetto-Gioia dei Marsi fault (central Italy).

Morgavi D., Spina L., Cannata A., Musu A., Campeggi C., Perugini D.

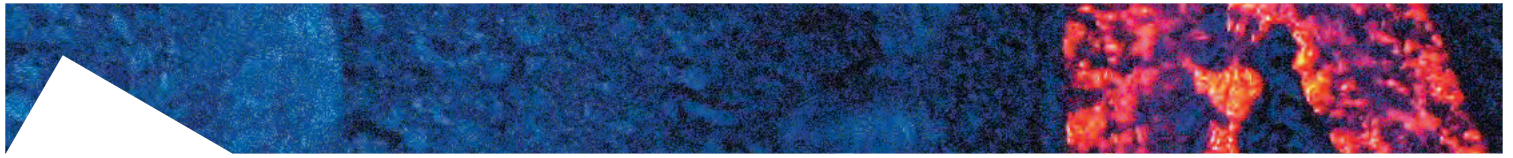
AEOLUS: a laboratory to study bubble-bearing flow dynamics and geophysical signals through analogue volcanic eruption.

Musu A., Morgavi D., Spina L., Corsaro R.A., Perugini D.

Lava fountaining activity: the Collapsing Foam Layer Model applied to the 2000 – 2013 South-East Crater eruptive period (Mt. Etna, Italy).

Rouwet D., Chiodini G., Pecoraino G., Tamburello G., Procesi M., Venturi S., Santi A., Ricci T., Cabassi J., Tassi F.

Resuming volcanic surveillance at Lago Albano: updates on the dissolved gas content and vertical temperature profiles.



Spina L., Morgavi D., Cannata A. Perugini D.

Experimental investigations on degassing behavior and related seismo-acoustic markers: the effect of complex conduit geometries.

GSA Annual Meeting I Phoenix (Arizona) I 22-25 September

Houghton B.F., Tisdale C.M., Wakker B.H., Taddeucci J.

Characterizing and explaining mildly explosive basaltic volcanism: examples from Kilauea in 2018.

Società Italiana di Fisica I L'Aquila, ITA I 23-27 September

Collettini C., Scuderi M.M., Tinti E.

The spectrum of tectonic failure modes and earthquake precursors: insights from rock deformation experiments

Deep Carbon 2019: Launching the Next Decade of Deep Carbon Science I Washington DC I 24-26 October

Stagno V.

Origin and rheology of CO₂-rich magmas controlled by changes in the mantle oxidation state through time.

Wind-remobilisation processes of volcanic ash workshop I Bariloche, Argentina I 23-26 October

Del Bello E., Taddeucci J., Scarlato P.

Experimental and field studies of the resuspension of volcanic ash by wind.

Congresso del Gruppo Nazionale di Geofisica della Terra Solida I 12-14 November

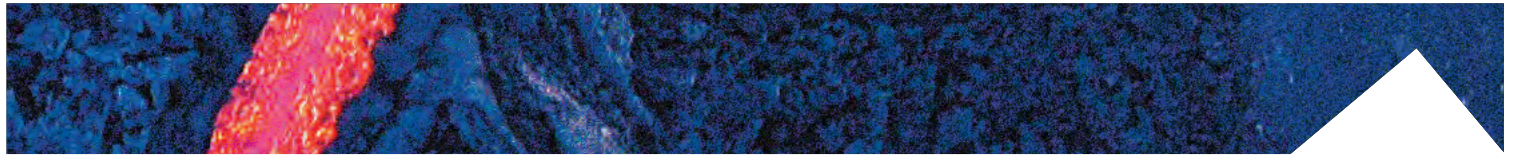
Del Rio L., Fondriest M., Moro M., Saroli M., Gori S., Falcucci E., Spagnuolo E., Di Toro G.

Gravitational Slope Deformation vs. Normal Faults: different hazards, similar microstructures?

AGU Fall Meeting I San Francisco, USA I 9-13 December

Andronico D., Del Bello E., Ciancitto F.A., Cristaldi A., D'Oriano C., Landi P., Pennacchia F., Ricci T., Scarlato P., Taddeucci J.

The 3 July 2019 Paroxysm of Stromboli.



Bistacchi A., Mittempergher S., Di Toro G.

New combined nonparametric/parametric statistical analysis of fracture networks to unravel the evolution of fault zones: a study of the exhumed seismogenic Gole Larghe Fault Zone (Italian Southern Alps).

Collettini C., Tesei T., Scuderi M.M., Carpenter B.M., Viti C.

Beyond Byerlee Friction, Weak Faults and Implications for Slip Behaviour.

Cornelio C., Passelegue F.X., Spagnuolo E., Di Toro G., Violay M.

Earthquake reactivation and seismic slip in presence of viscous fluids.

Del Bello E., Taddeucci J., Merrison J., Rasmussen K.R., Iversen J.J., Scarlato P., Ricci T., Andronico D.

PoWAR: a portable wind tunnel facility for studying in situ resuspension of volcanic ash.

Di Toro G., Fondriest M., Mitchell T.M., Gomila R., Siles E.J., Bistacchi A., Magnarini G., Faulkner D.R., Cembrano J.M., Mittempergher S., Spagnuolo E., Masoch S.

Field and experimental evidence of frictional melting in fluid-rich faults.

Gomila R., Jensen E., Fondriest M., Masoch S., Di Toro G., Mitchell T., Magnarini G., Pennacchioni G., Cembrano J.

An exceptionally exposed seismogenic source in the Atacama Desert: The Bolfin Fault Zone (Chile).

Harbord C., Spagnuolo E., Di Toro G.

Scaling of the dynamic slip weakening distance with acceleration during laboratory earthquake-like slip events.

Johnson J.B., Anderson J., Behnke S., Del Bello E., Edens H., Marshall A., Ortiz H., Pineda A., Taddeucci J., Vargas S., Watson L., Zorn E.

Volcano Storytelling.

Kueppers U., Huber J., Schmid M., Andronico D., Johnson J.B., Ripepe M., Taddeucci J., Scarlato P.

Mind the gap: refined acoustic characterisation of explosions at Stromboli volcano using drone-deployed sensors and near-field arrays.

Masoch S., Gomila R., Fondriest M., Siles E.J., Magnarini G., Spagnuolo E., et al.

Pseudotachylytes from the Atacama Desert (Northern Chile).

Mittempergher S., Bistacchi A., Di Toro G., Nielsen S., Gukov K.

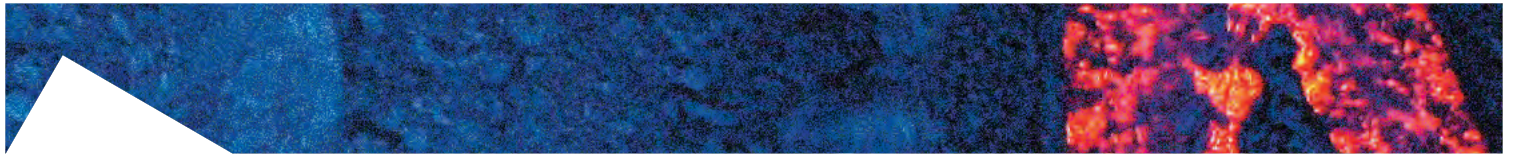
Roughness, Off-fault Damage and Frictional Melt Distribution in an Exhumed Seismogenic Fault.

Pucci S., Villani F., Civico R., Di Naccio D., Porreca M., Sapia V., Di Giulio G., Baccheschi P., Amoroso S., Cantore L., Salomon H., Smedile A., Vassallo M., Marchetti M., Benedetti L.C., Gueli A., Stella G., Ricci T., Pantosti D.

Geometry and evolution of the Middle Aterno Quaternary basin and relationship with the 2009 L'Aquila earthquake causative fault system (Abruzzi Apennines, Italy).

Rempe M., Renner J., Di Toro G.,

Hydrothermal Alteration of Natural Pseudotachylytes and Synthetic Glasses.



Ricci T., Andronico D., Cantarero M., Civico R., De Beni E., Del Bello E., Di Traglia F., Eggensglüß M., Hansteen T.H., Hoernle K., Johnson J.B., Kwasnitschka T., Pizzimenti L., Scarlato P., Strehlow K., Taddeucci J.

Monitoring the morphological changes associated with the 3 July 2019 paroxysmal eruption at Stromboli volcano (Italy) using UAVs.

Rowe C., Lamothe K., Rempe M., Andrews M., Mitchell T.M., Di Toro G., White J.C., Aretusini S., Harrichhausen N., Gonzalez C.

Earthquake lubrication and healing caused by amorphous silica powder - experimental wear products compared to natural fault rocks .

Sapia V., Villani F., Fischanger F., Lupi M., Baccheschi P., Brunori C.A., Civico R., Coco I., De Martini P.M., Giannattasio F., Improta L., Materni V., Murgia F., Pantosti D., Pizzimenti L., Pucci S., Ricci T., Romano V., Sciarra A., Smedile A.

3D modelling of the fault-bounded Castelluccio basin (2016 Mw 6.5 Norcia earthquake, central Italy) using deep resistivity Full Waver survey.

Scarlato P., Del Bello E., Ricci T., Kueppers U., Houghton B., Taddeucci J.

The total grain size distribution of tephra from Strombolian explosions: in the air.

Scuderi M.M., Collettini C.

Stress triggering and the mechanics of fault slip behavior.

Scuderi M.M., Collettini C.

Evolution of hydrologic and frictional properties of quartz-illite mixtures.

Spagnuolo E., Aretusini S., Meneghini F., Harbord C., Di Toro G.

Dynamic weakening and seismic slip propagation along the Hikurangi margin shallow subduction fault under realistic pore fluid pressures.

Stagno V.

The redox boundaries and volatiles cycle of Earth's interior through space and time.

Taddeucci, J., Pena-Fernandez, J.J., Andronico, D., Del Bello, E., Johnson, J.B., Kueppers, U., Ricci T., Scarlato P., Sesterhenn J., Spina, L.

Vortex rings and acoustic signatures illuminate vent diameter and jet velocity of Strombolian explosions.

Tisato N., Harbord C., Spagnuolo E., Di Stefano G., Di Toro G.

A new apparatus to study visco-elastic properties in large displacement experimental faults.

Tisdale C.M., Houghton B.F., Taddeucci J.

In-flight Parameters for the first 90 minutes of activity at Fissure 8 during the 2018 Eruption of Kilauea's LERZ.

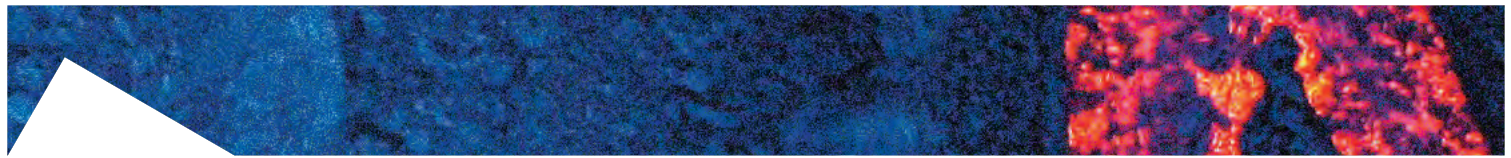
Vannucchi P., Spagnuolo E., Aretusini S., Di Toro G., Nielsen S.B.

Controlling factors on the shallow co-seismic slip at the Sumatra subduction zone megathrust.

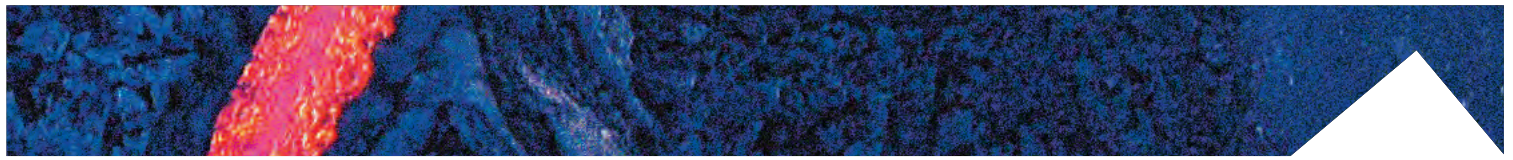


121 PUBLICATIONS

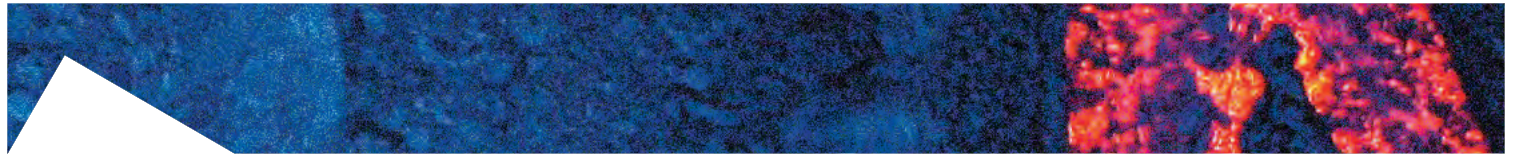
1. *Aretusini S., Spagnuolo E., Dalconi M.C., Di Toro G., Rutter E.H.*
Water availability and deformation processes in smectite rich gouges during seismic slip
Journal of Geophysical Research: Solid Earth 124 (11), 10855-10876
2. *Aretusini S., Plümper D., Spagnuolo E., Di Toro G.*
Subseismic to seismic slip in smectite clay nanofoliation
Journal of Geophysical Research: Solid Earth 124 (7), 6589-6601
3. *Arzilli F., Morgavi D., Petrelli M., Polacci M., Burton M., Di Genova D., Spina L., La Spina G., Hartley M.E., Romero J.E., Fellowes J., Diaz-Alvarado J., Perugini D.*
The unexpected explosive sub-Plinian eruption of Calbuco volcano (22-23 April 2015; southern Chile): Triggering mechanism implications.
Journal of Volcanology and Geothermal Research 378, 35-50.
4. *Avvisati G., Bellucci Sessa E., Colucci D., Marfè B., Marotta E., Nave R., Peluso R., Ricci T., Tomasone M.*
Perception of Risk for Natural Hazards in Campania Region (Southern Italy).
International Journal of Disaster Risk Reduction, doi:10.1016/j.ijdrr.2019.101164
5. *Barberi F., Carapezza M.L., Tarchini L., Ranaldi M., Ricci T., Gattuso A.*
Anomalous Discharge of Endogenous Gas at Lavinio (Rome, Italy) and the Lethal Accident of 5 September 2011.
GeoHealth, doi:10.1029/2019GH000211
6. *Brenna M., Pontesilli A., Mollo S., Masotta M., Cronin S.J., Smith I.E.M., Moufti M.R.H., Scarlato P.*
Transient to stationary radon (²²⁰Rn) emissions from a phonolitic rock exposed to subvolcanic temperatures
American Mineralogist 104, 1750-1764
7. *Cannata A., Cannavò F., Moschella S., Gresta S., Spina L.*
Exploring the link between microseism and sea ice in Antarctica by using machine learning.
Scientific Reports 9(1), 1-15.
8. *Cappa F., Scuderi M.M., Collettini C., Guglielmi Y., Avouac J.P.*
Stabilization of fault slip by fluid injection in the laboratory and in situ.
Science Advances, doi.org/10.1126/sciadv.aau4065.
9. *Civico R., Pucci S., Nappi R., Azzaro R., Villani F., Pantosti D., Cinti F.R., Pizzimenti L., Branca S., Brunori C.A., Caciagli M., Cantarero M., Cucci L., D'Amico S., De Beni E., De Martini P.M., Mariucci M.T., Montone P., Nave R., Ricci T., Sapia V., Smedile A., Tarabusi G., Vallone R., Venuti A.*
Surface Ruptures Following The 26 December 2018, Mw 4.9, Mt. Etna Earthquake, Sicily (Italy).
Journal of Maps, doi:10.1080/17445647.2019.1683476
10. *Cornelio C., Spagnuolo E., Di Toro G., Nielsen S., Violay M.*
Mechanical behaviour of fluid-lubricated faults
Nature communications 10 (1), 1-7
11. *Cornelio C., Passelegue F.X., Spagnuolo E., Di Toro G., Violay M.*
Effect of fluid viscosity on fault reactivation and co-seismic weakening
Journal of Geophysical Research: Solid Earth 125(1)
12. *Demurtas M., Smith S.A.F., Prior D.J., Spagnuolo E., Di Toro G.*
Development of crystallographic preferred orientation during cataclasis in low-temperature carbonate fault gouge
Journal of Structural Geology 126, 37-50
13. *Demurtas M., Smith S., Prior D., Brenker F., Di Toro G.*
Grain size sensitive creep during simulated seismic slip in nanogranular fault gouges: constraints from Transmission Kikuchi Diffraction (TKD).
Journal of Geophysical Research 127, 10197-10209, 10.1029/2019JB018071.



14. *Del Vecchio A., Poe B.T., Misiti V., Cestelli Guidi M.*
High-Temperature Evolution of Point Defect Equilibria in Hydrrous Forsterite Synthesized at 1100°C and up to 4 GPa
Minerals 9, 574.
15. *Di Piazza A., Vona A., Mollo S., De Astis G., Soto G.J., Romano C.*
Unsteady magma discharge during the “El Retiro” subplinian eruption (Turrialba volcano, Costa Rica): Insights from textural and petrological analyses
Journal of Volcanology and Geothermal Research 371, 101-115
16. *Di Stefano F., Mollo S., Blundy J., Scarlato P., Nazzari M., Bachmann O.*
The effect of CaO on the partitioning behavior of REE, Y and Sc between olivine and melt: Implications for basalt-carbonate interaction processes
Lithos 326-327, 327-340
17. *EMERGEO Working Group*
Il terremoto etneo del 26 dicembre 2018, Mw4.9: rilievo degli effetti di fagliazione cosismica superficiale.
Rapporto n. 1 del 21/01/2019, 9 doi:10.5281/zenodo.2545555
18. *EMERGEO Working Group*
Photographic collection of the coseismic geological effects originated by the 26th December 2018 Etna (Sicily) earthquake.
Miscellanea INGV, 48, 1-76, ISSN 1590-2595.
19. *Giorgetti C., Tesi T., Scuderi M.M., Collettini C.*
Experimental Insights Into Fault Reactivation in Gouge-Filled Fault Zones.
Journal of Geophysical Research, doi.org/10.1029/2018JB016813.
20. *Guerin-Marthe S., Nielsen S., Bird R., Di Toro G., Giani S.*
Earthquake Nucleation Size: Evidence of Loading Rate Dependence in Laboratory Faults.
Journal of Geophysical Research, 124, 689-708, doi: 10.1029/2018JB016803.
21. *Hung C.C., Kuo L.W., Spagnuolo E., Wang C.C., Di Toro G., Wu W.W., Dong J.J., et al.*
Grain fragmentation and frictional melting during initial experimental deformation and implications for seismic slip at shallow depths
Journal of Geophysical Research: Solid Earth, 124 (11), 11150-11169
22. *Lévy L., Maurya P.K., Byrdina S., Vandemeulebrouck J., Sigmundsson F., Árnason K., Ricci T., Deldicque D., Roger M., Gibert B., Labazuy P.*
Electrical Resistivity Tomography and Time-Domain Induced Polarization field investigations of geothermal are as at Krafla, Iceland: comparison to borehole and laboratory frequency-domain electrical observations.
Geophysical Journal International, doi:10.1093/gji/ggz240
23. *Lombardo V., Corradini S., Musacchio M., Silvestri M., Taddeucci J.*
Eruptive Styles Recognition Using High Temporal Resolution Geostationary Infrared Satellite Data
Remote Sensing 11, 669
24. *Lucca A., Storti F., Balsamo F., Clemenzi L., Fondriest M., Burgess R., and Di Toro G.*
From submarine to subaerial out-of-sequence thrusting and gravity-driven extensional faulting: Gran Sasso Massif, Central Apennines, Italy.
Tectonics, 38, 4155-4184, 10.1029/2019TC005783
25. *Lucchetti C., De Simone G., Tuccimei P., Ricci T., Finizola A., Sciarra A.*
Improving Gas Permeability Measurements for Environmental Monitoring and Management.
Journal of Waste Management & Xenobiotics, doi:10.23880/oajwx-16000123
26. *Masoch S., Fondriest M., Preto N., Secco M., Di Toro G.*
Seismic cycle recorded in cockade-bearing faults (Col de Teghime, Alpine Corsica).
Journal of Structural Geology, <https://doi.org/10.1016/j.jsg.2019.103889>, 129, 1-17
27. *Masotta M., Mollo S.*
A new plagioclase-liquid hygrometer specific to trachytic systems
Minerals, 9, 375



28. **Mollo S., Tuccimei P., Soligo M., Galli G., Iezzi G., Scarlato P.**
Transient to stationary radon (^{220}Rn) emissions from a phonolitic rock exposed to subvolcanic temperatures
Royal Society Open Science 16: 190782
29. **Nazzari M., Di Stefano F., Mollo S., Scarlato P., Tecchiato V., Ellis B., Bachmann D., Ferlito C.**
Modeling the crystallization and emplacement conditions of a basaltic trachyandesitic sill at Mt. Etna volcano
Minerals, 9, 126
30. **Passèlegue F., Aubry J., Nicolas A., Fondriest M., Deldicque D., Schubnel A., Di Toro G.**
From Fault Creep to Slow and Fast Earthquakes in Carbonates.
Geology, 47, 744-748.
31. **Polacci M., Andronico D., de' Michieli Vitturi M., Taddeucci J., Cristaldi A.**
Mechanisms of ash generation at basaltic volcanoes: the case of Mount Etna, Italy
Frontiers in Earth Science 7, 193
32. **Pontesilli A., Masotta M., Nazzari M., Mollo S., Armienti P., Scarlato P., Brenna M.**
Crystallization kinetics of clinopyroxene and titanomagnetite growing from a trachybasaltic melt: New insights from isothermal time-series experiments
Chemical Geology 510, 113-129
33. **Poret M., Finizola A., Ricci T., Ricciardi G.P., Linde N., Mauri G., Barde-Cabusson S., Guichet X., Baron L., Shakas A., Gouhier M., Levieux G., Morin J., Roulleau E., Sortino F., Vassallo R., Di Vito M.A., Orsi G.**
The buried caldera boundary of the Vesuvius 1631 eruption revealed by present-day soil CO₂ concentration.
Journal of Volcanology and Geothermal Research, doi:10.1016/j.jvolgeores.2019.01.029
34. **Revil A., Qi Y., Ghorbani A., Coperey A., Soueid Ahmed A., Finizola A., Ricci T.**
Induced polarization of volcanic rocks. 3. Imaging clay cap properties in geothermal fields.
Geophysical Journal International, doi:10.1093/gji/ggz207
35. **Romeo G.**
Use a current mirror to control a power supply,
EDN, online magazine.
36. **Rowe C., Lamothe K., Remppe M., Andrews M., Mitchell T., Di Toro G., White J.C., Aretusini S.**
Earthquake lubrication and healing explained by amorphous nanosilica.
Nature Communications, 10:320, <https://doi.org/10.1038/s41467-018-08238-y>.
37. **Sciarra A., Cantucci B., Ricci T., Tomonaga Y., Mazzini A.**
Geochemical characterization of the Nirano Mud Volcano, Italy.
Applied Geochemistry, doi:10.1016/j.apgeochem.2019.01.006
38. **Shirey, S.B., Pearson, D.G., Walter, M.J., Aulbach, S., Brenker, F.E., Bureau, H., Burnham, A.D., Cartigny, P., Chacko, T., Frost, D.J., Hauri, E.H., Jacob, D.E., Jacobsen, S.D., Kohn, S.C., Luth, R.W., Mikhail, S., Navon, O., Nestola, F., Nimis, P., Smit, K.V., Smith, E.N., Stachel, T., Stagno, V., Steele, A., Thomassot, E., Thomson, A.R., Weiss, Y.**
Diamonds and the Mantle Geodynamics of Carbon: Deep Mantle Carbon Evolution from the Diamond Record.
In B. Orcutt, I. Daniel & R. Dasgupta (Eds.) Deep Carbon: Past to Present (pp. 89-128). Cambridge: Cambridge University Press.
39. **Spina L., Cannata A., Morgavi D., Perugini D.**
Degassing behaviour at basaltic volcanoes: New insights from experimental investigations of different conduit geometry and magma viscosity.
Earth-science reviews 192, 317-336
40. **Spina L., Morgavi D., Costa A., Scheu B., Dingwell D.B., Perugini D.**
Gas mobility in rheologically-layered volcanic conduits: The role of decompression rate and crystal content on the ascent dynamics of magmas.
Earth and Planetary Science Letters 524, 115732
41. **Stagno, V., Cerantola, V., Aulbach, S., Lobanov, S., McCammon, C.A., Merlini, M.**
Carbon-bearing phases throughout Earth's interior - evolution through space and time.
In B. Orcutt, I. Daniel & R. Dasgupta (Eds.), Deep Carbon: Past to Present (pp. 66-88). Cambridge: Cambridge University Press.



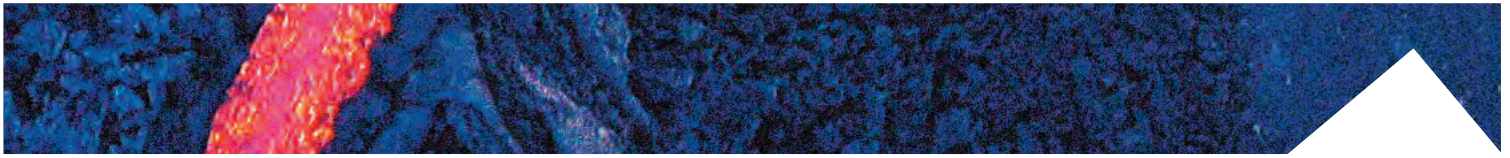
42. *Tamburello G., Caliro S., Chiodini G., De Martino P., Avino R., Minopoli C., Carandente A., Rouwet D., Aiuppa A., Costa A., Bitetto M., Giudice G., Francofonte V., Ricci T., Sciarra A., Bagnato E., Capecchiacci F.*
Escalating CO₂ degassing at the Pisciarelli fumarolic system, and implications for the ongoing Campi Flegrei unrest.
Journal of Volcanology and Geothermal Research, doi:10.1016/j.jvolgeores.2019.07.005
43. *Tournigand P.Y., Peña Fernández J.J., Taddeucci J., Perugini D., Sesterhenn J., Palladino D.M.*
Time evolution of transient volcanic plumes: Insights from fractal analysis
Journal of Volcanology and Geothermal Research 371, 59-71
44. *Ubide T., Caulfield J., Brandt C., Bussweiler Y., Mollo S., Di Stefano F., Nazzari M., Scarlato P.*
Deep Magma Storage revealed by Multi-Method Elemental Mapping of Clinopyroxene Megacrysts at Stromboli Volcano
Frontiers in Earth Science, 7, 239
45. *Ubide T., Mollo S., Zhao J.X., Nazzari M., Scarlato P.*
Sector-zoned clinopyroxene as a recorder of magma history, eruption triggers, and ascent rates
Geochimica et Cosmochimica Acta 251, 265-283
46. *Violay M., Passelegue F., Spagnuolo E., Di Toro G., Cornelio C.*
Effect of water and rock composition on re-strengthening of cohesive faults during the deceleration phase of seismic slip pulses
Earth and Planetary Science Letters 522, 55-64
47. *Winkler A., Caricchi C., Guidotti M., Owczarek M., Macrì P., Nazzari M., Amoroso A., Di Giosa A., Lustrani S.*
Combined magnetic, chemical and morphoscopic analyses on lichens from a complex anthropic context in Rome, Italy.
Science of The Total Environment, 690; <https://doi.org/10.1016/j.scitotenv.2019.06.526>

In press

48. *Scarlato P., Mollo S., Petrone C.M., Ubide T., Di Stefano F.*
Interpreting magma dynamics through a statistically refined thermometer: Implications for clinopyroxene Fe-Mg diffusion modeling and sector zoning at Stromboli
AGU books - Crustal Magmatic System Evolution: Anatomy, Architecture, and Physico-Chemical Processes.
49. *Stagno, V., Aulbach, S.*
Redox processes before, during and after Earth's accretion affecting the deep carbon cycle.
AGU monographs.
50. *Stagno V., Kono Y., Stoppioni V., Masotta M., Scarlato P., Manning C.E.*
The viscosity of carbonate-silicate transitional melts at Earth's upper mantle P-T conditions by in-situ falling-sphere technique.
In Manning, C.E., Lin, J-F., Mao, W. (Eds) Carbon in Earth's Interior, AGU monographs.

Patents

51. *Bruno M., Caramelli A., Romeo G., Savio G.*
Rimessa per velivoli multi-rotore a controllo remoto
brevetto per invenzione industriale N. 102017000076573



Design by
Laboratorio Grafica e Immagini INGV

Rome, March 2020

Editing by Valeria Misiti

Disclaimer clause

This report contains data and information property of Istituto Nazionale di Geofisica e Vulcanologia in Rome (Italy). The information contained in this report don't imply the responsibility of the Istituto Nazionale di Geofisica e Vulcanologia. Our purpose is to supply reliable scientific information to the members of the national and international scientific community and to whoever could be interested in them. Istituto Nazionale di Geofisica e Vulcanologia does not engage any responsibility for the content. This material is constituted by information of general character, result of specific researches, or data coming from the laboratory activity. Copy and the dissemination of this report are authorized only under licence of HP-HT Laboratory people.